NTNU

Norwegian University of
Science and Technology

Development of a Patch Antenna Array between 2-6 GHz with Phase Steering Network for a Double CubeSat

Anton Johan Bolstad

Master of Science in Electronics
Submission date: June 2009
Supervisor: Odd Gutteberg, IET
Co-supervisor: Irene Jensen, SINTEF

Norwegian University of Science and Technology
Department of Electronics and Telecommunications

Problem Description

A phased array or a switched beam antenna solution for the double CubeSat project will be investigated. The placement of the antenna elements on the available area will be explored to optimize the antenna characteristics. Discuss different antenna solutions, and select one antenna solution with a corresponding feeding network. The frequency of operation can be either 2.5 or 5.8 GHz. The project should include a detailed design of the antenna solution and chosen parts of the antenna design. The final design will be manufactured using a commercial manufacturing house. The project also includes measurements of the antenna design. For the double CubeSat project it is important to focus on compact and light weight solutions, and for active designs it is important to choose solutions with low power consumption.

Assignment given: 15. January 2009
Supervisor: Odd Gutteberg, IET

Abstract

To make a double CubeSat with limited power resources capable of transmitting large amounts of data down to Earth, a high gain antenna is needed. In this thesis a switched beam MSA array operating at 5.84 GHz has been designed to operate on a double CubeSat. The array has 5 beams and uses a switched-line phase shifter to switch between beams. Three different array geometries has been proposed based on work done in [1]. Computer simulations suggest that the array should be capable of an effective beamwidth of over 60° with a directivity of over 11 dBi. A feed network has been designed to fit the best suited geometry. The antenna elements will be separated from the feed network with a ground plane. Along with the full array solution all the sub parts has been realized as test circuits. This allows for an evaluation of their characteristics. A TRL calibration kit has also been designed so that the sub parts could be more accurately evaluated. When sending the circuits to fabrication it appeared to be a problem with the selected substrate used for the antenna elements. A redesign using the same substrate for the feed network and antennas was done and production commenced. As it turns out, the TRL calibration kit was not good enough so the S-parameters had to be measured with regular SOLT calibration. Significant problems with connection to ground and mismatches due to a poor SMA-to-microstrip transition was encountered. This caused large deviations between measured and simulated results. It was also discovered that the wrong dielectric constant, ε_r, had been used. This error caused the antenna elements to be dimensioned for operation at 5.70 GHz instead of 5.84 GHz. Problems was also encountered in the switched line phase shifter design (based on a design from [2]). Beam-lead PIN-diodes have been used and due to their small size, a sufficient quality of the soldering was not achieved. This lead to different losses through the phase shifter which again caused the different beam directions to vary from simulations. Only one beam had characteristics similar to simulations. Measurements on the array without phase shifters showed good correspondence with simulation results (adjusted for the correct ε_r). It is concluded that by making a better SMA-to-microstrip transition, improve the soldering work and do a redesign with the correct dielectric constant, the array configuration should work as outlined in the design process.

Preface

Due to my involvement in the NTNU student satellite project, me and a fellow student got to travel to ESTEC in the Netherlands. We attended the 2nd European CubeSat Workshop where we presented some work from the project here at NTNU and listened to presentation from other university projects as well as presentations from ESA and other organizations. It was very interesting to hear about other projects and their way of solving different problems. CubeSats are being designed all over Europe with a large variety of experiments and solutions. There seems to be no limit to what you can do with these small satellites. I really must say that to hear about all the other projects going on around in Europe, provided me with a lot of inspiration.

Time has passed fast this last semester and I have enjoyed it a lot. The work has been interesting to do, but there have also been periods frustration when nothing seems to work. I guess so has the rest of my time as student been too. During my work with this thesis I have come to realize that I have actually learned something from my years at NTNU. It feels great to be able to use knowledge accumulated these last four and a half years and create something with them. I have also learned that experience is invaluable and cannot be taught, learning by doing is the only way to achieve it. Since I am very very far from being all-knowing and experienced in the field of satellites and antennas, I have received help and guidance from two that are a lot more seasoned in these fields. Therefore, I would like to thank my professor Odd Gutteberg (NTNU) and my supervisor Irene Jensen (SINTEF) for valuable input and support throughout the process of writing this thesis.

Trondheim June 17th

Anton Johan Bolstad

Contents

List of Figures

List of Tables

Nomenclature

ADCS Attitude Determination and Control Subsystem

ADS Advanced Design System

AF Array Factor

AMSAT-UK The Radio Amateur Satellite Corporation - United Kingdom

BER Bit Error Rate

BPSK Binary Phase Shift Keying

DQPSK Differential Quadrature Phase Shift Keying

DUT Device Under Test

EIRP Equivalent Isotropic Radiated Power

EM Electromagnetic

EMDS ElectroMagnetic Design System

ESA European Space Agency

ESTEC European Space Research and Technology Centre

FEM Finite Element Method

GEO Geostationary Orbit

HPBW Half Power Beamwidth

IL Insertion Loss

LEO Low Earth Orbit

MSA MicroStrip Patch Antenna

NTNU Norwegian University of Science and Technology

PCAAD Personal Computer Aided Antenna Design

PCB Printed Circuit Board

RF	Radio Frequency
SMA	SubMiniature version A
SMD	Surface Mounted Device
SNR	Signal-to-Noise Ratio
SOLT	Short-Open-Load-Thru
TEM	Transverse Electro Magnetic
TM	Transverse Magnetic
TRL	Thru-Reflection-Line
VNA	Vector Network Analyzer

Chapter 1

Introduction

The CubeSat standard (see App. A and [11]) was developed by CalPoly and Stanford University in 1999. Their goal was to offer a small and cheap platform that would bring space science and space exploration to universities around the world. The original CubeSat specification calls for a pico satellite with one liter volume, one kg mass and for the units to be released from a special deployment pod once the launch vehicle has reached its final orbit. The launch pod ensures that the CubeSat will not interfere with the launch vehicles main cargo, so that CubeSats can "hitchhike" on launch vehicles that has leftover capacity after the main payload has been fitted. Getting a free ride into space can be translated into several thousands of dollars in saved costs. It would probably be next to impossible to do this without a standardized and approved launch pod. Since the launch pod has a capacity of three units, the CubeSat standard now allows for satellites that has two and three times the volume of the standard unit of one liter volume. The 2x and 3x units are extended in height.

A major obstacle in satellite communications is the great distances and the following large free space path loss. For a satellite in LEO this problem is not as big as for a satellite in GEO, but the distance from the satellite down to Earth is still far greater than any earthbound line of sight radio link. Power available is also limited in space, so one would have to rely on good antennas and low noise receivers to make a usable satellite-to-Earth link.

In the specification document for the NTNU student satellite [12] that outlines a double CubeSat design it is suggested to use 437 MHz as the carrier frequency for the data down link. The radio system has been designed in [13] and features a 18 kBaud link with $\pi/4$-DQPSK modulation. This results in a 36 kbit/s link and a total of 2 MB transmitted data in one optimal pass (i.e the satellite passes directly over the ground station). Since this is a band used by radio amateurs and many other CubeSat projects there are

quite a few ground stations that can download data.

Depending on what task the satellite will perform in space, the amount of collected data will vary. If it gathers a lot of data a high speed data link is required. If it gathers rather small amounts of data it can still be transferred over a high speed link, but not vice versa. Therefore, a higher data throughput is highly desired. In order to increase the data rate from the satellite one would have to either increase the gain of the antennas at both ends and/or the EIRP from the satellite. Since the frequency is relatively low (long wavelength), a high gain antenna would become rather large. Power is a scarce resource in a small satellite, so increasing the output power is not an option. The solution will then be to increase the carrier frequency and bandwidth of the link. A down link between 2-6 GHz makes it possible to realize a relatively high gain reasonably sized antenna on the satellite as well as the use of a parabolic reflector antenna on the ground. The atmospheric loss is also at its minimum in this frequency band. In the frequency band 2-6 GHz there are two slots available for amateur satellites that can be used for satellite-to-Earth links these bands are 2400-2450 MHz (S-band) and 5830-5850 MHz (C-band) [14, 15].

For these frequency bands and operating environment microstrip patch antennas will be a good choice. To increase the directivity an array should be designed. In [1] it was found that an 2x2 array operating at the upper frequency band around 5.84 GHz could be fitted on the nadir side of the satellite and provide a directivity of 13.4 dBi. The lowest frequency band around 2.425 GHz will result in too large patches to realize an array on only the nadir panel.

According to a presentation at the 2nd European CubeSat Workshop by Graham Shirville from AMSAT-UK, the European Student Earth Orbiter will be the first amateur satellite to feature a C-band beacon. So it would be interesting to see if a satellite from NTNU could be the first amateur satellite with not only a beacon, but with a high speed C-band data link.

1.1 Software

To be able to solve the different problems in this thesis different software solutions have been used. These include:

- Agilent EMDS 2006C
- Agilent ADS 2008 Update 2
- Antenna Design Associates PCAAD 5.0
- Elprint Macaos Enterprise 2.11

- Cascade Microtech WinCal 3.2.2.6
- The Mathworks MATLAB R2008a

1.2 Outline

This thesis will first present some basic theory regarding antennas, space operations and link budgets. Theory concerning radiation mechanism and MSAs are heavily based on explanation from [3], while array theory mainly stems from [6]. The following chapter presents the design procedure for a single antenna element followed by a chapter where an array geometry is chosen. Next the feed network will be designed and fitted with a phase shifter. Then the simulations circuits are made into layouts for fabrications. Circuits are then measured and the results presented. The thesis is then ended by a discussion, conclusion and suggestions for further work.

Chapter 2

Microstrip Antenna and Array Basics

2.1 Coordinate System

When describing radiation patterns and antenna characteristics a spherical coordinate system like in Fig. 2.1 is often used. In this thesis the radiating antenna will be in the xy-plane/azimuth plane and the z-direction ($\theta = 0°$) is the boresight direction.

2.2 Radiation Mechanism

EM radiation occurs when there is an accelerated charge or a time-varying current. Imagine a very thin wire with a charge density, q_l, along its length, l. The charge is moving along the wire in the z-direction with a velocity v_z, caused by an electric field, E, . The total current, I_z can then be written as

$$I_z = q_l v_z \tag{2.1}$$

In the case where the current, I_z, is time varying its derivative can be written as

$$\frac{dI_z}{dt} = q_l \frac{dv_z}{dt} = q_l a_z \tag{2.2}$$

where a_z is the acceleration. Time varying currents are found in time-harmonic applications while accelerated/decelerated charge occurs in curved,

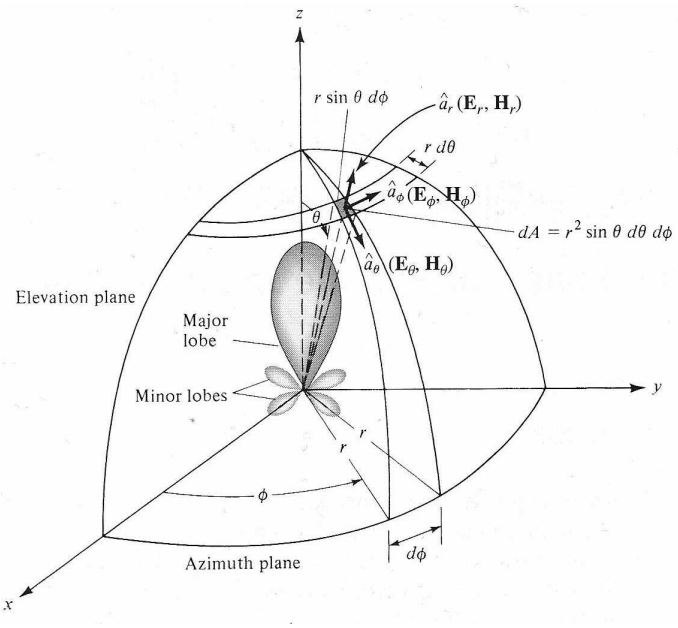

Figure 2.1: Coordinate system used when describing the antenna characteristics. Source [3].

bent, discontinuous or terminated wires.
Summed up:

- Without a moving charge there is no current and no radiation.
- There will be no radiation from a moving charge that travels along an infinitely long wire with a constant velocity.
- There will be radiation from a charge moving along a curved, bent, discontinuous or terminated wires even though it travels at a constant velocity.
- If there is a time-varying current, there will also be radiation.

By applying a time-varying sinusoidal voltage between two conducting wires an electric field will appear between them like in Fig. 2.2. The free-space waves/field are periodic just like the ones between the conductors. As the field propagates into free space, one can say that the field "detaches" itself from the conductors when the voltage between them becomes zero. If the wires in Fig. 2.2 is bent further out to $\pm 90°$, a dipole antenna can be realized like in Fig. 2.3.

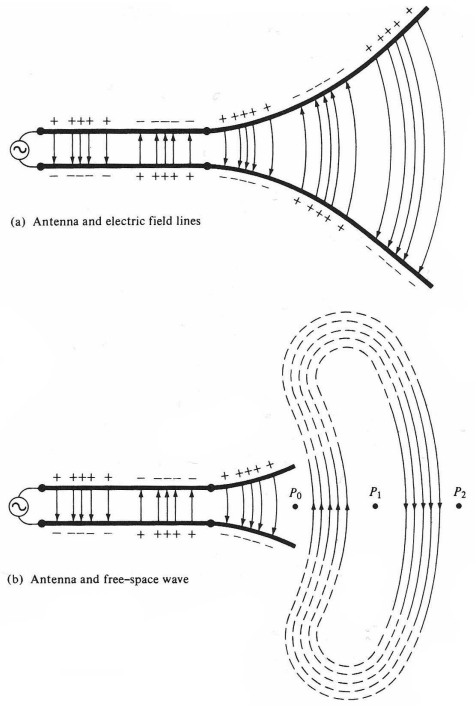

Figure 2.2: Propagating E-field between two conductors and its detachment. Source [3].

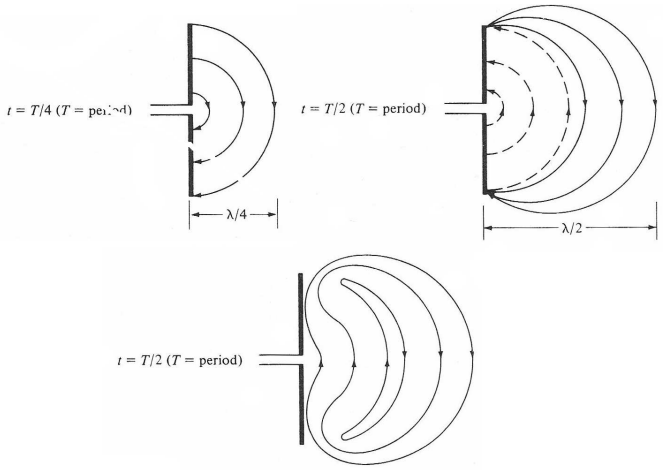

Figure 2.3: Radiating and detaching E-field from a dipole. Source [3].

2.3 Microstrip Patch Antenna

A MSA consist of a ground plane, a substrate and a metal patch like in Fig. 2.4. This structure makes the MSA suitable for applications that demands a thin, robust and lightweight antenna. A MSA can for instance be made conformal with the outer surface of an aircraft or a missile. It is the relatively small form factor and lightweight features that makes this type of antenna attractive for the purpose of a high gain small satellite antenna. MSAs are also cheap and easy to fabricate using printed-circuit techniques

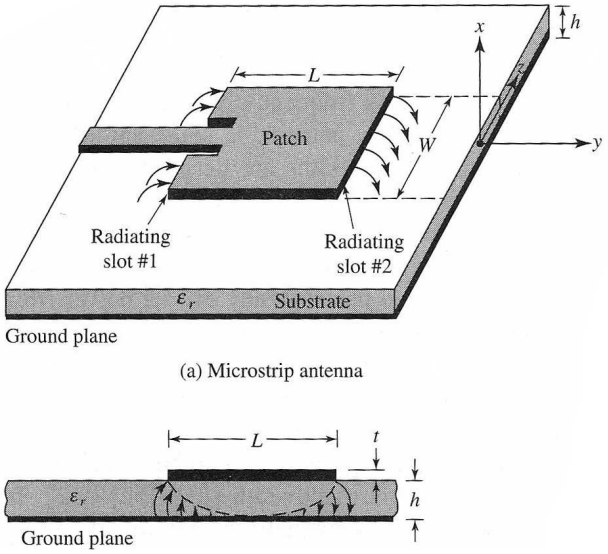

Figure 2.4: General geometry of a microstrip line fed MSA. Source [3].

2.3.1 Microstrip

A *microstrip* is a planar structure consisting of a ground plane covered with a sheet of low loss dielectric and a metal conductor strip on top. An electromagnetic wave will propagate between the metal strip and the ground plane when a signal is applied. Since the microstrip-line structure has a discontinuity in permittivity (two different dielectrics, substrate and air) it does not support *TEM waves*, but instead *quasi-TEM* waves (TEM-waves with a small longitudinal component). As one can see from Fig. 2.5, not all of the electrical field will be contained inside the substrate between the strip and the ground plane (the higher dielectric permittivity the more of the file will be contained in the substrate). These fields are called *fringing fields*. They cause radiation and therefore losses along the line.

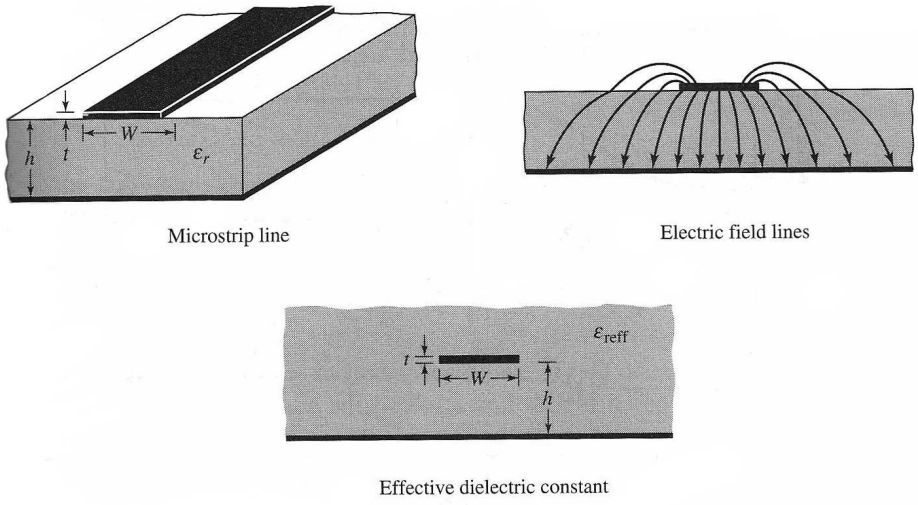

Figure 2.5: General Microstrip geometry. Source [3].

To account for the fringing fields along the edges and the discontinuity in dielectric permittivity, an *effective dielectric constant*, ε_{reff} is introduced like in the bottom microstrip configuration in Fig. 2.5. This equivalent line has the same electrical properties as the real microstrip line. The effective dielectric constant ε_{reff} is in the range $1 < \varepsilon_{reff} < \varepsilon_r$, where 1 is the free space permittivity. The effective dielectric constant can be calculated using (2.3) from [16]. This equation only gives static values and does not account for dispersion, it will therefore only be accurate for lower frequencies.

$$\varepsilon_{reff} = \frac{\varepsilon_r + 1}{2} + \frac{\varepsilon_r - 1}{2}\left[1 + 12\frac{h}{W}\right]^{-1/2}, \text{ where } \frac{W}{h} > 1 \qquad (2.3)$$

2.3.2 Microstrip Resonator

Transmission-line Model

By using the *transmission-line model* outlined in [3], a rectangular microstrip resonator can be modeled by its length L, width H, height h and two narrow radiating slots along the width. This model is a simple resonator model, but it gives a physical insight and not too complicated equations that are suited for quick design calculations. Due to the fringing fields the patch will become electrically larger than its physical dimensions. A rectangular microstrip resonator is around half a wavelength long, so that the phase of the field along the length of the patch will vary with 180°, see Fig. 2.7 and Fig. 2.6.

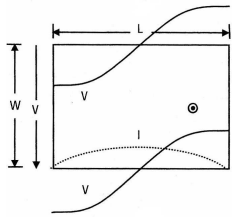

Figure 2.6: Current and voltage distribution along a resonant patch. Source [4].

If one observes the fringing fields from above the patch like in Fig. 2.8, it can be observed that the fringing fields along the length of the patch will cancel each other out. Fringing fields along the width of the patch will on the other hand add in phase and radiate. To account for the electrically larger length of the patch, the length will be increased by ΔL at both ends. The expression for ΔL can be found in [17] and is given in (2.4)

$$\frac{\Delta L}{h} = 0.412 \frac{(\varepsilon_{reff} + 0.3)\left(\frac{W}{h} + 0.264\right)}{(\varepsilon_{reff} - 0.258)\left(\frac{W}{h} + 0.8\right)} \tag{2.4}$$

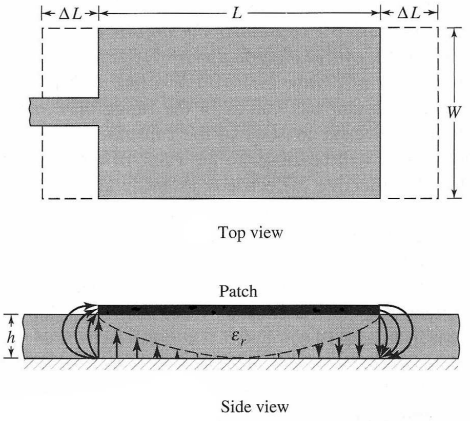

Figure 2.7: Rectangular microstrip resonator. Source [3].

This results in an effective patch length of

$$L_{eff} = L + \Delta L \tag{2.5}$$

According to [3], the dominant mode of a resonant patch is TM^x_{010}. and the resonance frequency is given by

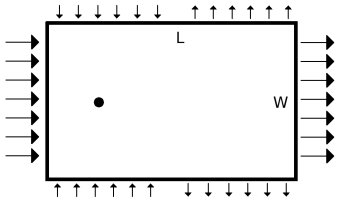

Figure 2.8: Fringing fields around a microstrip resonator.

$$(f_0)_{010} = \frac{1}{2L\sqrt{\varepsilon_r}\sqrt{\mu_0\varepsilon_0}} = \frac{v_0}{2L\sqrt{\varepsilon_r}} \tag{2.6}$$

where v_0 is the speed of light in free space. The above formula does not account for the fringing fields (uses L and ε_r), but with some modifications it can

$$(f_r)_{010} = \frac{1}{2L_{eff}\sqrt{\varepsilon_{reff}}\sqrt{\mu_0\varepsilon_0}} \tag{2.7}$$

Cavity model

A more accurate model than the transmission-line model described above is the *cavity model*. However, the increased accuracy comes at the cost of increased complexity. The cavity model approximates the MSA as a resonant cavity filled with a lossless dielectric medium. The cavity is bound with perfect electric conductors at the top and bottom and with perfect magnetic conducting side walls. As the patch gets energized a charge is distributed on the the patch and the ground plane like in Fig. 2.9.

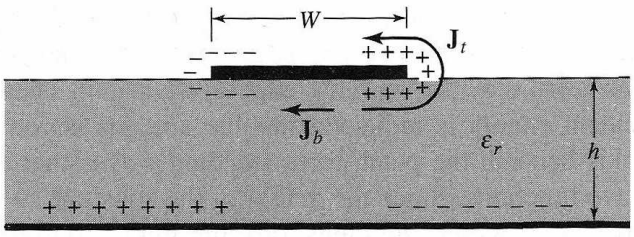

Figure 2.9: Charge distribution and current density on a MSA structure. Source [3].

This build-up is affected by an attractive force between opposite charges on the bottom side of the patch and the ground plane and a repulsive force

between equal charges. The charge distributions on the sides and top of the patch are caused by the repulsive mechanism, while the charge concentration at the bottom are caused by the attractive force. The currents $\mathbf{J}_b$ and $\mathbf{J}_t$ are caused by movement of the above mentioned charges. For most MSA the height-to-width ratio is very small and this causes the attractive force to dominate over the repulsive force. The current around the edges of the patch will therefore decrease as the height-to-width ratio decreases. When the height-to-width ratio approach zero the current flowing around the edges will also approaches zero. With no current flow around the edges the tangential magnetic field to the edges of the patch will be zero. No real MSA will have a height to width ratio of zero, so modeling the side walls of the cavity/patch as perfect magnetic conductors is an approximation. So far this model is a lossless cavity resonator that does not account for radiation, so a loss mechanism should be introduced. A loss tangent is introduced that accounts for radiation and conduction-electric losses. Since the height of the MSA usually is very small compared to a wavelength, the field in the x-direction can be considered as constant. Because of the small height the fringing fields will also be small and almost normal to the surface of the patch. The consequence of this is that only TM^x field configurations will be considered inside the cavity. The field configurations or modes inside the cavity can be found by applying the vector potential approach. The vector potential must satisfy the homogeneous wave equation. The problem is solved in, e.g., [3] with the resonant frequencies derived as

$$(f_r)_{mnp} = \frac{1}{2\pi\sqrt{\mu\varepsilon}}\sqrt{\left(\frac{m\pi}{h}\right)^2 + \left(\frac{n\pi}{L}\right)^2 + \left(\frac{p\pi}{W}\right)^2} \tag{2.8}$$

If L > H > h the dominant mode (mode with the lowest resonance frequency) inside the cavity will be the TM^x_{010} mode. As one can see from Fig. 2.10 the E-field is constant along the width of the patch and varies with a half period along the length.

$$(f_r)_{010} = \frac{1}{2L\sqrt{\mu\varepsilon}} \tag{2.9}$$

The above equation above does not account for fringing fields. One must use 2.7 to account for these fields (more accurate)

More details on the cavity model can be found in books like [3, 18]

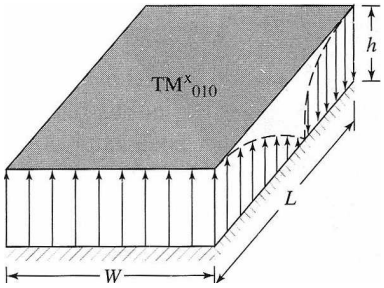

Figure 2.10: Field configurations for the TM^x_{010} mode. Source [3].

2.3.3 MSA Design Procedure

The transmission-line model can be used to make a quick preliminary MSA design if one knows the substrate parameters, ε_r and h, and which center frequency, f_0, that is desired, [3]. A formula for an efficient patch width is

$$W = \frac{1}{2f_0\sqrt{\mu_0\varepsilon_0}}\sqrt{\frac{2}{\varepsilon_r+1}} = \frac{v_0}{2f_0}\sqrt{\frac{2}{\varepsilon_r+1}} \tag{2.10}$$

To calculate the length of the patch, it is needed to first calculate ε_{reff} by using (2.3) and ΔL by using (2.4). These values must then be inserted into (2.11)

$$L = \frac{1}{2f_0\sqrt{\varepsilon_{reff}}\sqrt{\mu_0\varepsilon_0}} - 2\Delta L \tag{2.11}$$

The BW for a MSA is usually given as the frequency band where the VSWR ≤ 2. A theoretical expression for the BW in both GHz, (2.12), and percent, (2.13), is given in [4].

$$BW \cong 50hf^2 \tag{2.12}$$

where f is given in GHz and h in cm.

$$\%BW = \frac{Ah}{\lambda_0\sqrt{\varepsilon_r}}\sqrt{\frac{W}{L}} \tag{2.13}$$

where

$$A = 180 \text{ for } \frac{h}{\lambda_0\sqrt{\varepsilon_r}} \leq 0.045$$
$$A = 200 \text{ for } 0.045 \leq \frac{h}{\lambda_0\sqrt{\varepsilon_r}} \leq 0.075$$
$$A = 220 \text{ for } \frac{h}{\lambda_0\sqrt{\varepsilon_r}} \geq 0.075$$

An approximate formula for the directivity of a rectangular MSA is also given in [4]

$$D \cong 0.2W + 6.6 + 10\log\left(\frac{1.6}{\sqrt{\varepsilon_r}}\right) \text{ dB} \tag{2.14}$$

2.3.4 Radiation Diagram

The radiation diagram from a rectangular MSA can be calculated by applying aperture theory and Fourier Transform [3]. Assume that the radiation comes from two rectangular apertures with the dimension $W \times h$ positioned along the width W of the patch as depicted in Fig. 2.11. Within the aperture the field is constant with an amplitude E_0. Further assume that the dimension $h \ll W, L$ so that the radiation can be calculated as it came from a magnetic current at each side of the patch with a distance $L_e = L + h$ between them. According to [5] the far field can then be calculated as following

$$E_{xa}\left(x', y', z' = 0\right) = \begin{cases} E_0 & \text{for} \quad L/2 \leq |x'| \leq L/2 + h \text{ and } |y'| \leq W/2 \\ 0 & \text{otherwise} \end{cases} \tag{2.15}$$

Since h is so small compared to the length, the pulse functions along x' can be replaced with δ-functions placed at $\pm L_e/2$. (2.15) can then be rewritten into

$$E_{xa}\left(x', y', z' = 0\right) = \begin{cases} E_0 h\left[\delta\left(x' + L_e/2\right) + \delta\left(x' - L_e/2\right)\right] & \text{for } |y'| \leq W/2 \\ 0 \quad \text{otherwise} \end{cases} \tag{2.16}$$

To calculate the far-field the Fourier Transform that can be found in [3] must be used.

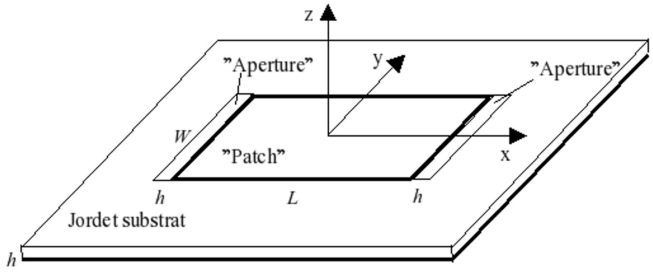

Figure 2.11: Geometry for radiation calculations. Source [5].

$$f_x(k_x, k_y) = \int\int E_{xa}(x', y', z' = 0)\, e^{j(k_x x' + k_y y')} dx' dy' \tag{2.17}$$

$$f_y(k_x, k_y) = \int\int E_{ya}(x', y', z' = 0)\, e^{j(k_x x' + k_y y')} dx' dy' \tag{2.18}$$

where

$$\begin{aligned} k_x &= k \sin\theta \cos\phi \\ k_y &= k \sin\theta \sin\phi \end{aligned} \tag{2.19}$$

and the far-field is given as

$$\begin{aligned} E_\theta &= f_x \cos\phi + f_y \sin\phi \\ E_\phi &= \cos\theta\,(-f_x \sin\phi + f_y \cos\phi) \\ \mathbf{E}(r, \theta, \phi) &= j\frac{ke^{-jkr}}{2\pi r}\left(\hat{\mathbf{a}}_\theta E_\theta + \hat{\mathbf{a}}_\phi E_\phi\right) \end{aligned} \tag{2.20}$$

Since the integrand in (2.17) can be separated in x' and y', the integral below can also be separated. Multiply with $E_0 h$ to obtain the right value of the integral along the x-axis.

$$
\begin{aligned}
f_x =& E_0 h \int_{\infty}^{\infty} \left[\delta\left(x' + L_e/2\right) + \delta\left(x' - L_e/2\right)\right] e^{jk_x x'} dx' \\
& \int_{-W/2}^{W/2} e^{jk_y y'} dy' \\
=& E_0 h \left[e^{-jk_x L_e/2} + e^{-jk_x L_e/2}\right] \frac{1}{jk_y} \left[e^{-jk_y y'}\right]_{-W/2}^{W/2} \\
=& E_0 h 2 \cos\left(k_x L_e/2\right) \frac{2j \sin\left(k_y W/2\right)}{jk_y} \frac{W/2}{W/2} \\
=& 2hW E_0 \cos\left(k_x L_e/2\right) \frac{\sin\left(k_y W/2\right)}{k_y W/2}
\end{aligned}
\tag{2.21}
$$

Since there are no field components in the y-direction, $f_y = 0$. The far-field then becomes

$$
\mathbf{E}\left(r, \theta, \phi\right) = j \frac{k e^{-jkr}}{2\pi r} \left[\hat{\mathbf{a}}_\theta f_x \cos\phi - \hat{\mathbf{a}}_\phi \cos\left(\theta\right) f_x \sin\phi\right] \tag{2.22}
$$

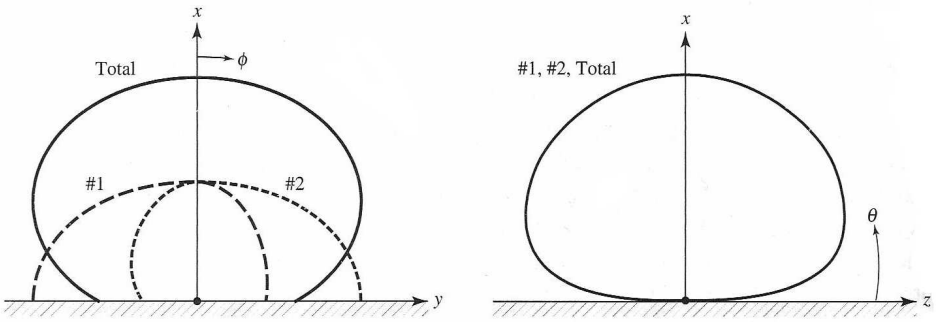

Figure 2.12: E- and H-plane radiation diagram for a typical MSA. Source [3].

2.4 Antenna Array

An antenna array is a matrix like structure consisting of two or more antennas. The fields from the antennas is added and the phase of the fields determines whether there is constructive or destructive interference. The phases of the fields can be controlled by either exiting the elements with signals of different phases or by taking advantage of the physical placement of the array elements.

An antenna array can be understood using only geometrical considerations, but this is a simplification. A thorough treatment would have to use electromagnetic modeling to consider how the elements interact with each other through mutual coupling. However, a geometrical consideration would be the first step in designing an array anyway.

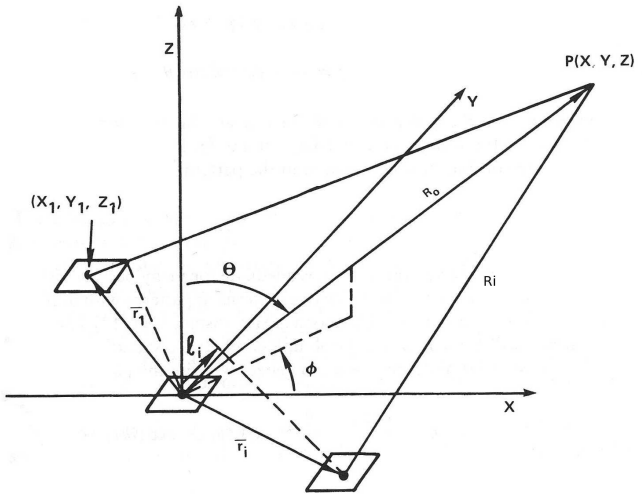

Figure 2.13: Generalized array configuration. Source [6].

Consider the elements in Fig. 2.13. They radiate in a directional pattern dependent on both the angle and radial distance close to the element. At a large distance this dependence will be $e^{(-jkR)}/R$ multiplied with an angle dependent vector function, $\mathbf{f_i}(\theta, \phi)$, that is element dependent and referred to as the *element factor*. One can then write the far field for element number i as

$$\mathbf{E_i}(r, \theta, \phi) = \mathbf{f_i}(\theta, \phi) \frac{e^{(-jkR_i)}}{R_i} \tag{2.23}$$

where

$$R_i = \left[(x - x_i)^2 + (y - y_i)^2 + (z - z_i)^2\right]^{1/2} \tag{2.24}$$

At a point far away from the array the difference between radius vector from element i and from the center of the array becomes negligible. However, this approximation is only valid for the amplitude of the field. The phase must include information about how the element is positioned relative to the defined center. It will determine whether there will be destructive or constructive interference.

$$R_i \approx R_0 - \hat{\mathbf{r}} \cdot \mathbf{r_i} \tag{2.25}$$

$$\frac{e^{(-jkR_i)}}{R_i} \approx \frac{e^{(-jkR)}}{R} e^{(+jk\hat{\mathbf{r}}\cdot\mathbf{r_i})} \tag{2.26}$$

The above expression can be expressed in terms of θ and ϕ using the relations below

$$\begin{aligned} \mathbf{r_i} &= \hat{\mathbf{x}}x_i + \hat{\mathbf{y}}y_i + \hat{\mathbf{z}}z_i \\ \hat{\mathbf{r}} &= \hat{\mathbf{x}}u + \hat{\mathbf{y}}v + \hat{\mathbf{z}}\cos\theta \\ u &= \sin\theta\cos\phi \\ v &= \sin\theta\sin\phi \end{aligned} \tag{2.27}$$

Inserting the relations from (2.26) and (2.27) into (2.23) results in the far-field for element i

$$\mathbf{E_i}(\mathbf{r}) = \frac{e^{(-jkR)}}{R} a_i \mathbf{f_i}(\theta,\phi)\, e^{(jk\hat{\mathbf{r}}\cdot\mathbf{r_i})} \tag{2.28}$$

where a_i is the amplitude that of which element i is exited with. The expression below can be used to describe an arbitrary array

$$\mathbf{E}(\mathbf{r}) = \frac{e^{(-jkR)}}{R} \sum_i a_i \mathbf{f_i}(\theta,\phi)\, e^{(jk\hat{\mathbf{r}}\cdot\mathbf{r_i})} \tag{2.29}$$

Usually the elements in an array are identical, so that the element factor can be placed outside the summation sign like this

$$\mathbf{E}(\mathbf{r}) = \mathbf{f}(\theta,\phi) \frac{e^{(-jkR)}}{R} \sum_i a_i e^{(jk\hat{\mathbf{r}}\cdot\mathbf{r_i})} \tag{2.30}$$

From the above equation one can derive the *array factor*, AF .

$$AF = \sum_i a_i e^{(jk\hat{\mathbf{r}}\cdot\mathbf{r_i})} \tag{2.31}$$

2.4.1 One Dimensional Array

Instead of using the real valued weighting function, a_i, a complex value can be assigned. This means that not only the amplitude of the signal may vary between elements, but also the phase

$$a_i = |a_i| \, e^{(-jk\mathbf{r_i}\cdot\hat{\mathbf{r}}_\mathbf{0})} \tag{2.32}$$

where

$$\hat{\mathbf{r}}_\mathbf{0} = \hat{\mathbf{x}}u_0 + \hat{\mathbf{y}}v_0 + \hat{\mathbf{z}}\cos\theta_0 \tag{2.33}$$

and

$$k = \frac{2\pi}{\lambda} \tag{2.34}$$

The weighing functions will steer the beam in a direction (θ_0, ϕ_0). This is possible because in that direction the exponential function in (2.32) will cancel out the exponential function in (2.31). The pointing direction is frequency independent. The easiest way to achieve different phase excitation of the elements is to add a transmission line length that has a electrical length equal to the phase delay that is needed. Another way to do it is by the help from phase shifters. To adapt (2.32) to the use of phase shifters one would have to use the free space wave number, k_0, instead of the substrate wave number, k. This will introduce some frequency dependence.

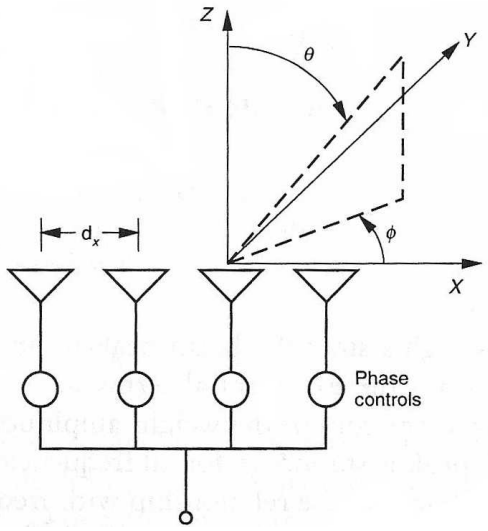

Figure 2.14: Two dimensional scanning array in the zx-plane. Source [6].

The array depicted in Fig. 2.14 has elements that are spaced d_x apart. The radiated field then becomes

$$\mathbf{E}(\theta) = \mathbf{f}(\theta, \phi) \sum a_n e^{[jk_0(nd_x u)]} \tag{2.35}$$

a_n is the complex weight to element n. For a fixed frequency a maximum in direction $(\theta_0, 0)$ can be realized by choosing the weight, a_n, like this

$$a_n = |a_n| e^{-jk_0 n d_x u_0} \tag{2.36}$$

then the array factor becomes

$$AF(\theta) = \sum |a_n| e^{jnd_x k_0 (u - u_0)} \tag{2.37}$$

2.4.2 Two Dimensional Planar Array

A two dimensional array will have its elements in a plane instead of just along an axis, here the xy-plane will be used. Such an array can steer the beam in both θ- and ϕ-direction. For a geometry like in Fig. 2.15 the elements will be placed at distance

$$\mathbf{r}_{m,n} = \hat{\mathbf{x}} m d_x + \hat{\mathbf{y}} n d_y \tag{2.38}$$

So in order to steer the phase in a direction (θ_0, ϕ_0) at frequency f_0 the AF must be

$$AF(\theta, \phi) = \sum_{m,n} |a_{m,n}| e^{jk_0[md_x(u-u_0) + nd_y(v-v_0)]} \tag{2.39}$$

where u and v is defined in (2.27)

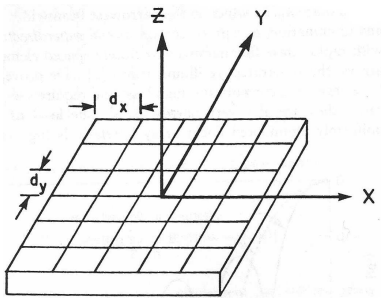

Figure 2.15: Geometry for a planar array. Source [6].

Chapter 3

RF Design Basics

RF signals operates at such high frequencies that the wavelengths becomes comparable with circuit and circuits component dimensions. Due to this RF signals should be treated as waves.

3.1 Reflection Coefficient

Consider a transmission line with a characteristic impedance of Z_0 terminated in a load Z_L. An incident voltage, V_0^+, is traveling towards load while a reflected voltage, V_0^- is traveling from the load. The ratio between voltage and current on a transmission line is the line impedance in which the corresponding voltage is the sum of the incident and reflected voltage. The current towards the load will be $(V_0^+ - V_0^-)$ divided by the line impedance At the load the ratio should then be decided by the load impedance Z_L like this;

$$Z_L = \frac{V}{I} = \frac{V_0^+ + V_0^-}{\frac{V_0^+ - V_0^-}{Z_0}}$$

which can be rearranged into

$$V_0^- = \frac{Z_L - Z_0}{Z_L + Z_0} V_0^+$$

the ratio between the reflected and incident voltage can then be found as the *reflection coefficient*, Γ.

$$\Gamma = \frac{V_0^-}{V_0^+} = \frac{Z_L - Z_0}{Z_L + Z_0} \tag{3.1}$$

3.2 VSWR

When a mismatched load causes a reflection on a transmission line, Γ is the ratio between the incident and reflected voltage. The mismatched load leads to standing waves on the transmission line. The maximum value of the standing wave will occur when the incident and reflected voltage is added in phase and will be equal to

$$V_{max} = \left|V_0^+\right| (1 + |\Gamma|)$$

while the minimum value will occur when the voltages are added out of phase

$$V_{min} = \left|V_0^+\right| (1 - |\Gamma|)$$

The ratio between maximum and minimum voltage along a line is referred to as the *voltage standing wave ratio* or VSWR and is defined as:

$$\text{VSWR} = \frac{V_{max}}{V_{min}} = \frac{1 + |\Gamma|}{1 - |\Gamma|} \tag{3.2}$$

A VSWR of 1 (minimum value) implies a perfectly matched load.

3.3 Quarter Wave Transformer

The quarter wave transformer can be deduced from the *transmission line impedance equation* [19] given below

$$Z_{in} = Z_0 \frac{Z_L + jZ_0 \tan \beta l}{Z_0 + jZ_L \tan \beta l} \tag{3.3}$$

where

$$\beta = \frac{2\pi}{\lambda}$$

and Z_{in} is the input impedance, Z_0 is the line impedance and Z_L is the load impedance.

If the line length, l, is equal to a quarter wavelength the argument inside the tangent expression will be equal to $\pi/2$. The tangent expression will then become infinity and (3.3) can be written as

$$Z_{in} = \frac{Z_0^2}{Z_L} \tag{3.4}$$

$$Z_0 = \sqrt{Z_{in} Z_L} \tag{3.5}$$

This means that by adding a piece of line that is a quarter wavelength long and has a characteristic impedance of, e.g. 70.7 Ω, transformation between 50 Ω and 100 Ω is possible.

3.4 S-parameters

The scattering matrix describes incident and reflected voltages at the ports on a device with N ports. The scattering matrix is useful when performing measurements at higher frequencies since it measures voltages that goes into the device and what is reflected or scattered through the N ports of the device or network. It is easier to measure these voltages than to measure total voltages and currents according to [19].

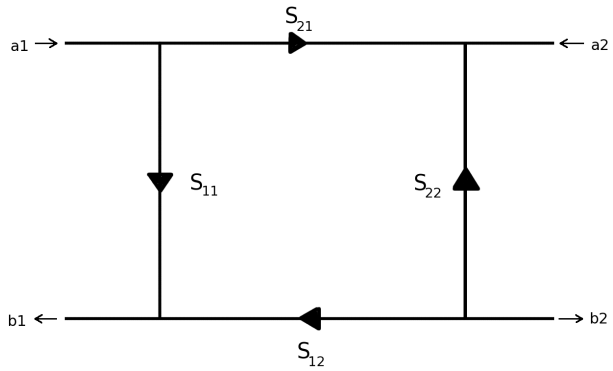

Figure 3.1: Generalized two-port S-parameter network. a1 and a2 represents incident voltages while b1 and b2 are reflected /transmitted voltages.

From Fig. 3.1 the four two-port S-parameters can be defined as:

- $S_{11} = \frac{b1}{a1}$, is the same as the reflection coefficient, Γ_1, for port 1. Input port reflection coefficient.

- $S_{21} = \frac{b2}{a1}$, tells how much of the incident voltage on port 1 is transmitted in the forward direction through the two-port network. For a passive network it describes loss while in an active circuit it can represent gain.
- $S_{12} = \frac{b1}{a2}$ tells how much of the incident voltage on port 2 is transmitted in the reverse direction. through the two-port network. For a passive network it describes loss while in an active circuit it can represent gain.
- $S_{22} = \frac{b2}{a2}$, is the same as the reflection coefficient, Γ_2, for port 2. Output port reflection coefficient

In general, S-parameter S_{ij} can be found by applying a voltage V_j^+ into port j and measure the reflected voltage V_i^- out of port i. Only port j can have have an incident voltage during this measurement, the other ports must therefore be terminated in matched loads to avoid reflections.

$$S_{ij} = \frac{V_i^-}{V_j^+}$$

3.4.1 Insertion Loss

The drawback of using S_{21} as the loss parameter is that it gives the ratio of power into port 1 divided by the power into port 2. In case of a DUT that is perfect or a near perfect match to the source or VNA, S_{21} will give a good representation of the loss through the device. However, if the DUT is poorly matched to the VNA a great portion of the incident power will be reflected before it enters the DUT. Using S_{21} as an indication of the loss through the DUT in this case will give a loss that is greater than the real loss through the device. A portion of the incident power will never enter the DUT. So in order to assess the actual loss through a DUT, without the mismatch losses, the *insertion loss*, IL, should be used:

$$IL = -10 \log \frac{|S_{21}|^2}{1 - |S_{11}|^2} \tag{3.6}$$

The insertion loss represents the ratio of power the actual enters the DUT and the power that flows into port 2.

Chapter 4

Satellite Communication Basics

4.1 Orbital Mechanics

Given the Earth as a point of mass, an orbiting satellite and no other forces involved *Kepler's laws of planetary motion* will determine the satellite's orbit. These are:

- The planets are moving in elliptical orbits with the Sun in one of the focal points
- Radius vector from the Sun to the planets covers an equal area in equal periods of time
- The square of the orbital period for the planets is proportional to the cube of the semi-major axis

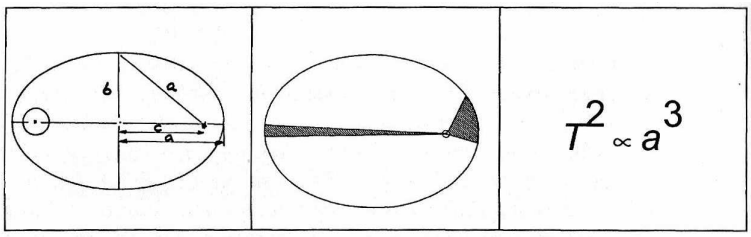

Figure 4.1: Illustration of Kepler's planetary motions laws. Source [7].

In combination with *Newton's law of universal gravitation* an expression for the orbital velocity can be derived [7].

$$v = \sqrt{\mu\left(\frac{2}{r} - \frac{1}{a}\right)} \tag{4.1}$$

where

$$\begin{aligned} &\mu = GM \\ &G \approx 6.674 \times 10^{-11} \quad \text{N(m/kg)}^2 \quad \text{(gravitational constant)} \\ &M = 5.9742 \times 10^{24} \quad \text{kg} \quad \text{(Earth mass)} \end{aligned}$$

In case of a circular orbit a will be equal to r and the orbital velocity can be calculated. Once the orbital velocity is known the orbital period can also be calculated. Consider a circular orbit with an orbital height, h, of 800 km and the Earths radius, R_J, of 6378 km:

$$\begin{aligned} v &= \sqrt{\mu\frac{1}{r}} = \sqrt{\mu\frac{1}{h + R_J}} = 7.45\text{km/s} \\ T &= \frac{2\pi r}{v} = 6054\text{s} \approx 100\text{min} \end{aligned}$$

4.2 Space Environment

Space is a harsh environment with vacuum, radiation and extreme variations in temperature. The background temperature of space in 2.7 K, but when an object is exposed to the Sun while in an Earth orbit, it is exposed to approximately 1.4 kW/m^2 of incident power that can heat up the satellite and cause large variations in temperature. Radiation can cause problems for semiconductor electronics. Charged particles can destroy the hole and electron distribution in the semiconductor material and render them useless. Solar panels degrades over time due to particle collisions. Because of the vacuum in space one must be careful when selecting materials for space applications. Materials exposed to vacuum may undergo outgassing of corrosive gasses such as chloride. The corrosive gas will then corrode metal in the satellite and damage electric wiring or the satellite platform itself.

4.3 ADCS

In order to stabilize a satellite or to change its attitude, some sort of control and measurement device is needed. When the satellite is released into orbit

it will most likely tumble, to stop the tumbling one needs to know how the satellite tumbles to counteract the tumbling. Measuring the movement can be done with, e.g., sun sensors, magnetic sensors or by measuring variation in received signal strength from the satellite. Output from the sensors will then be fed into a control algorithm that will perform corrective maneuvers through e.g. magnetic coils. Once the satellite is stable enough a gravity gradient boom could be deployed in either the nadir or zenith direction to maintain stability along the pitch and roll axes. A gravity boom is a passive solution opposed to a solution with e.g. active magnetic coils that consumes power when operated. In [8] it is suggested that a gravity gradient boom solution would give an accuracy of $\pm 5^\circ$ around the pitch- and roll-axis. Magnetic coils or a momentum wheel could be used for stabilization along the yaw-axis.

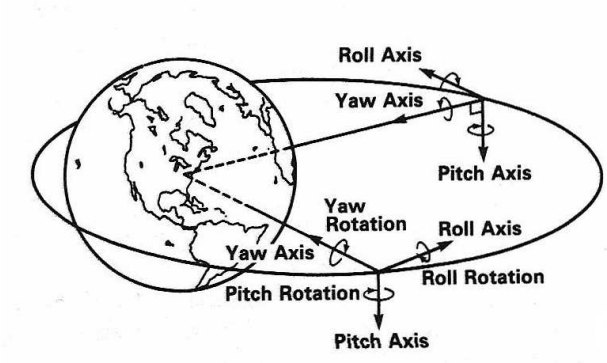

Figure 4.2: Illustration of how the axes are defined on a orbiting satellite. Source [8].

4.4 Satellite - Ground Station Geometry

When describing a satellites position relative to a ground station three parameters are needed

- *Elevation angle* - angle between a line from the ground station to the satellite and the ideal horizon (tangential plane). Tells how "high" the satellite is on the sky
- *Azimuth angle* - angle between the projection of the line between the ground station and the satellite into the tangential plane and true North. Tells in which direction the satellite is
- *Slant range* - distance between the ground station and the satellite

To calculate the slant range for a satellite at the same longitude as the ground station (at sea level) some information must be known. The Earth central angle which is between the line from the satellite to the Earths center and the line from the ground station to the Earths center (difference in latitude between the ground station and the satellites footprint), called jsv in Fig. 4.3 and the satellites orbital height. The slant range, D, can then be calculated by applying the *law of cosines*

$$D = \sqrt{R^2 + (R+h)^2 - 2R\,(R+h)\cos jsv} \tag{4.2}$$

Once D is known, the elevation angle can be found by applying the *law of sines*

$$e = \arcsin\left(\sin(jsv)\frac{R+h}{D}\right) - 90 \tag{4.3}$$

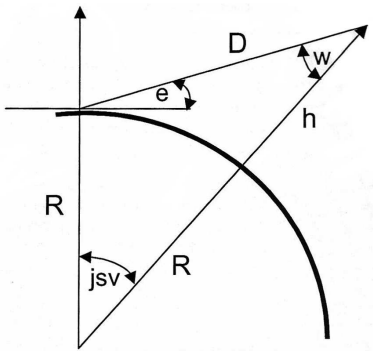

Figure 4.3: Slant range, D, and elevation, e.

This means that if a satellite in a 800 km high circular orbit is currently at the horizon directly south of ground station the

- elevation angle will be 0°
- azimuth angle will be 180°
- slant range will be 3293 km

4.5 Link Budget

The link budget describes the transmission link in terms of gain, losses and noise as an arithmetic sum of logarithmic values. It gives an overview over important parameters and how they interact with the overall link design.

Friis Transmission Equation

The quality of the received signal is determined by its *carrier to noise ratio*, C/N. The received power can be found by first calculating the *power flux density*, Φ. If a transmitter radiates P_T Watt from its antenna with gain G_T (relative to an isotropic radiator) then the power flux density at d meters will be

$$\Phi = \frac{P_T G_T}{4\pi d^2} \quad \left[\frac{\mathrm{W}}{\mathrm{m}^2}\right] \tag{4.4}$$

where $P_T G_T$ is the EIRP and the denominator describes the surface of a sphere with radius d. The power radiates out in spherical waves. The power received by a receiver is dependent on how large the *effective aperture*, A_E, of the receiving antenna is

$$P_R = \left(\frac{P_T G_T}{4\pi d^2}\right) A_E \quad [\mathrm{W}] \tag{4.5}$$

The effective aperture is the physical aperture times the *aperture efficiency*, η. $A_E = \eta A_R$. A_E, is related to the gain like this

$$A_E = \frac{G_R \lambda_0^2}{4\pi} \quad \left[\mathrm{m}^2\right] \tag{4.6}$$

Insert (4.6) into (4.5) to get the *Friis transmission equation*

$$P_R = \frac{P_T G_T G_R \lambda_0^2}{(4\pi d)^2} = \frac{P_T G_T G_R}{(4\pi d/\lambda_0)^2} \tag{4.7}$$

The denominator in (4.7) is referred to as the *free space path loss*, L_P. The above equation can be expressed as a sum of dB values

$$\begin{aligned} P_R[\mathrm{dBW}] &= 10\log P_T + 10\log G_T + 10\log G_R - 20\log 4\pi d/\lambda_0 \\ &= \mathrm{EIRP}[\mathrm{dBW}] + G_R[\mathrm{dB}] - L_P[\mathrm{dB}] \end{aligned} \tag{4.8}$$

4.5.1 Atmospheric Loss

As the electromagnetic wave propagates through the atmosphere, some of the energy will be lost due to gaseous absorption. This absorption is frequency dependent and Fig. 4.4 shows total gaseous absorption for different elevation angles. The different peaks are at the resonance frequencies for

different gas molecules in the atmosphere. The increase in attenuation due to a decrease in elevation angle is caused by an increasingly longer signal path through the atmosphere.

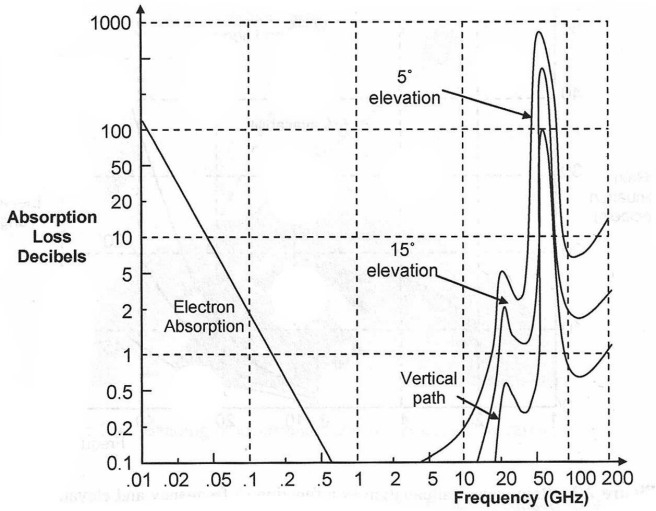

Figure 4.4: Gaseous absorption loss versus frequency for different elevation angles. Source [9].

From Fig. 4.4 one can see that the optimum frequency band to use for satellite communication, with respect to attenuation, is from about 500 MHz to 10 GHz. Additionally, rain attenuation is not significant for frequencies under 10 GHz [9].

The ionosphere which is a region of high electron content (plasma) in the atmosphere causes depolarization, this is referred to as the *Faraday Effect*. This effect causes attenuation unless the polarization of the receiving antenna is adjusted to compensate for the rotation. The depolarization has a $1/f^2$ dependence and its attenuation effect can be calculated using formula (4.9) from [9].

$$\text{Attenuattion [dB]} = -20\log\left(\cos\left(\Delta\Psi\right)\right) \tag{4.9}$$

where $\Delta\Psi$ is the *Faraday rotation* in degrees. The depolarization also creates a cross-polarized component

$$\text{XPD [dB]} = -20\log\left(\tan\Delta\Psi\right) \tag{4.10}$$

Another phenomena is *scintillation*, it causes rapid fluctuations in the signal amplitude, phase, polarization or angle of arrival (twinkling stars occurs

because of this effect). The origin of this effect is small changes in the refractive indexes of the atmosphere caused by local variations in ion concentrations. This can lead to multiple signal paths. When the signals are added together they can lead to the fluctuations (vector addition). Like the Faraday effect its frequency dependence is $1/f^2$ and has its maximum at around $\pm$ 25°around the equator, [9].

4.5.2 Noise

Satellite links are especially vulnerable to noise due to their inherent low power levels at the receiving end. Noise originates from cosmic background radiation, man-made noise and noise from system components.

Thermal noise is generated by random motion of atoms and electrons. As the temperature increases the average velocity of the particles increases. Since the motion is random the noise power is distributed over the entire frequency band, this is also referred to as *white noise* or *Johnson noise*.

In [9] it is derived from kinetic theory that the noise power, P_n, generated in a resistor is directly proportional to its absolute temperature, T, and the bandwidth, B.

$$P_n \propto TB = kTB \tag{4.11}$$

where
k = Boltzmann's constant = 1.38×10^{-23}J/K
From the above equation the *noise power spectral density*, P_{n0}, can be defined as

$$P_{n0} = kT \text{ [W/Hz]} \tag{4.12}$$

The *noise figure*, F, is defined as the ratio between the input SNR and the output SNR

$$F = \frac{S_i/N_i}{S_o/N_o} = \frac{N_o}{(S_o/S_i)\,N_i} = \frac{N_o}{GN_i} \tag{4.13}$$

Since $N_i = kT_iB$ the noise figure can be written as

$$F = \frac{N_o}{GkT_iB} \tag{4.14}$$

An actual amplifier will itself introduce some noise, ΔN. By adding the introduced noise, F becomes

$$F = \frac{GkT_iB + \Delta N}{GkT_iB} = 1 + \frac{\Delta N}{GkTiB} \tag{4.15}$$

If a device does not introduce any noise ($\Delta N = 0$) F would be equal to 1. Therefore, all actual devices will have a $F \geq 1$.

Another way to express noise performance is to use the *equivalent noise temperature*, T_e. If a device has an output noise power P_e, then the equivalent noise temperature is the temperature, T_e, that a resistor would need to be at in order to produce the same noise power. By substituting ΔN in (4.15) with GkT_eB the expression for F becomes

$$F = 1 + \frac{T_o}{T_i} \quad \text{or} \quad T_e = T_i\,(F - 1) \tag{4.16}$$

The antenna at the ground station on Earth will pick up noise from many different sources. The noise is dependent on the pointing direction and its side lobes. For a clear sky the noise temperature versus frequency is given for different elevation angles in Fig. 4.5.

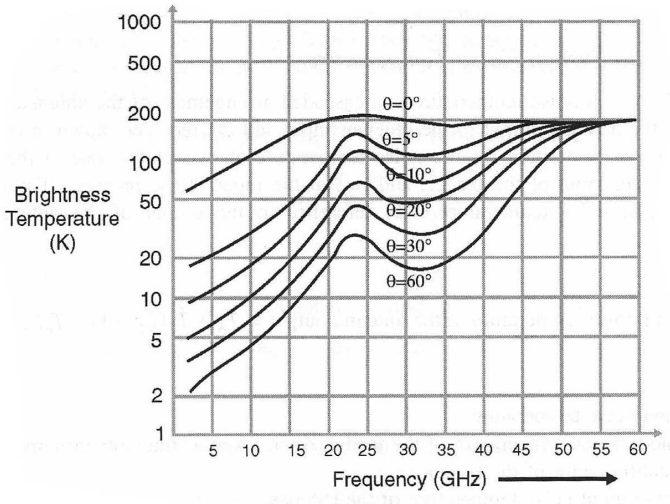

Figure 4.5: Brightness temperature for a clear sky for various elevation angles. Source [9].

4.6 Assumptions Made in This Thesis

- Circular sun-synchronous orbit at 800 km altitude
- $\pm 5^{\circ}$ pointing accuracy
- 1 W transmitting power
- 50% efficiency in the satellite antenna
- DQPSK-modulation
- BER = $10^{-}6$
- Receiving parabola of 2 m in diameter
- Receiver noise temperature of 500K
- One pass is equal to a optimal pass where the satellite orbits directly above the observer

The link budget that are made here serves primarily as a tool for evaluating different array solutions. A radio design would require a more detailed link budget with coding gain, link margin etc, but for a comparative analysis of different antenna solutions the link budget presented here should sufficient.

Assuming Circular Orbit	800 km Orbit Height and 98º inclination	
Carrier Frequency	5.83E+009	5.83E+009 [Hz]
Speed of Light	3.00E+008	3.00E+008 [m/s]
Carrier Wavelength	0.05	0.05 [m]
Earth Radius	6.38E+006	6.38E+006 [m]
Pi	3.14	3.14
Boltzmann's constant	1.38E-023	1.38E-023 [J/K]
Kepler Constant (Gme)	3.99E+014	3.99E+014
Path Parameters		
Elevation	75.67	59.22 [deg]
Orbit Height	800000	800000 [m]
Polarization Loss	3	3 [dB]
Ionospheric Attenuation	0	0 [dB]
Ionospheric Scintillation	0	0 [dB]
Slant Range	822709.55	913476.2 [m]
Maximum Doppler Shift	35841.25	73988.53 [Hz]
Time Visible	54.64	125.52 [s]
Ground Station Properties		
Antenna Diameter	2	2 [m]
Antenna Efficiency	0.6	0.6
Receiver Antenna Gain	39.52	39.52 [dB]
Noise Bandwidth	5.56E+006	4.20E+006 [Hz]
Antenna Noise Temperature	50	50 [K]
Antenna Receiver Noise Temperature	500	500 [K]
G/T	12.11	12.11 [dB/K]
Satellite Transponder Properties		
PA Output Power	0	0 [dBW]
Antenna SMA Connector Loss	0.5	0.5 [dB]
Coax Cable Loss	0.2	0.2 [dB]
PCB SMA Connector Loss	0.05	0.05 [dB]
Satellite Antenna Properties		
Antenna Efficiency	0.5	0.5
Satellite Antenna Gain	11.7	11.4 [dBi]
Modulation Parameters		
Bits per Symbol	2	2 [bits/symbol]
Symbol Rate	3.97E+006	3.00E+006 [Baud]
Eb/No Limit	1.06E+001	1.06E+001 [dB]
TOTALS		
EIRP	7.94	7.64 [dBW]
Free Space Loss	166.06	166.97 [dB]
Total Path Loss	169.06	169.97 [dB}
Received Power	-121.6	-122.81 [dBW]
System Noise Power	-133.75	-134.96 [dBW]
C/N	12.14	12.15 [dB]
C/No	**79.59**	**78.38 [dBHz]**
Eb/No	**10.6**	**10.6 [dB]**
Link Margin for Eb/No	**0**	**0 [dB]**
Received data amount	**54.23**	**94.18 [MB]**

Figure 4.6: Link budget based on the above assumptions.

Chapter 5

Antenna Element Design

The antenna elements will be designed as probe fed patch elements instead of microstrip line fed elements which were used in [1]. By choosing probe fed elements, the feeding network can be placed on a separate layer for itself with the ground plane between the feed layer and patch layer. By choosing this solution, greater freedom is allowed when designing the feed network. The feeding networks influence on the radiation diagram in the direction of the main beam will be greatly reduced, but the cost of this solution is increased complexity, thickness and weight. The stack-up that is intended to be used is described in Fig. 5.1.

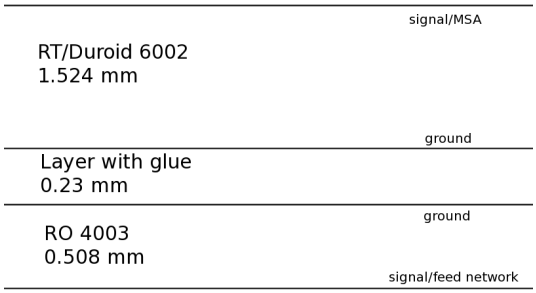

Figure 5.1: Stack-up that the antenna design will be based on.

The MSA should be engineered so that it will have its resonance frequency at 5.84 GHz, which is in the center of the allocated frequency band. The chosen substrate, RT/duroid®6002 (see App. B.1) has a h and ε_r as specified below.

- $\varepsilon_r = 2.94$
- $h = 1.524$ mm

- $\tan\delta = 0.0012$

The substrate was chosen because it is suitable for space applications (see App. B.4) and had satisfactory characteristics for a MSA design. This substrate was also used in [1] and a panel was purchased with the intent to be used in this thesis. It will also be matched to 100 Ω due to the feed network design (see chapter 7).

For the feed layer another space qualified substrate available from the board manufacturer (Elprint) was chosen, RO4003C (see App. B.2). This substrate has a higher dielectric constant and was chosen to be thinner than the patch layer in order to make the microstrip lines narrower and to save room and weight. The thickness of the adhesive layer was recommended by Elprint.

5.1 Design Based on MSA Models

As a starting point the simple analytical models has been used so that when more accurate software is put into play one will have a decent starting point.

5.1.1 Transmission-line Model

Based on the equations in section 2.3.2 the parameters given in Tab. 5.1 has been obtained.

Parameter	*Value*	*Units*
Width	18.3	mm
Length	14.28	mm
ΔL	0.74	mm
ε_{reff}	2.66	F/m
BW	260	MHz
BW	3.53	%
Directivity	6.5	dBi

Table 5.1: Results from a preliminary transmission-line model design.

5.1.2 Cavity Model

In order to have the TM_{010} as the dominant mode, the width should be smaller than the length (see (2.8)). By reducing the width to 10 mm, the procedure of calculating the length can begin. Inserting values for width, height and dielectric constant of the substrate into (2.3) results in a new

ε_{reff}. Equation (2.4) gives the extension of the physical length due to the fringing fields along the width of the patch. The physical length of the patch will then be

$$L = \frac{v_0}{2\,(f_r)_{010}\sqrt{\varepsilon_{reff}}} - 2\Delta L$$

Parameter	*Value*	*Units*
Width	10	mm
Length	14.64	mm
ΔL	0.72	mm
ε_{reff}	2.55	F/m
BW	260	MHz
BW	2.57	%
Directivity	6.5	dBi

Table 5.2: Results from the cavity model design.

5.1.3 Simulations in PCAAD 5.0

The PCAAD software [20] applies the cavity model when treating probe fed rectangular MSAs. Using the calculated values for width and length from Tab. 5.2 as input parameters in PCAAD results in $f_r = 5.70$ GHz.

By reducing the length of the patch so that the resonant length decreases and the resonance frequency increases, the desired center frequency can be obtained. The results are summarized in Tab. 5.3.

Parameter	*Value*	*Units*
Width	10	mm
Length	14.25	mm
f_r	5.84	GHz
BW	3.2	%
Efficiency	97.8	%
Directivity	6.4	dB
Probe-to-edge	4.62	mm

Table 5.3: Best result achieved for a MSA matched to 100 Ω with PCAAD.

5.2 Design of a Probe-fed MSA in EMDS 2006C

In the EMDS software [21] three dimensional models can be built and their EM behavior simulated. The different parts of the model is assigned physical properties that will affect the EM-field. This software applies the FEM when solving an EM problem which makes it capable to solve three dimensional problems. The FEM divides the structure into finite elements (tetrahedrons) and solves the problem for each finite element, these results are then combined to obtain the solution for the entire structure (see [22] for more information on the FEM).

When solving antenna problems in EMDS one should use radiation boundaries or as it is often called absorbing boundaries. For the radiating structure this will appear as the boundaries are open and the energy can radiate freely into space. For the radiation boundaries to work properly, they should be at least a quarter of a wavelength away from the radiating source. Having the radiation boundary further out does not produce any better result and will just consume more memory. According to [18] a ground plane that

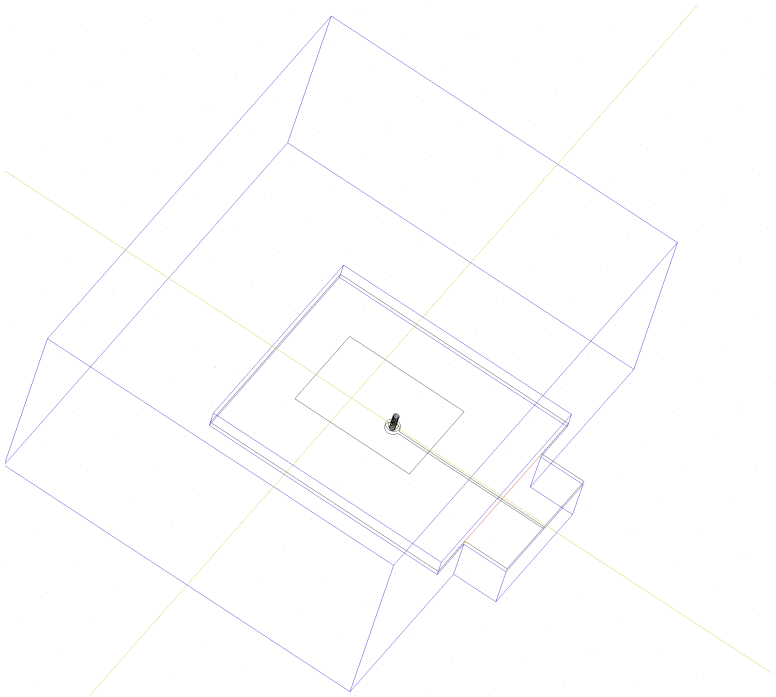

Figure 5.2: Geometry used in EMDS for a single patch. The feed line is 0.27 mm wide.

extends more than $\lambda_0/20$ out from the patch will not affect the resonance frequency compared to an infinite ground plane (the radiation diagram will

on the other side be affected). Having a ground plane smaller than this will increase the resonance frequency compared to an infinite ground plane.

As a consequence from the two previous paragraphs the ground plane will extend at least 2.6 mm out from the resonant structures and the radiation boundaries will extend 14 mm above and around radiating structures of interest.

The structure in Fig. 5.2 does not include the 0.23 mm thick adhesive layer between the two substrates. Simulations has been done where that layer has been replaced with an air gap between the two ground planes, but the difference in the simulation results was very small. It did however, consume more memory (more complex model) so that instead of 9 passes only 8 could be run. A comparison between two simulations with and without the adhesive layer (same amount of mesh refinement passes, 8) results in a S_{11} = -17.6 dB at 5.83 GHz (with adhesive layer) and S_{11} = -18.9 dB at 5.82 GHz. Having less refinement passes tends to result in a lower resonance frequency.

5.2.1 PCAAD Design Simulated in EMDS

As one can read from the graphs in Fig. 5.3 the suggested patch size from PCAAD and the cavity model is too large. Since this is a multilayer structure one should expect some difference in the result. The PCAAD calculations are based on the traditional probe fed solution where the inner conductor from a coaxial cable goes up through the substrate and is connected to the patch, while the solution presented here has a multilayer structure. The probe thickness and length also plays a role together with the annular ring where the probe goes through the ground plane.

5.2.2 EMDS Optimized Designed

With a patch size of 13.57x10 mm the simulations results in Fig. 5.5 are obtained. This MSA will be used further in the design process since it has the desired resonance frequency. To improve matching with the entire feed network when that is designed, it could be useful to modify the patch dimensions to some degree.

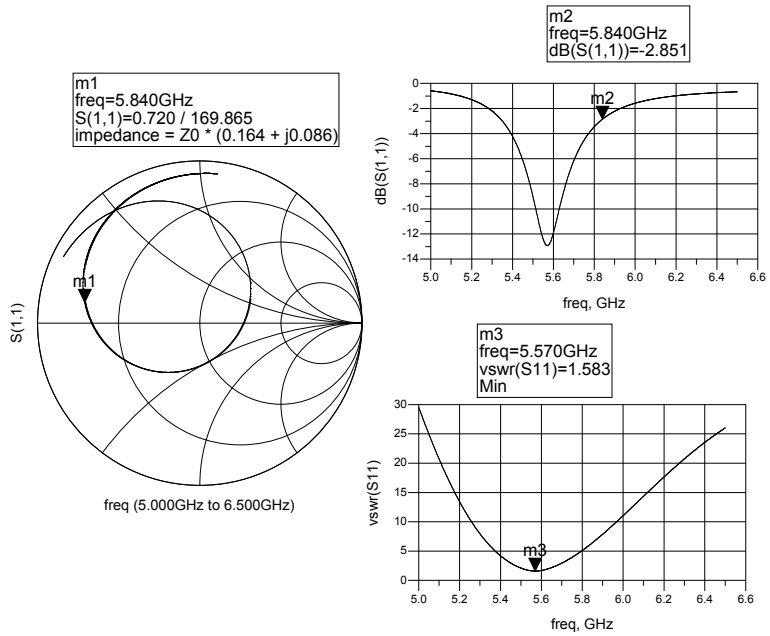

Figure 5.3: Simulation results from EMDS with the PCAAD patch design from Tab. 5.3.

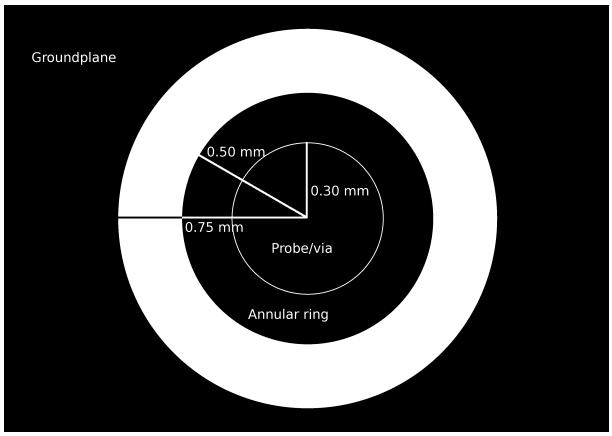

Figure 5.4: Shows how the feed probe goes through the ground plane. The annular ring serves as a adhesive point for the electroplated via.

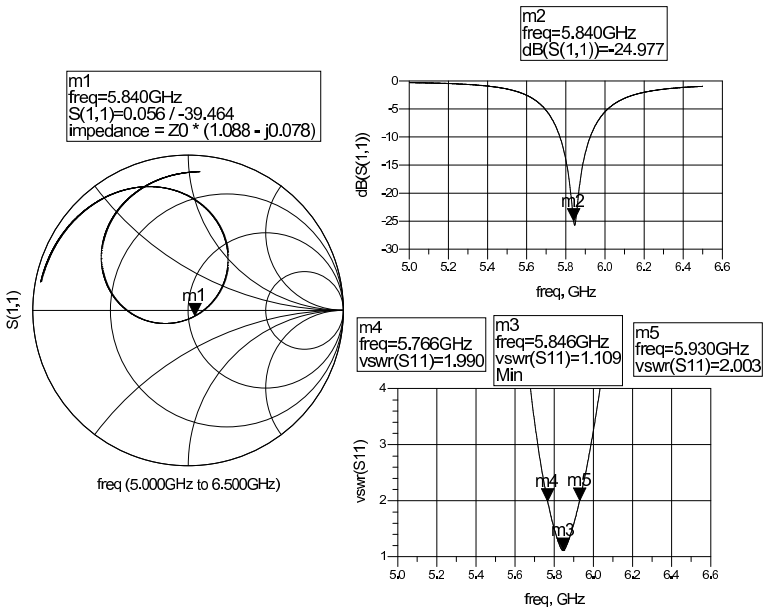

Figure 5.5: Simulation results from EMDS design in Tab. 5.4.

Parameter	*Value*	*Units*
Width	10	mm
Length	13.57	mm
f_0	5.846	GHz
BW	2.8	%
Efficiency	96.1	%
Directivity	6.7	dB
Probe-to-edge	4.81	mm

Table 5.4: MSA to proceed with. Results for EMDS simulation.

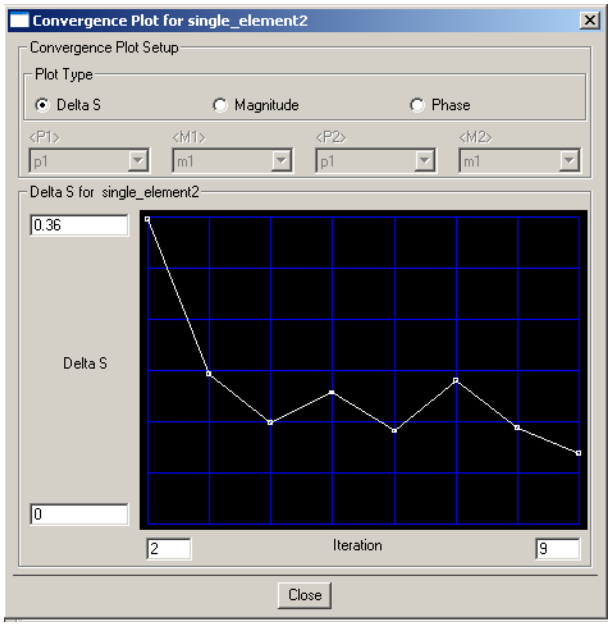

Figure 5.6: Convergence plot for the single element EMDS simulation.

Chapter 6

Array Design

As explained in [1], the best suited array solution seems to be a 2x2 MSA array with 5 switchable beams situated at the nadir side of the satellite. In [1] only a rectangular array like in Fig. 6.1 was explored. In this thesis two additional solutions will be explored and the best solution with regards to size, complexity, directivity and beamwidth will be chosen. Transferred data has been calculated with the link budget at the assumption of a constant bitrate, where the lowest directivity within the beamwidth dictates the bit rate with a link margin of 0 dB. It is also desirable to design the array so that a camera could be placed at the center of the array (diameter of maximum 2 cm).

6.1 Uniform Rectangular Array (Conf. #1)

The geometry in Fig. 6.1 provides a close to omnidirectional radiation pattern (Fig. 6.2) in the xy-plane or azimuth-plane (ignoring the side lobes). The inter-element distance of 36 mm or 0.7 free space wavelengths at 5.84 GHz results in a directivity of 13.4 dBi. Since the two symmetry planes along the x- and y-axis are not equal to each other (not square patches and the polarization is the x-direction) the array will not give the same radiation diagram when steering the beam in x- and y-directions. The symmetrical placement of the radiating elements allows for a 1 bit phase shifter to steer the beam in 5 directions. There are also symmetry lines between the centers of element 1 and 4 and between elements 2 and 3, but steering beams along theses lines would demand a 2 bit phase shifter.

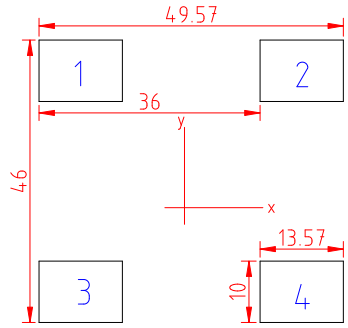

Figure 6.1: Geometry of the uniform rectangular array solution with a spacing of 36 mm

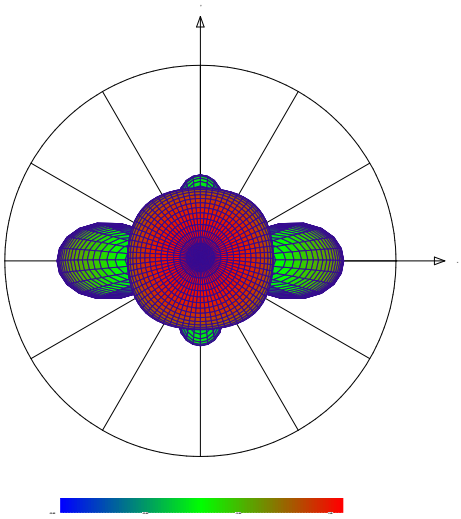

Figure 6.2: Volumetric radiation plot of the boresight beam from configuration #1

6.2 Rectangular Array with a Modified Grid Angle (Conf. #2)

The array described above can be modified by changing the grid angle, see Fig. 6.3. A rectangular array has a grid angle of 90°, but when this angle, α is changed to $\neq 90°$ the elements are shifted along the x-axis (from rectangle to parallelogram). Since changing the grid angle results in a "stretching" of the array, the same effect is observable in the radiation pattern. Setting the grid angle to 0° will result in a one dimensional linear array. This configuration result is a higher maximum directivity (13.7 dBi), but due to the lack of symmetry in this solution it will not be sufficient with a 1 bit phase shifter. Additionally, the radiation pattern is rather narrow so that the downloaded data will be highly dependent on the satellites orientation along its yaw-axis.

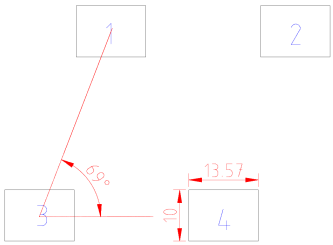

Figure 6.3: Shows the geometry of an array with a grid angle, α, of 69°

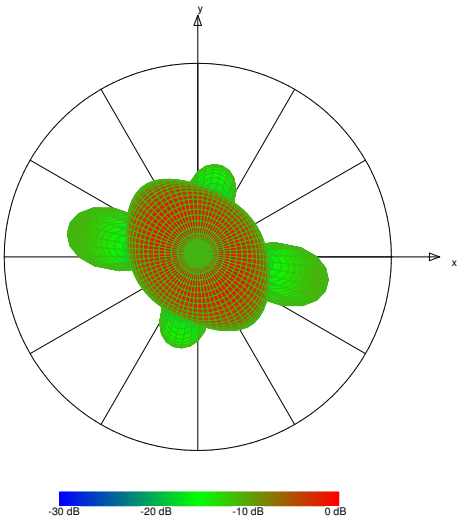

Figure 6.4: Volumetric radiation plot of the boresight beam from configuration #2

6.3 Rectangular Array with Rotated Elements (Conf. #3)

Since it is beneficial to have an array with identical beams that would lower the dependency on the satellites orientation around its yaw-axis, the solution in Fig. 6.5 has been proposed. This configuration is basically the same as configuration #1, but here the MSA elements has been rotated 45 degrees making the configuration able to function with only one phase delay and still achieve the same beams in four directions. Maximum directivity is the same as in configuration #1, 13.4 dBi (the inter-element distance remains unchanged). The symmetry is around the two axes in Fig. 6.5. By steering the beam out along the axes of symmetry, identical beams can be accomplished.

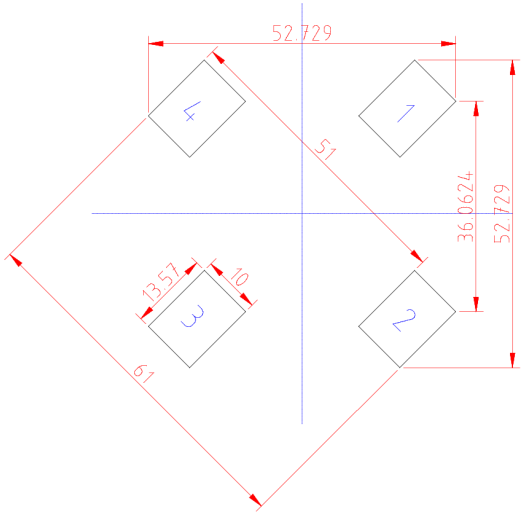

Figure 6.5: Geometry of configuration #3. The blue lines represents the lines of symmetry

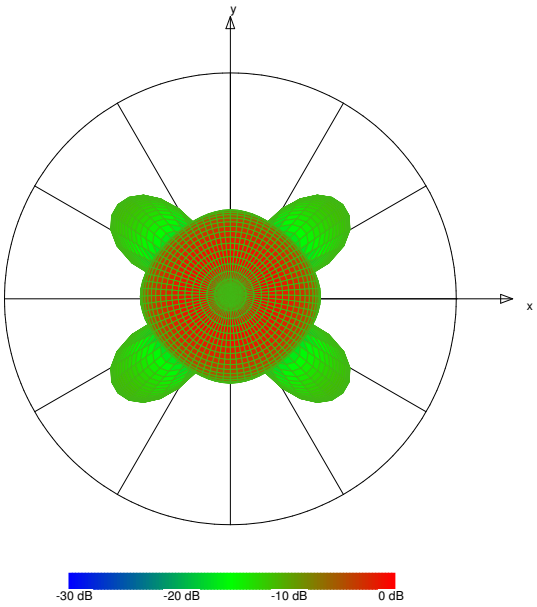

Figure 6.6: Volumetric radiation plot of the boresight beam for array configuration #3

6.4 Selecting Array Geometry

When reviewing the proposed solutions, configuration #2 pretty clear distinct itself as the least attractive alternative. It has a narrow radiation diagram and it would need a more complex phase shifter and feed network than the two other solutions. These characteristics makes this configuration less attractive even though it can offer a higher directivity than the two other configurations.

Configuration #1 can be utilized in two ways as described in 6.1. Since the one where identical beams can be achieved demands more than one phase delay, it will be discarded. This leaves configuration #3 and the single phase delay option from configuration #1 as the two viable options.

A suitable looking angle, Θ_0, to steer the beams out to, seems to be around 20 - 25 degrees which results in a directivity of around 10-12 dBi. To compare the two solutions that are left, the directivity at the point where the steered beam (looking angle of $\theta_0 = 25°$) radiation diagram intersects with the boresight beam has been used as a reference directivity. From Fig. 6.7 it can be read that when the beam is steered out to $\theta_0 = 25°$ the radiation diagrams intersects at around 16° with a directivity of 11.2 dBi. The corresponding numbers from Fig. 6.8 and 6.9 are both 15° and 11.7 dBi. For a quick comparison of the remaining configurations the effective beamwidth

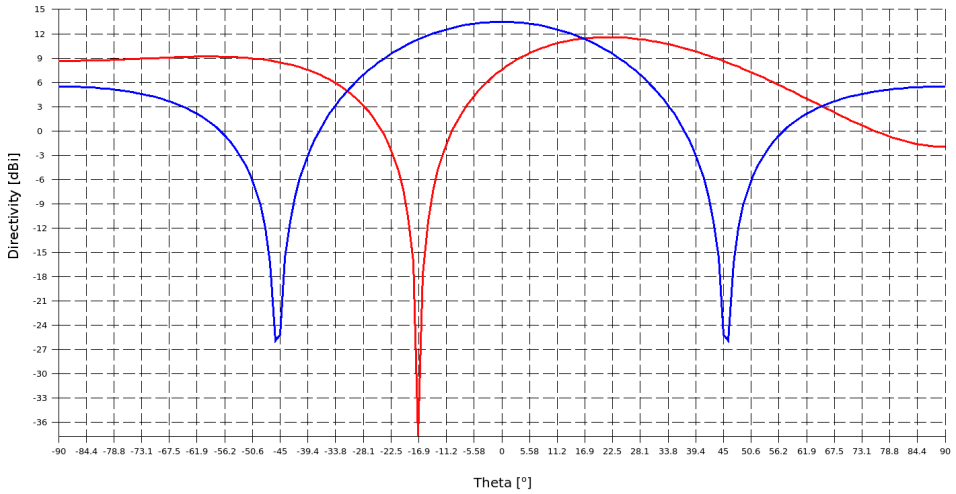

Figure 6.7: $\phi = 0°$ cut of the radiation diagram from array configuration #1. Blue = boresight beam, red = beam steered to $(\theta_0 = 25°, \phi = 0°)$

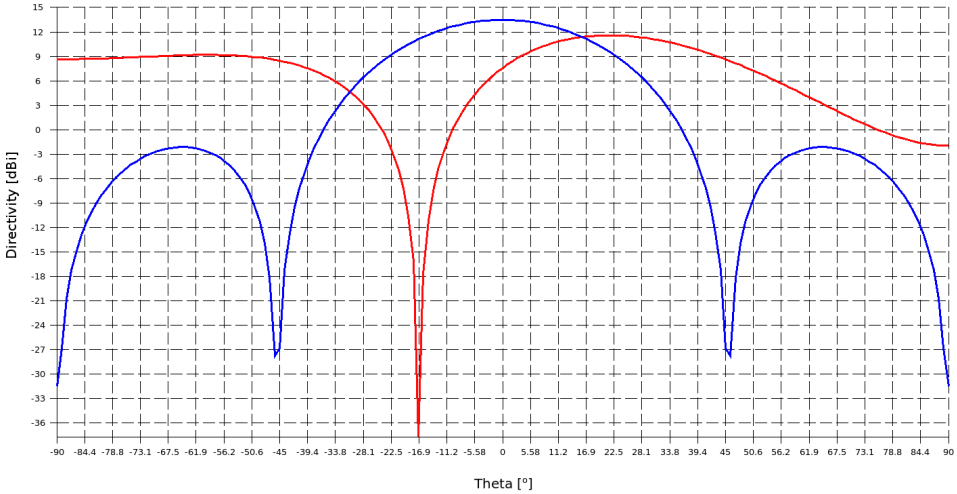

Figure 6.8: $\phi = 90°$ cut of the radiation diagram from array configuration #1. Blue = boresight beam, red = beam steered to $(\theta_0 = 25°, \phi_0 = 90°)$

achievable with the directivity at the switching point (when looking out to $\theta_0 = 25°$) has been inserted into the link budget. This has been done for looking angles between 20 to 25 degrees.

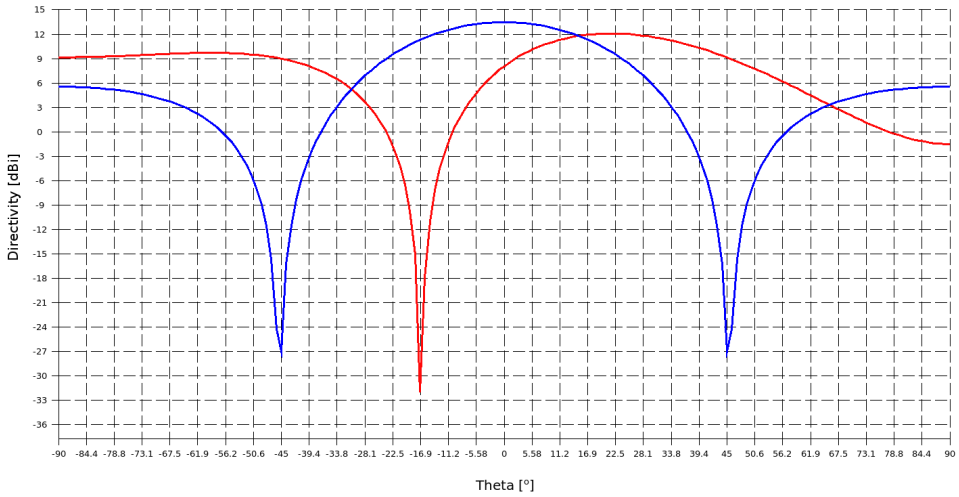

Figure 6.9: $\phi = 0°$ cut of the radiation diagram from array configuration #3. Blue = boresight beam, red = beam steered to $\theta_0 = 25°, \phi_0 = 0°$

θ [°]	BW[°],$\phi = 0°$	$Data$[MB]	BW[°],$\phi = 90°$	$Data$[MB]	Avg[MB]
25	56.0	80.2	57.0	93.0	86.6
24	56.6	81.1	64.4	90.3	85.7
23	57.0	81.6	63.8	89.7	85.7
22	57.0	81.6	64.4	90.3	89.0
21	58.6	83.6	63.8	89.7	86.7
20	58.2	83.1	62.2	87.8	85.5

Table 6.1: Performance data for array configuration #1, minimum directivity of 11.2 dBi

Since configuration #1 has such a large difference in its beams the average data amount has been calculated and will be used as the basis for comparison.

As it can be read from Tab. 6.1 and 6.2, configuration #3 provides the greatest capability in terms of downloaded data. This solution is also slightly less influenced by how satellite is oriented along its yaw-axis. In terms of square centimeters, configuration #1 is slightly smaller than configuration #3. Both configurations also has room for a camera at the center (at least before the feed network is in place). The best suited solution can therefore be said to be configuration #3.

θ [°]	BW [°], $\phi = 0°$	$Data$ [MB]
25	58.4	93.5
24	56.6	91.0
23	56.8	91.2
22	56.8	91.2
21	56.8	91.2
20	56.4	90.7

Table 6.2: Performance data for array configuration #3, minimum directivity of 11.7 dBi

To get the most out of array configuration #3 it is important to find which looking angle is the optimum one to steer the beams out to. and also how large the beamwidth should be. For a given looking angle there will be a maximum directivity given by the point where the radiation diagrams intersects each other. By setting this directivity as maximum directivity dips in the overall radiation diagram for the switched beam configuration can be avoided. The minimum directivity can be lowered so that the beamwidth and visibility time increases, effectively increasing the coverage area. By increasing the beamwidth, the elevation angle needed to "see" the satellite is decreased and the slant range will be increased. However, at some point the increased distance that increases the free space propagation loss, that along with the decreased directivity will counteract the effect of an increased visibility time (see plots in App. E). The atmospheric losses and antenna noise temperature will also increase with the decrease in elevation angle. In an effort to find the optimum trade off between looking angle, directivity and data transferring capability the tables below has been made. For each looking angle (from $\theta_0 = 26°$ to $\theta_0 = 20°$) the maximum directivity is given by the point of intersection between the radiation diagrams. In steps of 0.2 dB from maximum directivity down to 11.0 dBi the maximum beamwidth and corresponding download capability has been found and tabulated.

From Tab. 6.3 the looking angle that results in the largest beamwidth for each step in directivity has been inserted into the link budget in Fig. 4.6 and downloaded data amount has been calculated in Tab. 6.4

From Tab. 6.4 it can be read that the best trade-off between looking angle and directivity is $\theta_0 = 25°$, with a directivity of 11.4 dBi. This solution will, according to PCAAD, require a phase delay of 106.8° for two elements at the time.

D [dBi]	*Looking angle and corresponding beamwidths*[°]						
	20°	21°	22°	23°	24°	25°	26°
12.2	47.0	46.0	-	-	-	-	-
12.0	51.4	51.2	50.6	-	-	-	-
11.8	55.0	55.0	55.0	54.8	-	-	-
11.6	58.0	58.4	58.6	58.8	58.6	60.4	60.2
11.4	60.6	61.2	61.6	62.0	62.2	64.2	64.2
11.2	63.0	63.8	64.4	65.0	65.4	67.2	67.6
11.0	65.4	66.2	66.8	67.6	68.2	70.0	70.6

Table 6.3: Directivity with corresponding beamwidth for different looking angles, θ_0

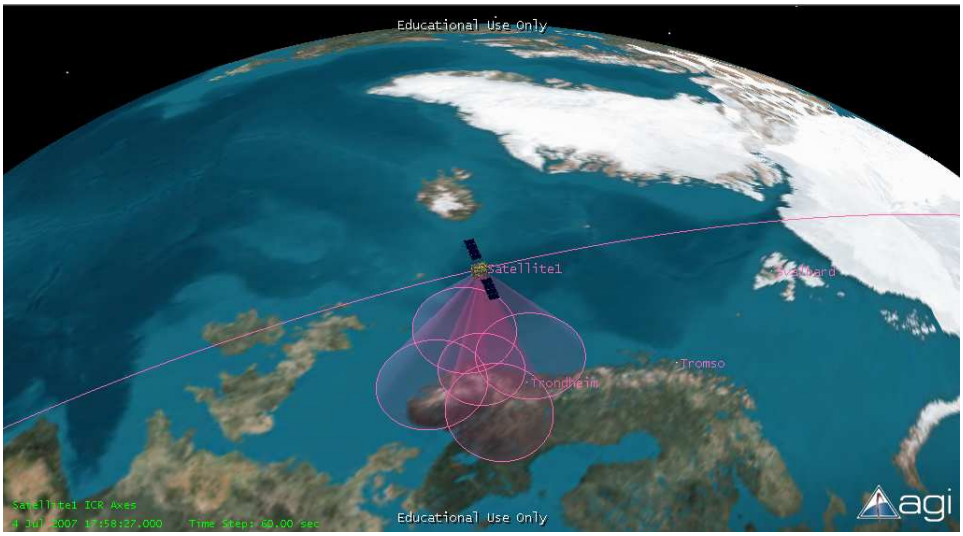

Figure 6.10: An approximate view of the coverage area array configuration #3 can offer

D [dBi]	θ_0 [°]	BW [°]	*Data* [MB]
12.2	20	47.0	84.8
12.0	20	51.4	89.0
11.8	20	55.0	90.6
11.6	25	60.4	94.1
11.4	25	64.2	94.4
11.2	26	67.6	93.5
11.0	26	70.6	92.0

Table 6.4: Directivity with corresponding beamwidth for different looking angles

The array configuration will then be

- Configuration #3
- Switch to/from the boresight beam at $\theta = 15°$. That means that the boresight beam will only be active when the satellite is at an elevation angle greater than 79.2°
- Maximum effective beamwidth of 64.2°, activate link when the elevation angle is grater than 59.2°
- Maximum link duration of 2 min 5 s
- 6 Mbps datarate (with conditions like in the link budget in Fig.4.6)

To steer the beam in the right directions the phase delays must be applied to the right elements. With Fig. 6.5 as the reference geometry four beam directions can be defined

- Right beam - towards right on the page, $\phi_0 = 0°$
- Forward beam . towards the top of the page, $\phi_0 = 90°$
- Left beam - towards left of the page, , $\phi_0 = 180°$
- Backward beam -toward the bottom of the page, $\phi_0 = 270°$

Beam	Element delay			
	1	2	3	4
Right	106.8°	106.8°	0°	0°
Forward	106.8°	0°	0°	106.8°
Left	0°	0°	106.8°	106.8°
Backward	0°	106.8°	106.8°	0°

Table 6.5: Map of phase delay for the different beams

6.4.1 Configuration #3 Simulated in EMDS

Simulating the array in EMDS demands a lot of memory which prevents the simulation to converge (see Fig. 6.12). This again, prevents EMDS to be used as a design tool for the feed network. However, the radiation diagram and directivity calculations should not be too far from the truth, so in Fig. 6.11 there is a plot that compares the radiation diagram from PCAAD with EMDS. The EMDS simulation results in a directivity of 13.1 dBi. As it should be expected, the directivity is reduced some compared to the PCAAD numbers since PCAAD operates with an infinite ground plane.

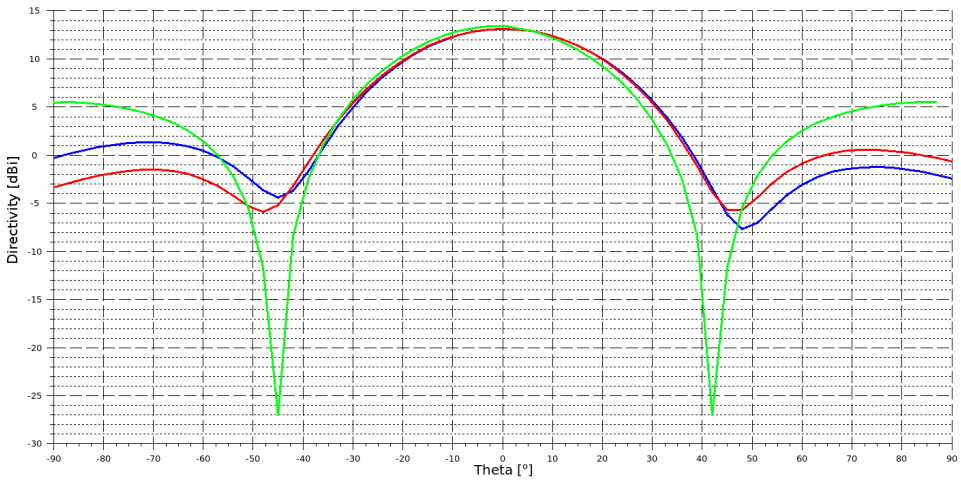

Figure 6.11: Red and blue are cuts form the EMDS radiation diagram while the green line is from PCAAD

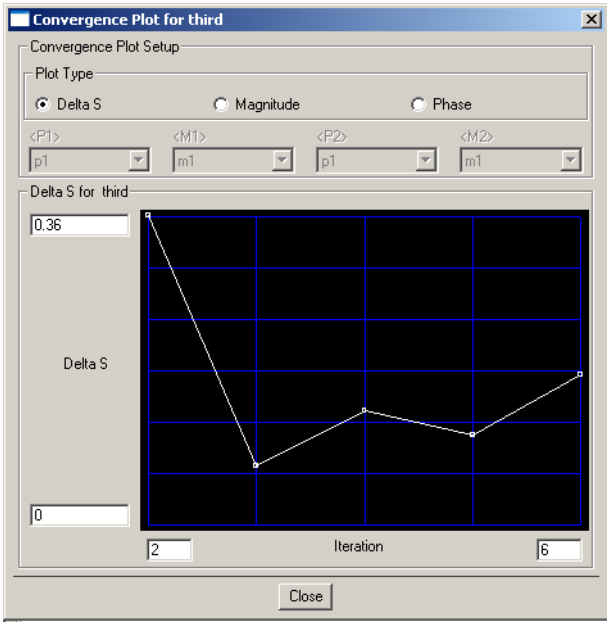

Figure 6.12: Convergence plot for the array simulation in EMDS

Chapter 7

Feed Network Design

The feed network has been designed so that the signal path to each element has the same waylength. Low loss and available area for a camera has also been prioritized. The design rules from Elprint [23] should also be followed. The cheapest option in the set of design rules has been chosen. To limit crosstalk between microstrip lines a minimum distance between lines has been set to two times the substrate height of 0.508 mm.

7.1 Feed Layout

The most ideal placement for the array would be at the center of the nadir side of the satellite (symmetry considerations for the radiation diagram). It also desirable to have a camera at this surface. To allow room for a camera at the center of the array the feed lines must be placed at the periphery of the array like in Fig. 7.1. The input should be matched to 50 Ω since it will be connected to other RF equipment. As a consequence of this, the microstrip lines out from the first tee-junction should have a width corresponding to 100 Ω. The two lines out from the tee-junction is seen as two parallel lines from the input line and their impedance is explained by the equations below.

$$
\begin{aligned}
Z_{in} &= \frac{Z_1 Z_2}{Z_1 + Z_2} \\
Z_1 &= Z_2 = Z_L \\
Z_{in} &= \frac{Z_L^2}{2Z_L} = \frac{Z_L}{2} \\
Z_L &= 2Z_{in}
\end{aligned}
$$

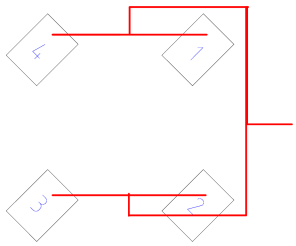

Figure 7.1: Principle sketch of how the feed network should be.

7.2 Static Feed Network

ADS 2008 Update 2 [24] has been used as the CAD software for the feed network design. As a first step the LineCalc tool in ADS has been used to find line widths and lengths. The microstrip line circuit has then been simulated in ADS and the line dimensions has been tuned till satisfying results has been obtained.

The first part of the feed network is the 50 Ω line splitting into two 100 Ω lines. The circuit in App. F.1 has been used to simulate the split.

LineCalc suggest these widths for the lines:

- 50 Ω lines - 1.14 mm
- 100 Ω lines - 0.26 mm

After tuning the circuit the final line widths has been set to:

- 50 Ω lines - 1.14 mm
- 100 Ω lines - 0.27 mm

Since the feed network needs one more tee-junction along the signal path (see Fig. 7.1) and the current line impedance is 100 Ω. The lines out from the last tee-junction will then need to have a width corresponding to 200 Ω if no countermeasures are taken. According to LineCalc a 200 Ω line will be 0.006 mm wide. This is too narrow to be used and a clear violation of the design rules that limits the line widths to 0.15 mm (cheapest option). One way to avoid this problem is to equip the feed network with quarter wave transformers that can take the 100 Ω lines back to 50 Ω lines. All the tee-junctions will then have the same dimensions and characteristics. By inserting $Z_{in} = 50\Omega$ and $Z_L = 100\Omega$ in (3.5) the characteristic impedance of the quarter wave transformer can be calculated to be 70.7 Ω. The LineCalc tool suggest the quarter wave transformer should be 0.60 mm wide and 8.10 mm long. The new simulation circuit in App. F.2 now includes a quarter wave transformer on each arm. As can be observed from the S_{11}-plot in

App. F.2 the match is not optimal at 5.84 GHz. The transformer should have been 8.34 mm long instead of 8.33 mm, but when a 50 Ω line is added to the transformer 8.33 mm gives the best results.

Dimensions for a quarter wave transformer with characteristic impedance of 70.7 Ω and a center frequency at 5.84 GHz:

- Line width: 0.6 mm
- Line length: 8.33 mm

The components in App. F.2 that are called MLIN accounts for the effect that a change in microstrip width has (basically a series inductance).

In Fig. 7.1 one can see that two right angle bends are needed in each main branch of the feed network. Designing a bend in a microstrip circuit should be given some attention. A bend will affect the characteristic impedance of the line by introducing a shunt capacitance. To minimize this effect a component called MSABND_MDS has been used. The component is a mitred bend which basically is a right angle bend that has had its corner chopped off. The larger the mitre factor, M = X/D, is the more of the corner gets chopped of as illustrated in Fig. 7.2.

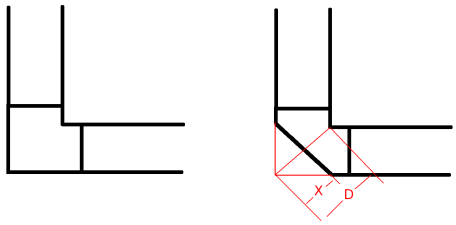

Figure 7.2: Cornered bend to the left and a mitred corner to the right.

The circuit and corresponding simulation results used to find the optimum value for M is given in App. F.3. The best results are obtained with M = 0.37.

The remaining parts of the feed network (disregarding the phase shifters) is just reuse of elements described above. The probe and vias related to the antenna has been simulated in EMDS so the effects of those are included in the S-parameters files from EMDS. By terminating the feed network in 100 Ω terminations the loss through the feed network can be found. Ideally S_{21}, S_{31}, S_{41} and S_{51} should be identical and equal to -6 dB (four branches in the network). The bottom right S-parameter plot in App. F.4. gives identical S-parameters (as could be expected, since the branches are identical), but there is a loss of 0.2 dB in each branch compared to a lossless network.

The S-parameters from the EMDS simulation can be exported to touchstone

format which can be read by ADS. It is important to be aware of the fact that EMDS normalizes the exported s-parameters to 50 Ω. Touchstone files can be used in ADS simulations through the S1P component (one port s-parameter data file). To get a correct simulation one would have to change the impedance in the touchstone file to the impedance which the EMDS simulation is calibrated to, in this case 102 Ω. By terminating the circuit in App. F.4 in a S1P component with the simulation results from the antenna described in Tab. 5.4 as input, the results in Fig. 7.3 are obtained.

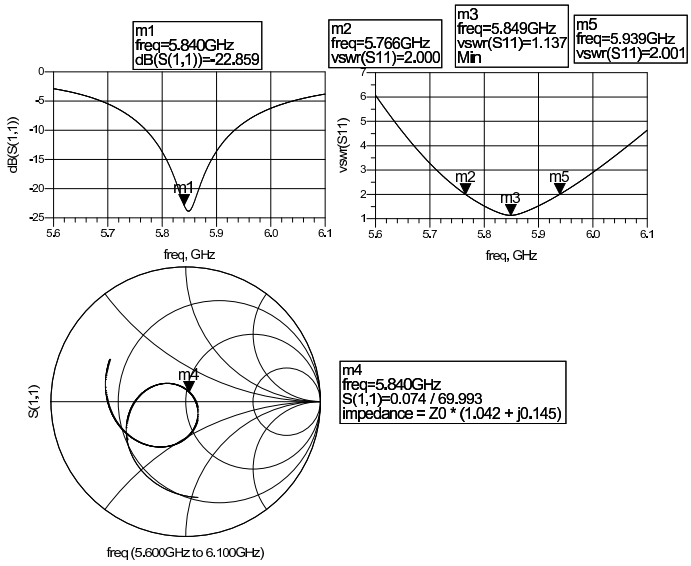

Figure 7.3: Simulation results for the feed network terminated in the MSA from Tab. 5.4.

7.3 Phase Shifter

In chapter 6 it was found that a phase shift of 106.8° was needed. The phase shifter should also be electronically controlled for remote operation. In [2] a 3 bit phase shifter has been developed. It consists of three delay elements at 45°, 90° and a 180°. The design is a switched-line configuration with a bandwidth of 1 GHz around 6 GHz. The idea is to modify the the 90° delay section into a 106.8° delay. As a switching device the PIN-diode in App. C has been used, making the phase shifter electronically controllable. The lines that have been used in [2] has a width of 0.3 mm which corresponds to an impedance of 115 Ω, this is in good correspondence with the feed network designed in the previous section which has line widths of 0.27 mm and a characteristic impedance of 100 Ω. The design from [2] has been followed and modifications has been made where it is required.

7.3.1 Switched Line Design

The PIN-diode is no ideal switch so there will be some signal leakage through the diode when it is in "off-mode" (reverse bias), it acts a small capacitance. So if the the waylength in the "off-direction" is equal to half a wavelength or multiples of that, resonance will occur and there will be large in phase and increased loss. The capacitance also works as an electrical extension of the physical line. These effects are discussed in greater detail in [2] where a MATLAB script is given that plots phase and loss as a function of the length of the reference line which is in "off-mode".

The MATLAB script has undergone some minor modifications by the author of this thesis and is given in App. D. The script has been used to find a suitable length of the reference line. The delay line will have a length equal to the reference length plus the length of the delay. In Fig. 7.4 and 7.5 it can be observed how the phase delay and loss is affected by the length of the reference line.

The electrical reference length has been chosen as 105°, making the delay line 211.8° long. As can be seen in Fig. 7.4 and 7.5 a reference length of around 70° will distort the phase and loss. The reference length should therefore be chosen either under or above this area. For this design a point above the "distorted" area has been chosen. The microstrip bends and pads for the diodes has not been taken into account when calculating the length of the reference line, it will therefore be a bit longer than the sum of the straight transmission lines (1 degree corresponds to roughly 0.1 mm). By placing the reference line length above the point where resonance occurs in the region where the curve is flat makes for a safer choice. Having a longer reference line will just increase the loss and cause conflict with the DC-feed in the final layout as can be seen in Fig. 7.8. The two different signal paths has been simulated in ADS and the simulation results are presented in App. F.5

Parameter	*Theoretical*	*Simulated*
Reference [dB]	0.7	0.6
Delay [dB]	0.7	0.8
Phase delay [°]	106.8	106.7

Table 7.1: Comparison of theoretical loss and phase calculations and ADS simulation for the switched line circuit.

From Tab. 7.1 one can see that theoretical calculations from the MATLAB script in App. D agrees well with the ADS simulations.

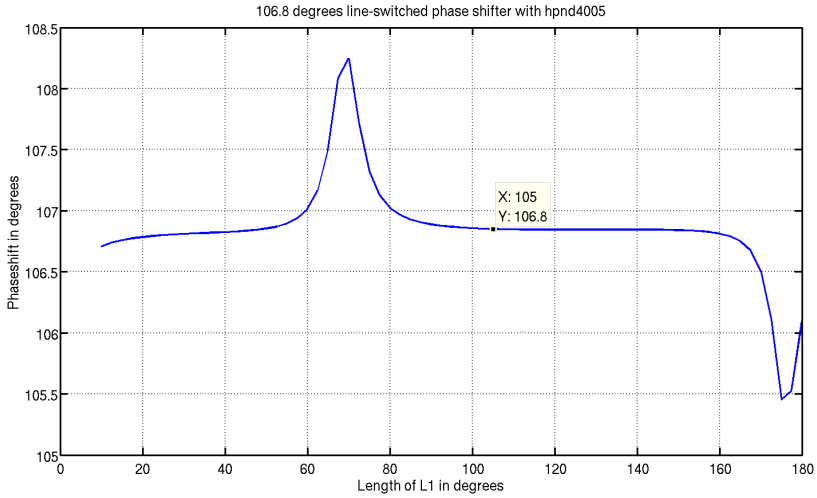

Figure 7.4: Phase delay versus length of the reference direction, L1.

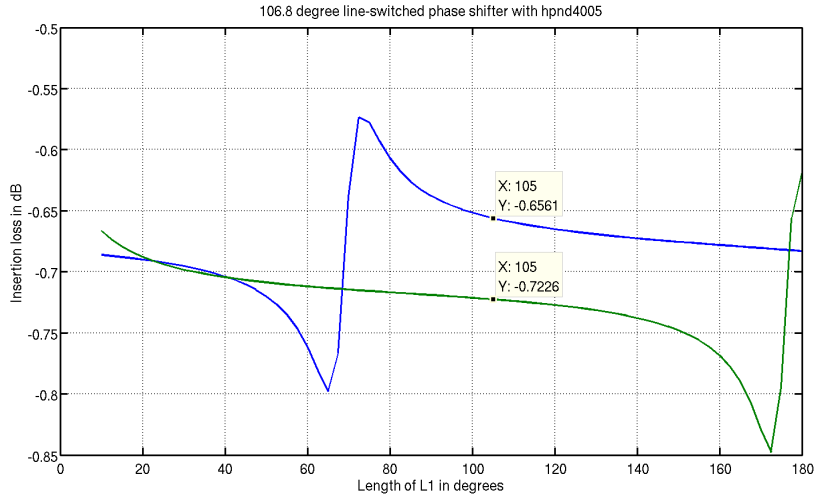

Figure 7.5: Insertion loss versus length of reference direction. Blue = reference, green = delayed.

7.3.2 DC Network

For the PIN-diodes to conduct they require a bias voltage/current. When applying DC to a RF network it is important to keep the DC current from flowing into the RF circuit and keeping the RF power from leaking out. The circuit in Fig. 7.6 illustrates a common way to do this. The DC block capacitor will be an open circuit at DC ($Z = 1/j\omega C$) and a short circuit at RF. The RF choke inductor will act as an open circuit for RF ($Z = j\omega L$) and as a short circuit for DC.

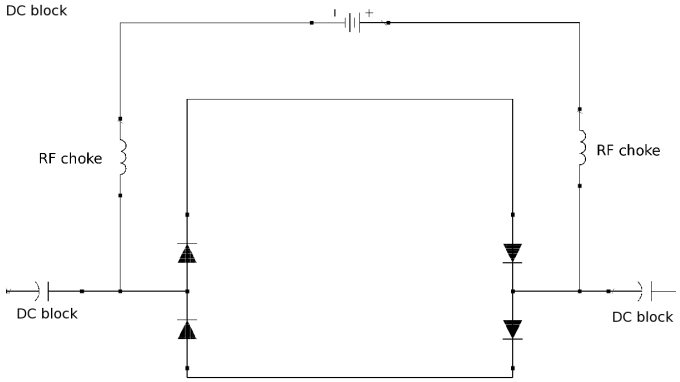

Figure 7.6: Principle sketch of the DC network.

To switch between the reference line and the delay line the polarity of the voltage source must be switched. In [2] it is suggested to use a voltage that gives a current of 20 mA over the diodes. Instead of using an inductor as the RF choke, two quarter wave transformer can be used. In Fig. 7.7 transformer 1 transforms from open to short circuit towards the RF line. Transformer 2 then transform from short circuit to open line at the RF line. This means that the RF circuit will regard the DC feed as an open line so that RF power does not leak into the DC network, but DC will flow into the RF line and over the diodes. The DC block capacitors on the RF line keeps the DC from going any further. Since the phase shifter design in [2] is a broadband design the DC network has been designed with that in mind. That is why transformer 2 is as narrow as the design rules will allow, 0.15 mm, while transformer 1 is wide and has a fan layout. All these measures to ensure broadband operation is probably not required for the design in this thesis, but it makes for an easier design process just to follow the design in [2]. From the S_{31} and S_{41} plots in the bottom right plot in App. F.6 one can see that there is very little RF leakage.

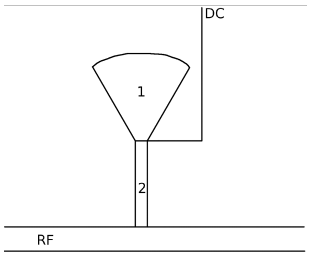

Figure 7.7: RF choke replacement.

7.3.3 Simulations of the Phase Shifter Design

By inserting the line switcher and DC network into the feed network (replacing the 0.27 mm line between the last tee-junction and the patch) the circuit characteristics seen from the patch elements and the array feed can be found. The simulation circuit is just the switched line design and the DC-network added together. Simulations results can be found in App. F.6.

Parameter	*Reference*	*Delay*
Reflection coefficient [dB]	16.3	21.6
Loss [dB]	0.9	1.0
Phase delay [°]	-	107.0

Table 7.2: Simulation results from just the phase shifter (line switcher plus DC network).

Parameter	*Reference*	*Delay*
Reflection coefficient [dB]	15.9	20.1
Loss [dB]	1.1	1.2
Phase delay [°]	-	108.4

Table 7.3: Simulation results from the feed network with the phase shifter integrated.

Beam	Elements			
	1	2	3	4
Right	1.7	1.7	0.5	0.5
Forward	0.7	1.5	1.5	0.7
Left	0.5	0.5	1.7	1.7
Backward	1.5	0.7	0.7	1.5

Table 7.4: Loss in dB for each element for specific beam directions. Loss plots can be found in App. F.8 and the corresponding phase delays are given in Tab. 6.5.

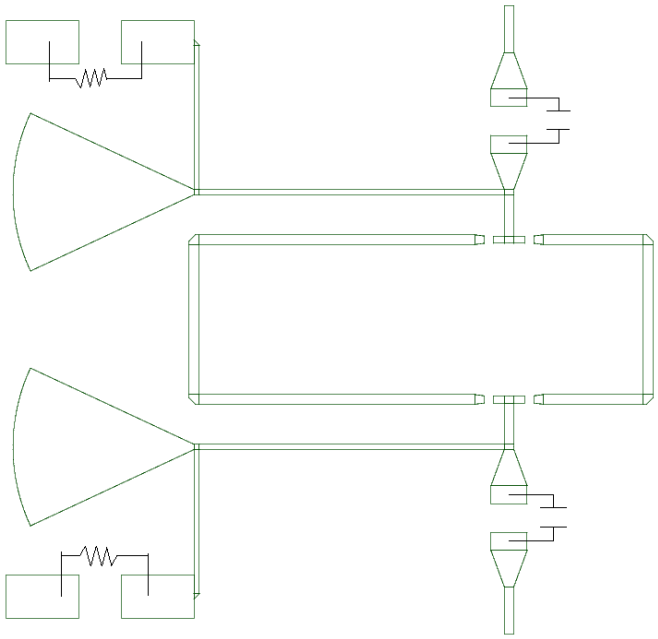

Figure 7.8: Layout for the phase shifter with discrete components in the DC network.

7.4 Matching MSA Elements to the Feed Network

From the feed layout sketch in Fig. 7.1 one can see that the patches must be rotated 45° relative to the feed. By introducing the phase shifter circuitry to the feed network one effectively ends up with different feed network characteristics for different phase shifter states (see App. F.8). It is therefore necessary to design the patch so that it will work satisfactory to the different states of the phase shifter.

Rotating the patch 45° with respect to the feed line has a negligible effect (resonance frequency increases 7-8 MHz) on the matching since via/probe and via pads have rotational symmetry.

The S-parameters that has been exported to touchstone format is imported into ADS by using the S1P component. The feed network is terminated in the S-parameters from EMDS. Using the rotated version of the solution from Tab. 5.4 results in the plots in Fig. 7.9 and 7.10. This patch design clearly favors the delay line state of the phase shifter. From the VSWR and S_{11} plots one can see that to even out the differences between the two states the resonance frequency should be decreased. By increasing the resonance length to 13.6 mm a better trade off is achieved with the results in Fig. 7.11 and 7.12.

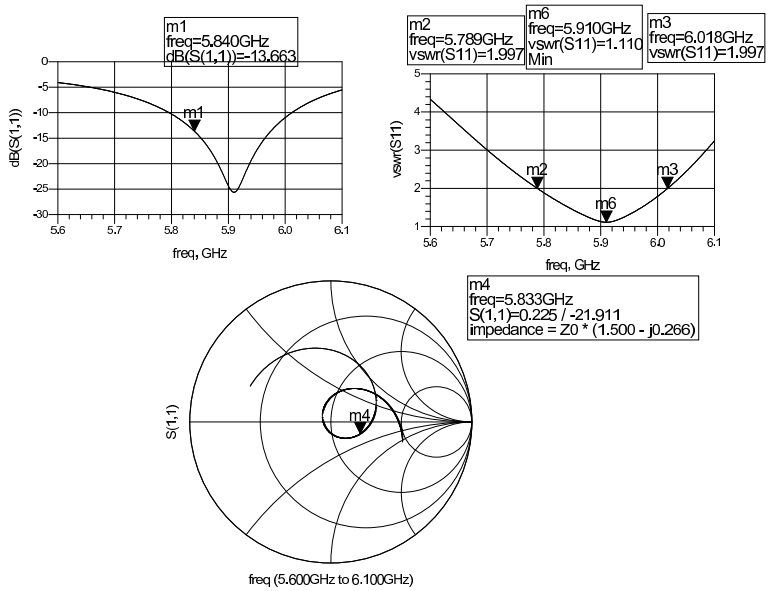

Figure 7.9: Simulation results from ADS with the MSA from Tab. 5.4, all phase shifter are in the reference state.

Under normal operation of this array the phase shifters will only be in the same state when the boresight beam is activated. If this is to be along the

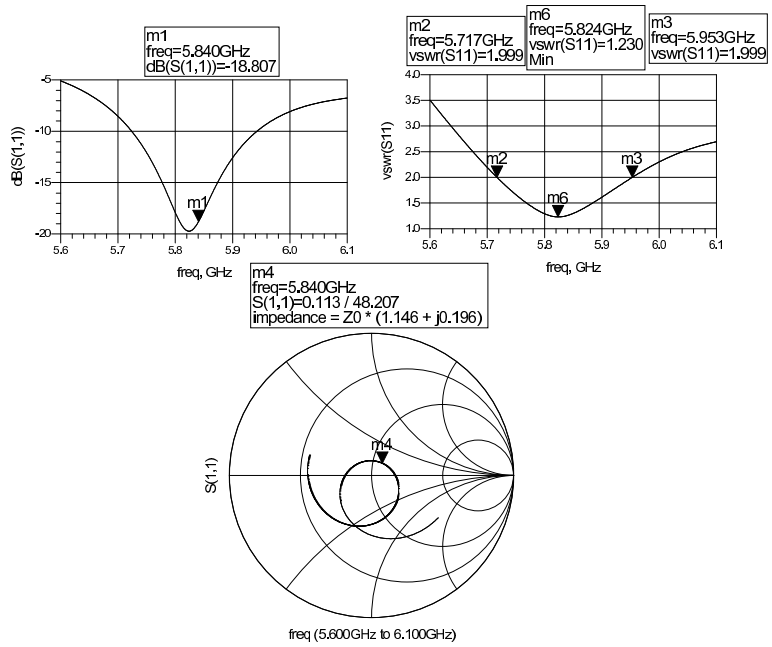

Figure 7.10: Simulation results from ADS with the MSA from Tab. 5.4, all the phase shifters are in the delay state.

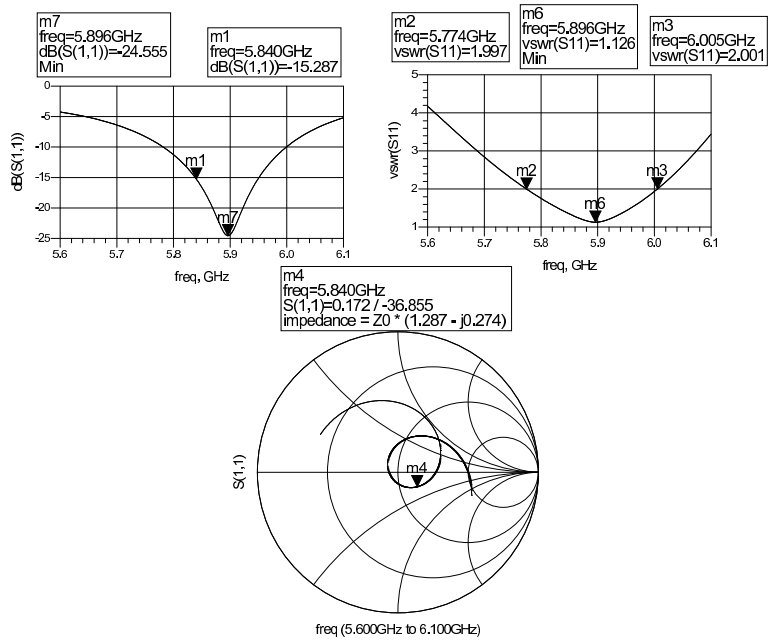

Figure 7.11: MSA with 13.6 mm length and all the phase shifters in the reference state, this means that the boresight beam is activated.

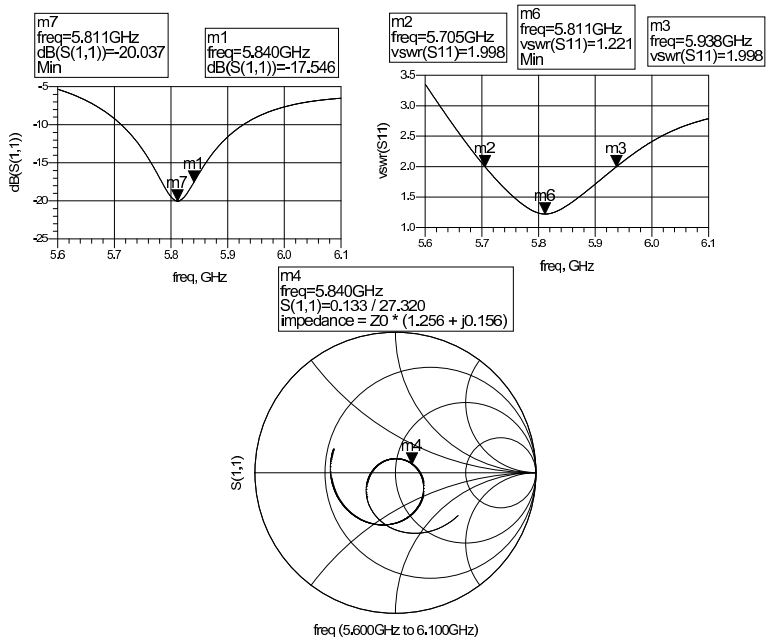

Figure 7.12: MSA with 13.6 mm length and all the phase shifters in the delay state, this means that the boresight beam is activated.

reference line or along the delay line will be decided by which state has the lowest loss. As can be read from Tab. 7.2 the path along the reference line has the lowest loss, but the difference is very small. Since there is less loss along the reference line state and to have the array working in a logical way, the reference line will be used for the boresight beam and act as the reference state.

When the array is steering the beam out to any of the directions it will have delay on either two elements on the same main branch or each main branch will have one element with delay (see Tab. 6.5).

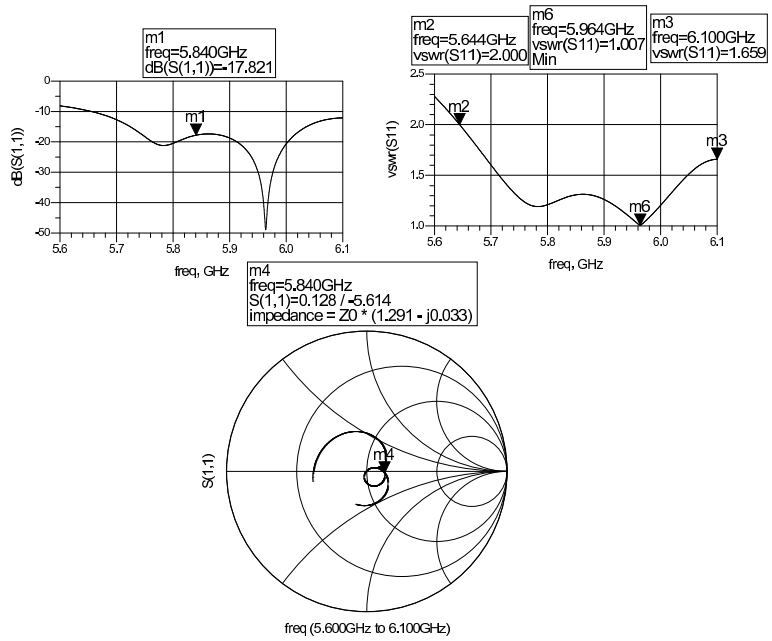

Figure 7.13: Simulation results from ADS with the 13.6 mm MSA. One main branch is in the delay state while the other is in the reference state, equivalent to steering the beam forwards or backwards.

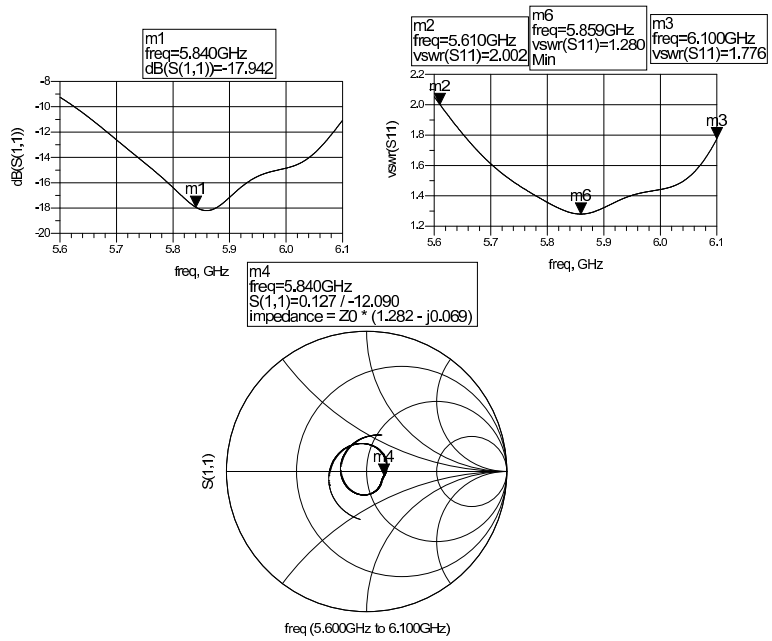

Figure 7.14: Simulation results from ADS with the 13.6 mm MSA. Each main branch has one phase shifter in each state, this is equivalent to steering the beam to left or right.

Chapter 8

From Simulation Circuits to Physical Circuits

When the circuits were sent out to for price offers a week went by, but no price offers came. It seems that the RT/duroid substrate was not readily available among PCB manufactures. Or it could be that the two substrates had such a large differences in their physical properties that it would be very difficult to make the PCB.

In an effort to try to speed things up it was decided to do a redesign of the MSA elements using the same substrate as used for the feed network. The RO4003C substrate is more commonly used and compared to the RT/duriod substrate there is one less step in the production. Using the same substrates for the feed network and the MSA elements also has mechanical benefits. Both the RT/duriod 6002 and RO4003C substrate is recommended for multilayer space applications by Rogers, App. B.4.

Since the feed layer remains the same this modification will have not have any affect on the feed network.

The MSA has been redesigned to give a good trade off between an array with all phase shifters in the reference state and with all of them in the delay state. The design procedure has been the same as described in chapter 5. The MSA dimension and placement is given in Tab. 8.1 while the simulation results for the steering the beams in different directions are given in App. G.8

The RO4003C substrate has a higher dielectric constant, ε_r than the RT/duroid 6002 substrate which results in shorter antenna. The increased ε_r leads to a shorter wavelength in the substrate, in this case a reduction of about 2 mm. This agrees well with the decrease in resonant length of the antenna of 0.9 mm since the resonant length is approximately half a

Parameter	*Value*	*Units*
Width	10	mm
Length	12.7	mm
f_0	5.83	GHz
BW	2.7	%
Efficiency	93	%
Directivity	6.6	dBi
Probe-to-edge	4.56	mm

Table 8.1: Results for EMDS simulation for the MSA with RO4003C substrate.

wavelength. The increase in ε_r will also reduce the fringing fields since more of the electric field is now contained inside the substrate. As a consequence of this the MSA radiation efficiency decreases. Equation (2.14) also states that the directivity will decrease with an increased ε_r. PCAAD suggests that the element directivity decreases from 6.3 dBi to 6.2 dBi and the array directivity drops 0.1 dB to 13.3 dBi. EMDS simulations also shows the same reduction

Changing substrates did speed up the process (a price offer came after just two days) so the final stack-up ended up to be as shown in Fig. 8.1. RO 4450 (see App. B.3) acts as the adhesive layer.

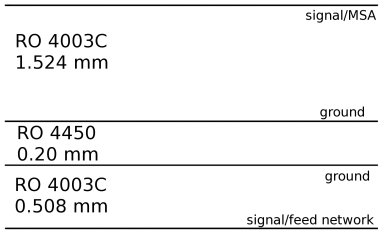

Figure 8.1: A cross section of the final stack up that will be sent to production.

8.1 Layout

To validate the accuracy of the simulations it is necessary to physically realize the circuits and do measurements on them. When connecting these circuits to a VNA through a coaxial cable, some kind of transition between the coaxial cable and microstrip is needed. The transition is is taken care of by a SMA adapter that is attached to the circuit board through another

"homemade" adapter like in Fig. 8.2. This is all mounted on a metal surface that has vias connected to both ground planes.

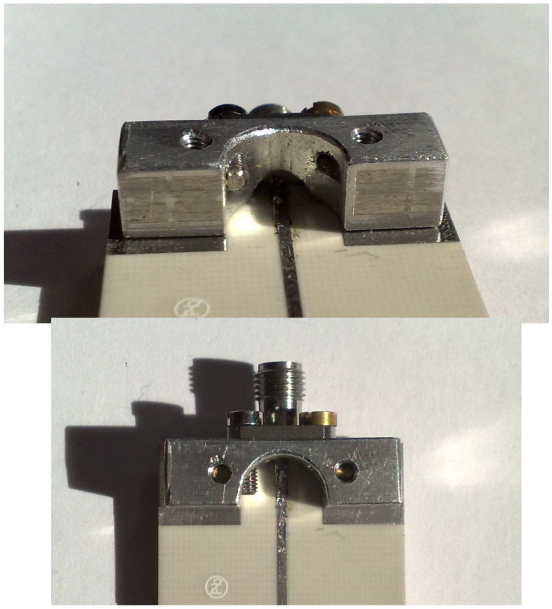

Figure 8.2: Shows the adapter for the SMA connection.

8.1.1 Calibration Kit

When performing measurements with a network analyzer it is important to do a calibration first. The calibration removes systematic errors in the analyzer and test setup. If the calibration is done with a standard calibration kit the reference plane will be at the end of connector that the calibration kit has been connected to, see Fig. 8.3. The problem with this method is that the connector on the DUT (usually a SMA-adapter) now becomes a part of the DUT. The reference plane will be at the end of the cables that connects the DUT to the network analyzer like in Fig. 8.3. So that any mismatches in the transition from e.g. coaxial center conductor to a microstrip will affect the results. To avoid this problem a calibration kit has been made for the test circuits that will be measured on here.

A standard 2-port calibration procedure consist of SOLT calibration. These components are hard, if not impossible, to fabricate in microstrip technology with such high quality as in a regular calibration kits. The solution is then to do a TRL calibration as suggested in [25]. A TRL calibration removes the effects from the launcher (transition from coaxial center conductor to the

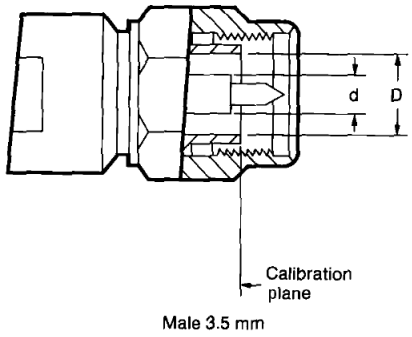

Figure 8.3: Cross section of a male SMA connector showing where the calibration plane will be after a SOLT calibration. Source [10].

microstrip) and moves the calibration plane. The difference in measurements with a SOLT calibration and TRL calibration is illustrated in Fig. 8.4.

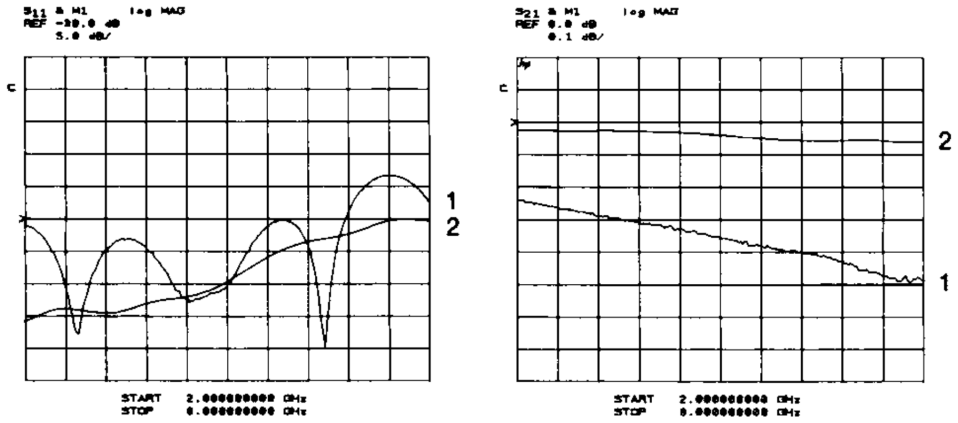

Figure 8.4: Example of measurements performed with calibration ports at the coaxial ports (1) and with a TRL calibration (2). S_{11} plot to the right and a S_{21} to the left.

Thru

A nonzero length Thru calibration component will be made. The microstrip line will have a total length of 35 mm and a width of 1.14 mm, no delay will be used in the calibration. This will cause the reference plane to be at the center of the Thru line, i.e. 17.5 mm from the end/start of the line. This component decides where the the reference plane will be.

Reflection

The reflection component will be made as an open circuit at the reference planes. Some distance is required between the open ends to limit crosstalk. Data gathered from this calibration component contributes to the error model that accounts for the systematic errors.

Line

This component has a quarter wave long microstrip line inserted between the reference planes. The extra piece of line must have the same impedance as the microstrip lines from the Thru component since this component decides the system impedance.

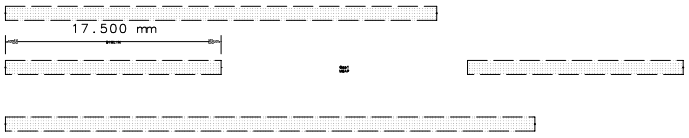

Figure 8.5: Layout of microstrip lines. From top to bottom: Thru, Reflection and Line.

Since the calibration kit moves the reference plane 17.5 mm into the microstrip lines, all DUT will have a feed line 1.14 mm wide and 20 mm long to make sure the reference plane is not inside the DUT.

The final layouts for the calibration kit is given in App. G.1

8.1.2 Test Circuits

Tee-junction

To test the tee-junctions in the feed network, a test circuit that splits and then combines the signal again has been made. The parameter of interest her is the loss, S_{21}. The layout with simulations results is given in App. G.2.

Quarter Wave Transformer

This test circuit consists of two quarter wave transformers from the feed network. The first one transforms from a 50 Ω line to a 100 Ω line while the second transformer does the opposite. Parameters of interest here are

the reflection coefficient, S_{11}, and the loss, S_{21}. The layout with simulations results is given in App. G.3.

DC Network

This circuit consist of the DC network and quarter wave transformers. The transformers are needed since the DC circuit is based on 100 Ω microstrip lines. The important parameter here is the loss, S_{21}. The loss from the quarter wave transformers is already known from the quarter wave transformer circuit so it can be subtracted to find the loss through the DC network. The layout with simulations results is given in App. G.4.

Phase Shifter

As a natural step further the line switcher is added to the quarter wave transformers and the DC network. Loss and phase delay are the most interesting parameters. The layout with simulations results is given in App. G.5.

Single MSA Element

3 different patch sizes has been manufactured. All with the same probe-to-edge distance of 4.56 mm. The objective here is to evaluate the accuracy of the EMDS simulations. The layout with simulations results is given in App. G.6.

Array without Phase Shifter

Measurements from this array configuration can be used to compare the array with and without phase shifters. The radiation diagram from this array can also be compared with computer simulations. The layout with simulations results is given in App. G.7. The small circles that are placed in the layout are vias that connects the two ground planes. The vias goes through the entire stack-up instead of being buried since buried vias were only available for certain stack-ups.

Array with Phase Shifter

All the above sub circuits put together as a system. There has also been added some lines and room for switches so that the phase shifters can be

controlled. The radiation diagrams for the different beams and corresponding S_{11} parameters should be measured. The layout with simulations results is given in App. G.8.

Chapter 9

Measurments

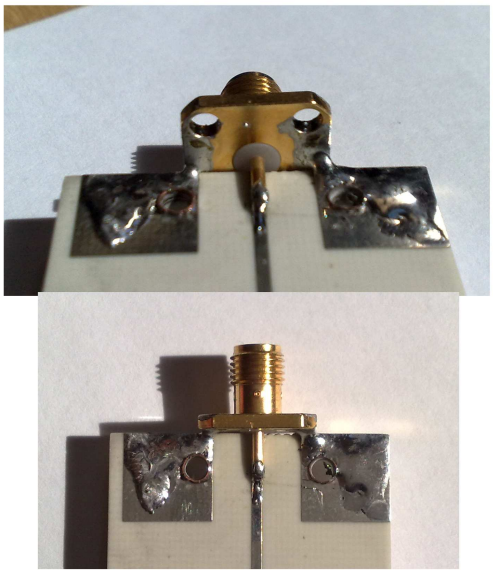

Figure 9.1: SMA-to-microstrip transition.

When the measurements was first started poor and very variable results were obtained. As it turns out, the aluminum adapter used to fasten the SMA connector has a very poor electrical connection to the ground plane. Aluminum is relatively easy to machine and is a fairly decent electrical conductor, but when aluminum is exposed to oxygen a thin layer of Al_2O_3 is formed on the outer surface. This layer is an electrical insulator (alumina substrate is made from Al_2O_3) and could be blamed for causing the poor electrical connection. Therefore, the SMA adapters was soldered directly onto the circuit boards. This solution lacks mechanical strength, so some

care should be taken while fastening cables to the circuit board.

Equipment used:

1. VNA used for S-parameter measurements
   - Make: Hewlett Packard
   - Model: HP8510C (45 MHz - 26.5 GHz)
   - Serial #:HJ401401
2. VNA used for radiation diagrams (measuring S_{21})
   - Make: Agilent Technologies
   - Model:E8364B (10 MHz - 50 GHz)
   - Serial #: HJ4024
3. Motion controller used for rotating the antenna during measurements
   - Make: Newport
   - Model: MM4005
   - Serial #: TD4004

9.1 S-parameter Measurements

After analyzing the measurement results it was discovered that the wrong ε_r had been used. When using the RO4003C substrate in circuit design a ε_r of 3.55 should be used instead of 3.38. The simulated results used in the following comparisons has been simulated with $\varepsilon_r = 3.55$

9.1.1 TRL Measurements

As can be seen from Fig. 9.2 and 9.3 the TRL calibration does not provide good reliable results. Therefore, the results from this calibration procedure has been ignored.

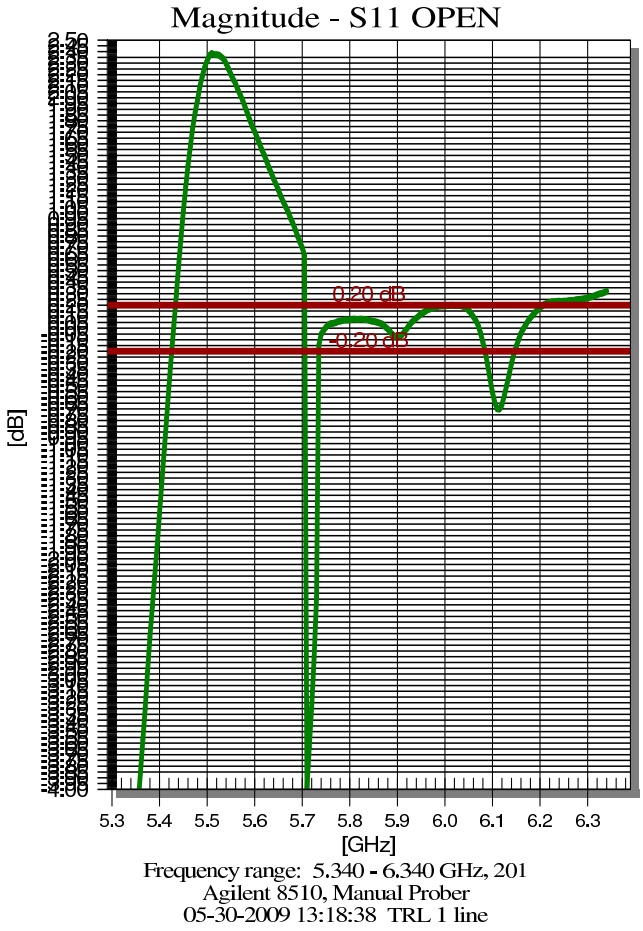

Figure 9.2: Calibration verification. Automatically generated in WinCal (software for remote operation of network analyzer). Y-axis ranges from 2.5 - -4 dB.

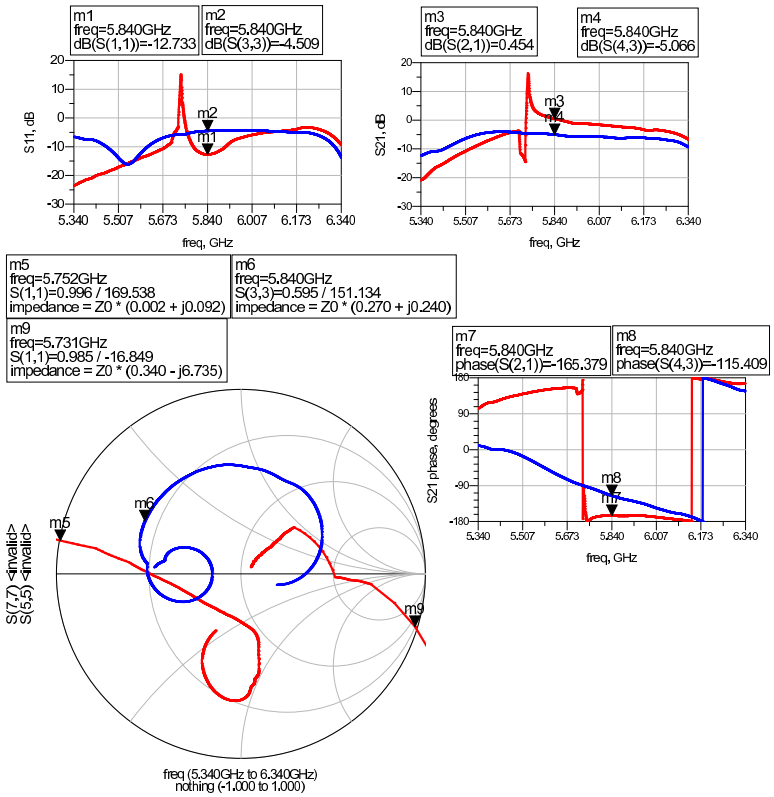

Figure 9.3: Results obtained after measuring on the quarter wave transformer test circuit in App. G.3. Red = measured with TRL calibration and blue = measured with SOLT calibration.

9.1.2 SOLT Measurements

After the SOLT calibration has been completed the network analyzer will be matched to 50 Ω and the reference plane will be at the tip of the cables connecting to the DUT, see Fig. 8.3.

Since the TRL calibration did not work out it was tried to use gating to avoid/disregard the mismatch reflections caused by the SMA-to-microstrip transition. By sending a pulse into the DUT and observe the reflected signal in the time domain one can tell where the reflection originates from. Once it is known where the "problem" is, one can use gating to ignore the reflection that occurs at the specific time interval where the reflection is positioned (position = speed of light times delay). To get an accurate position of the reflections in the time domain, the pulse needs to be wide in the frequency domain. As it turns out the VNA could not provide a pulse with a large enough bandwidth to get a time domain assessment that was accurate enough to map the reflections. The observable result was a reflection that extended beyond the DUT in both directions.

TRL Calibration Kit

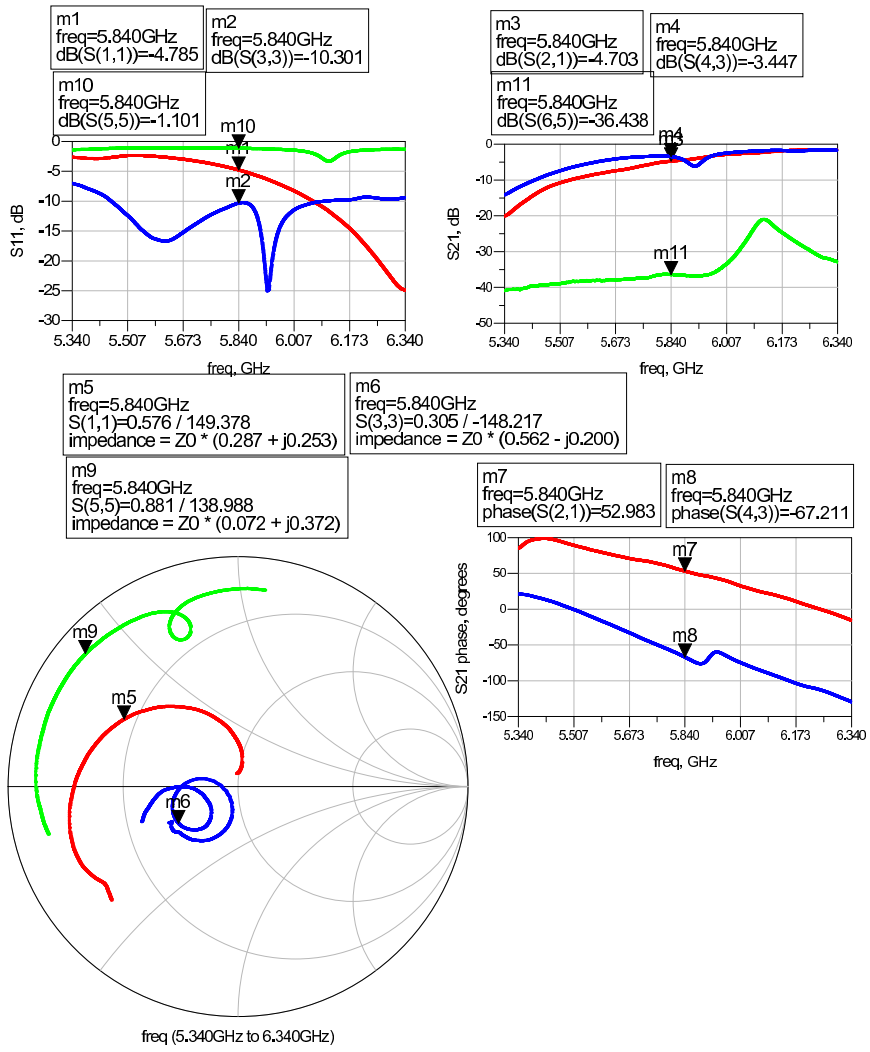

Figure 9.4: Results obtained after measuring on the TRL kit given in App. G.1. Red = Thru, blue = Line and green = Reflection.

Tee-junction

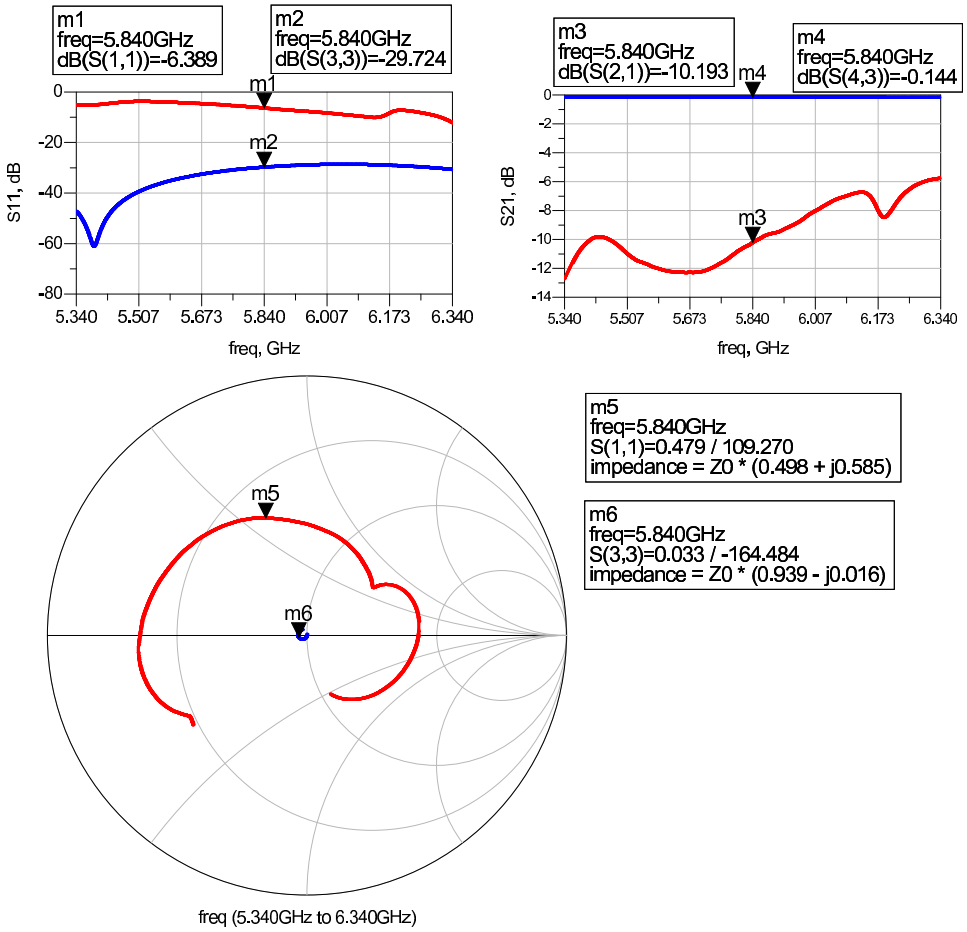

Figure 9.5: Results obtained after measuring on the tee-junction test circuit in App. G.2. Red = measured and blue = simulated.

Quarter Wave Transformer

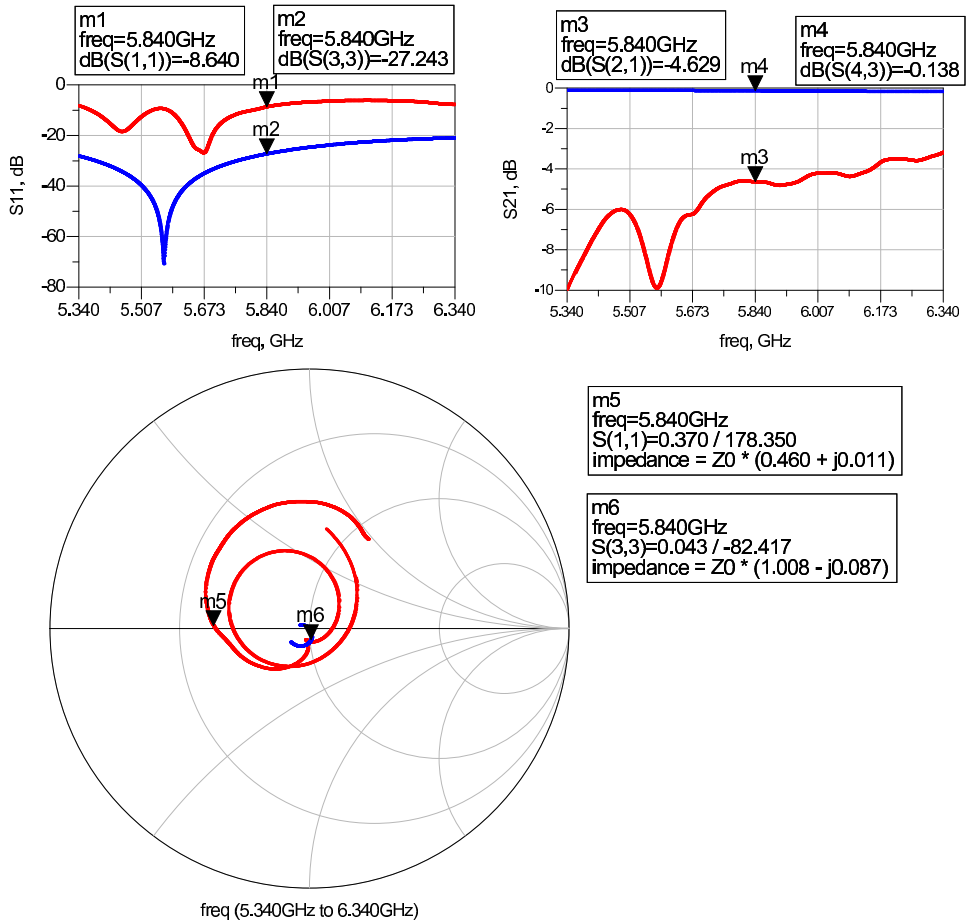

Figure 9.6: Results obtained after measuring on the quarter wave transformer test circuit in App. G.3. Red = measured and blue = simulated.

DC Network

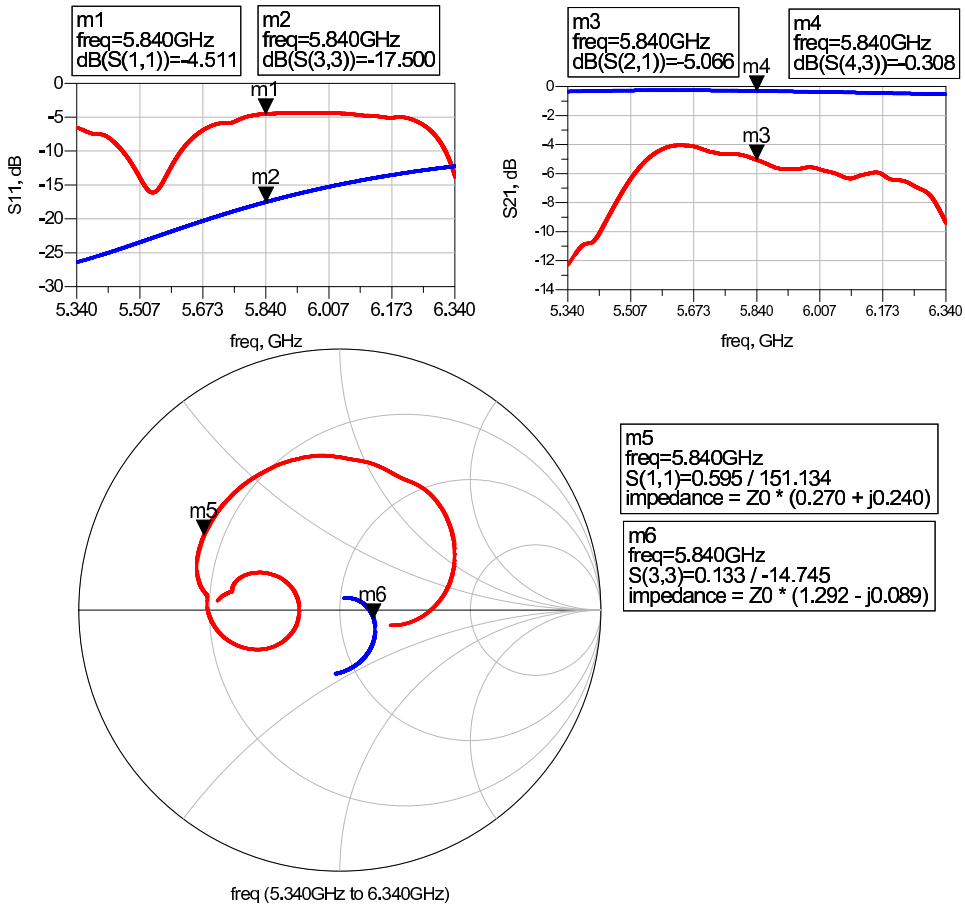

Figure 9.7: Results obtained after measuring on the DC network test circuit in App. G.4. Red = measured and blue = simulated.

Phase Shifter

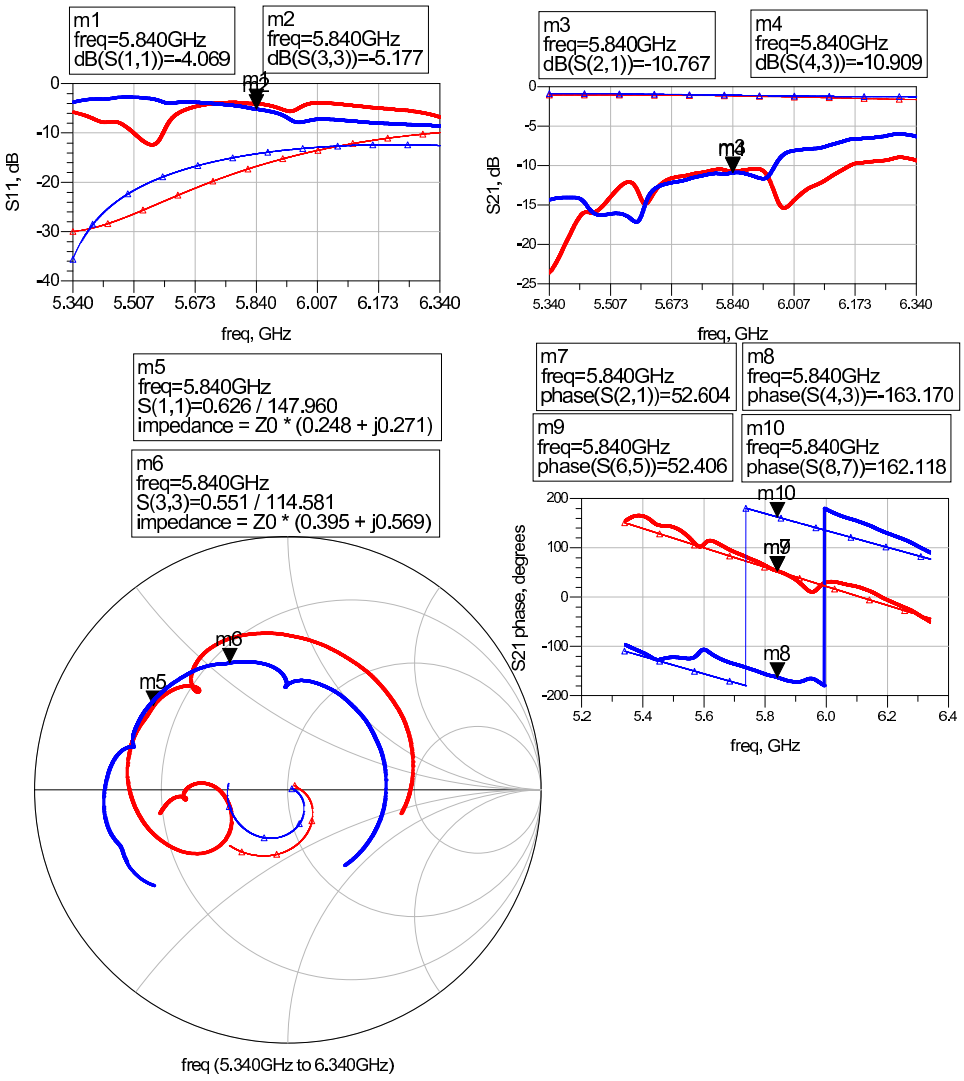

Figure 9.8: Results obtained after measuring on the phase shifter test circuit in App. G.5. Red = phase delay, blue = reference phase and the dotted lines are corresponding simulated results.

Single SMA Elements

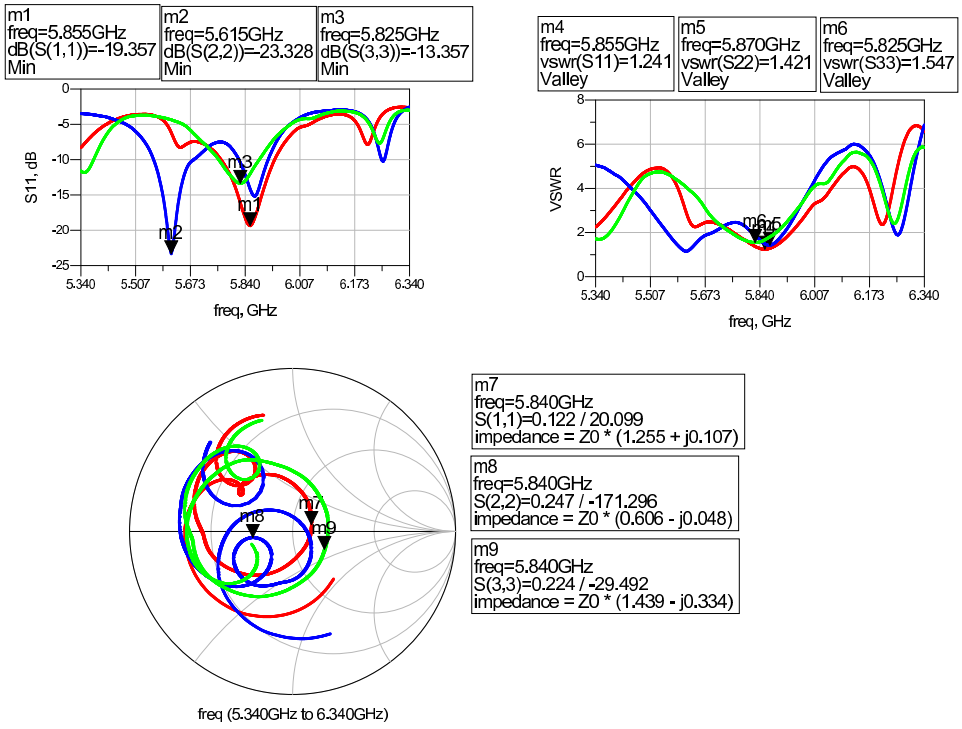

Figure 9.9: Results obtained after measuring on the single MSA elements from App. G.6. Different colors for various patch lengths. Red = 12.6 mm, blue = 12.7 and green = 12.8 mm.

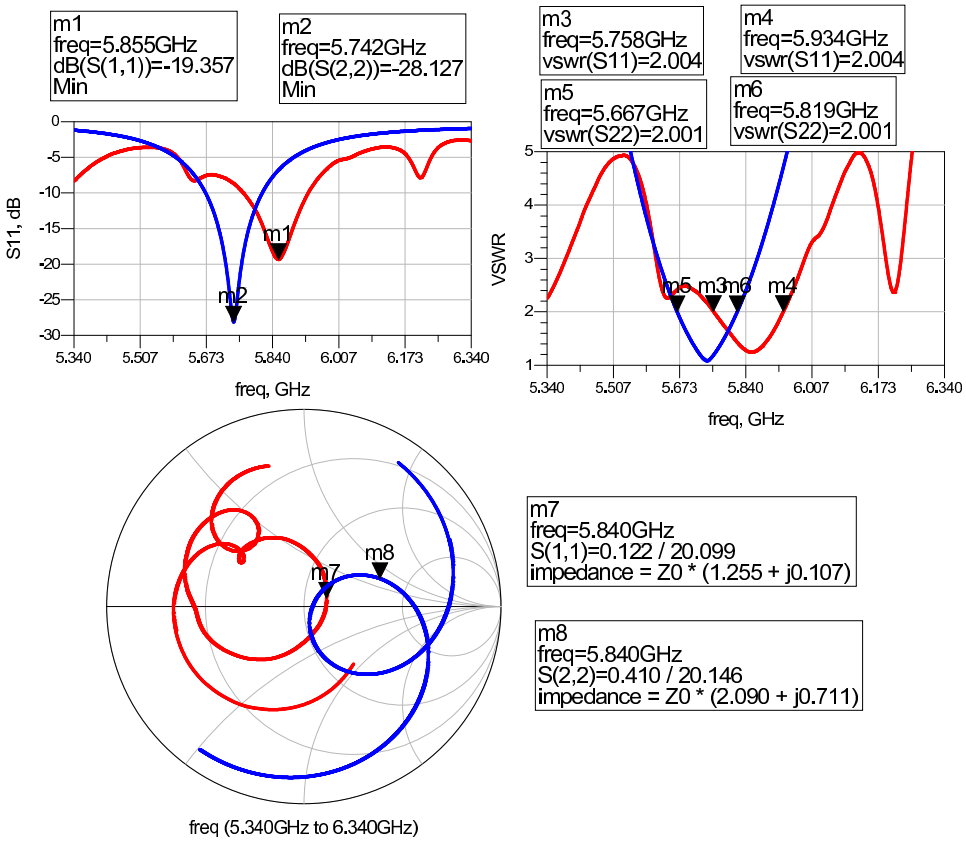

Figure 9.10: Results from measuring on the 12.6 mm long patch. Red = measured and blue = simulated.

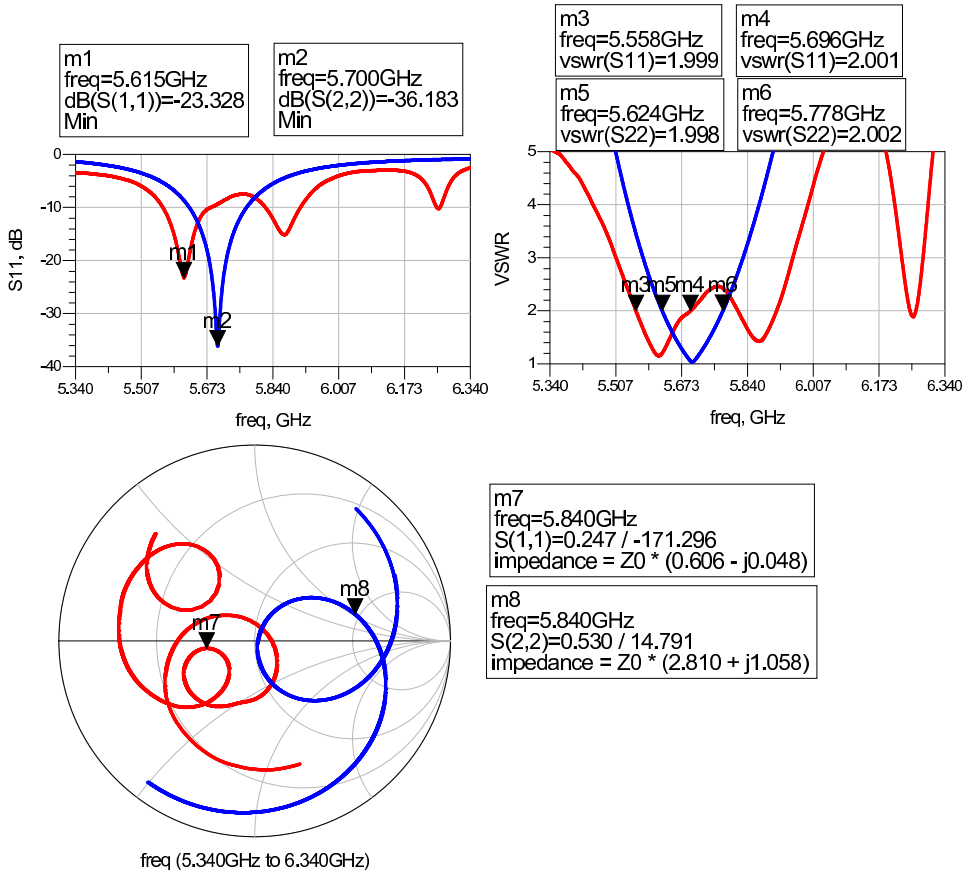

Figure 9.11: Results from measuring on the 12.7 mm long patch. Red = measured and blue = simulated.

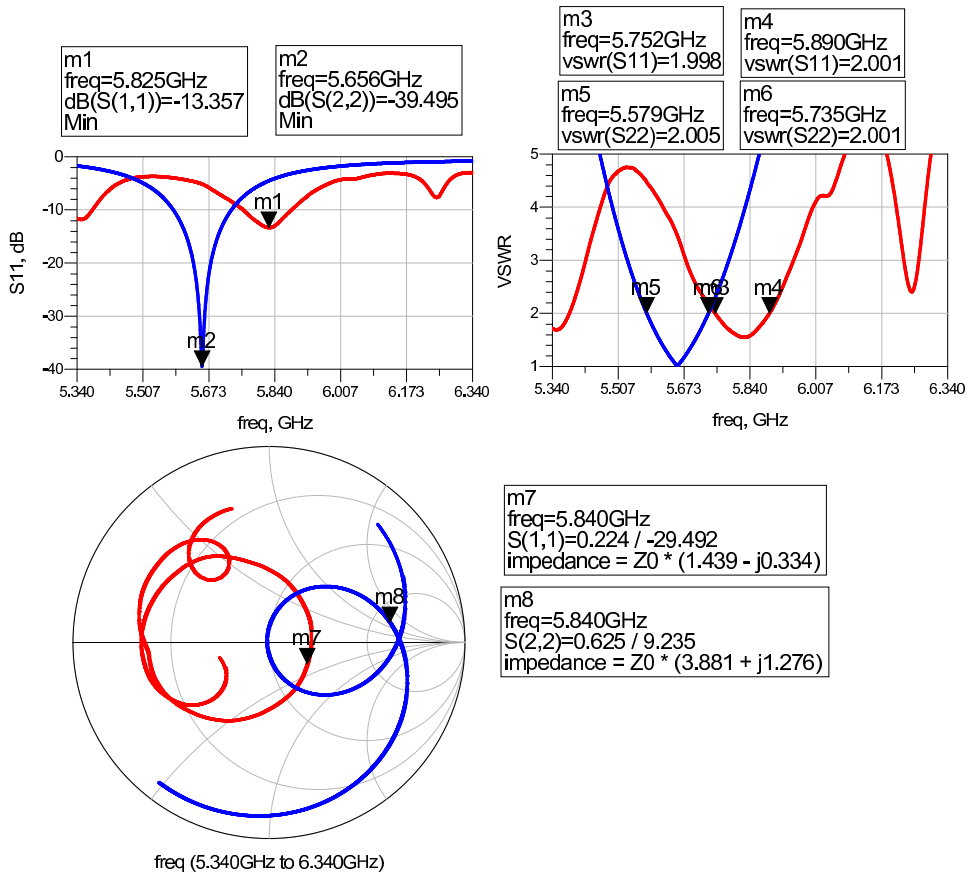

Figure 9.12: Results from measuring on the 12.8 mm long patch. Red = measured and blue = simulated.

Static Array

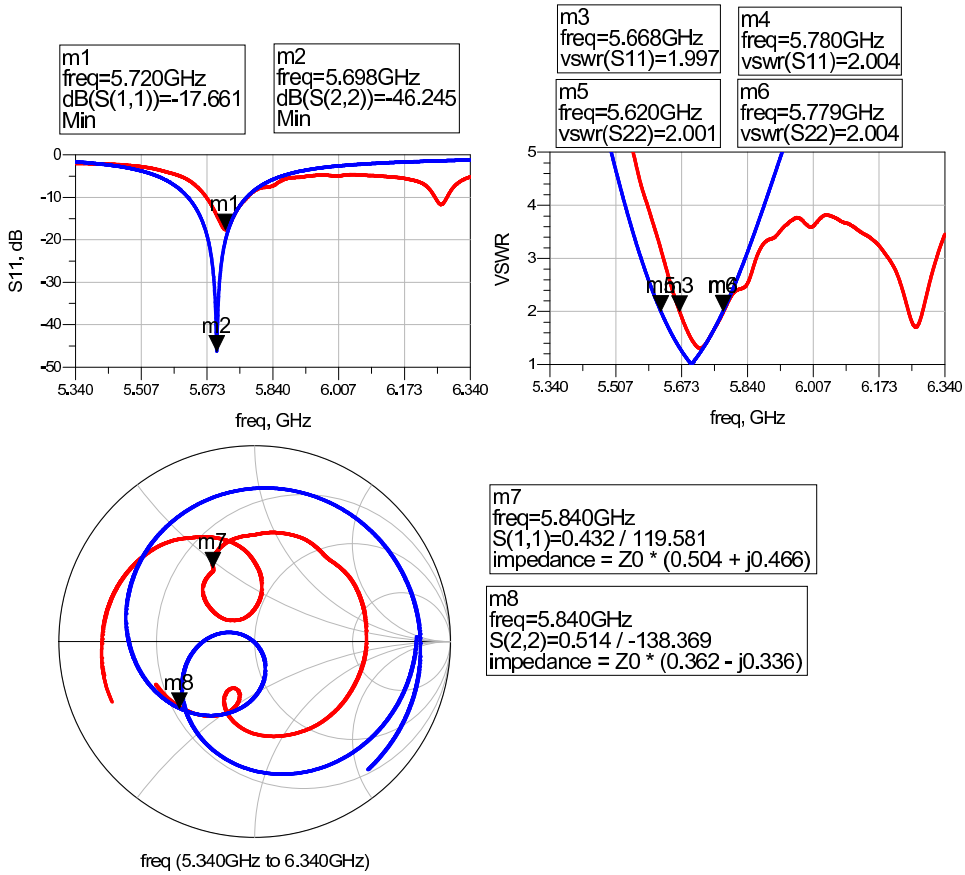

Figure 9.13: Results from measuring on the static array test circuit in App. G.7. Red = measured and blue = simulated.

Switched Beam Array

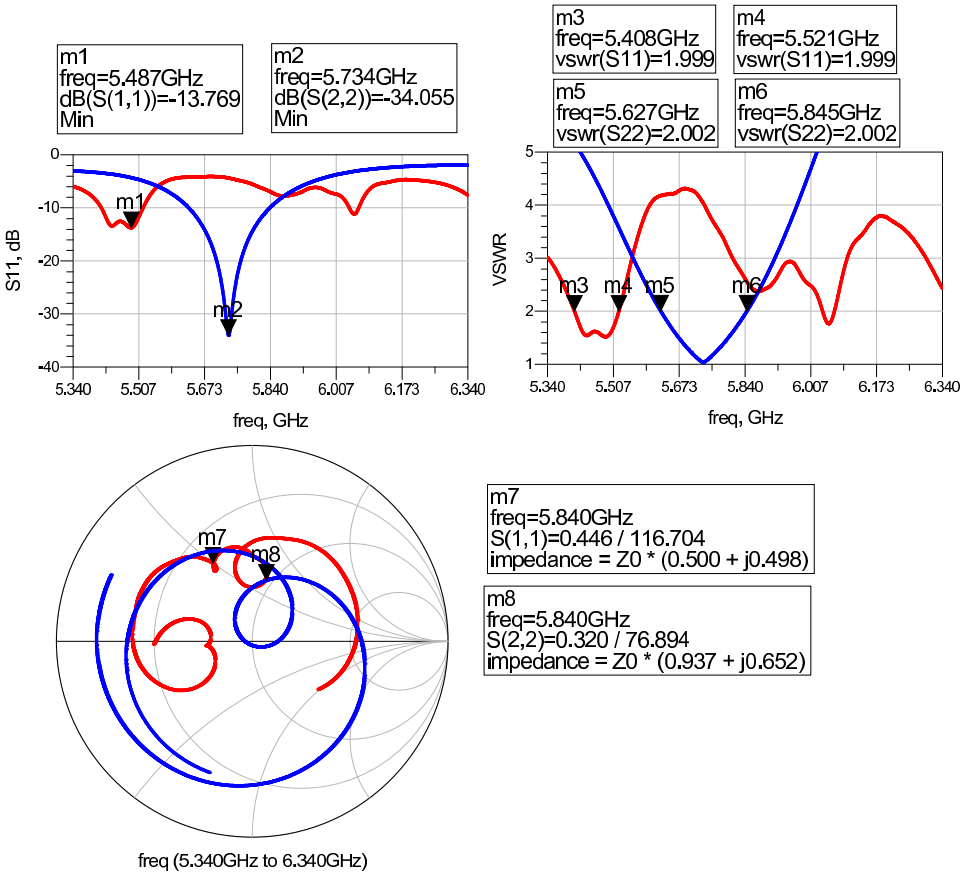

Figure 9.14: Comparison of measurement on the array from App. G.8 with all phase shifters in the reference mode. Red = measured and blue = simulated.

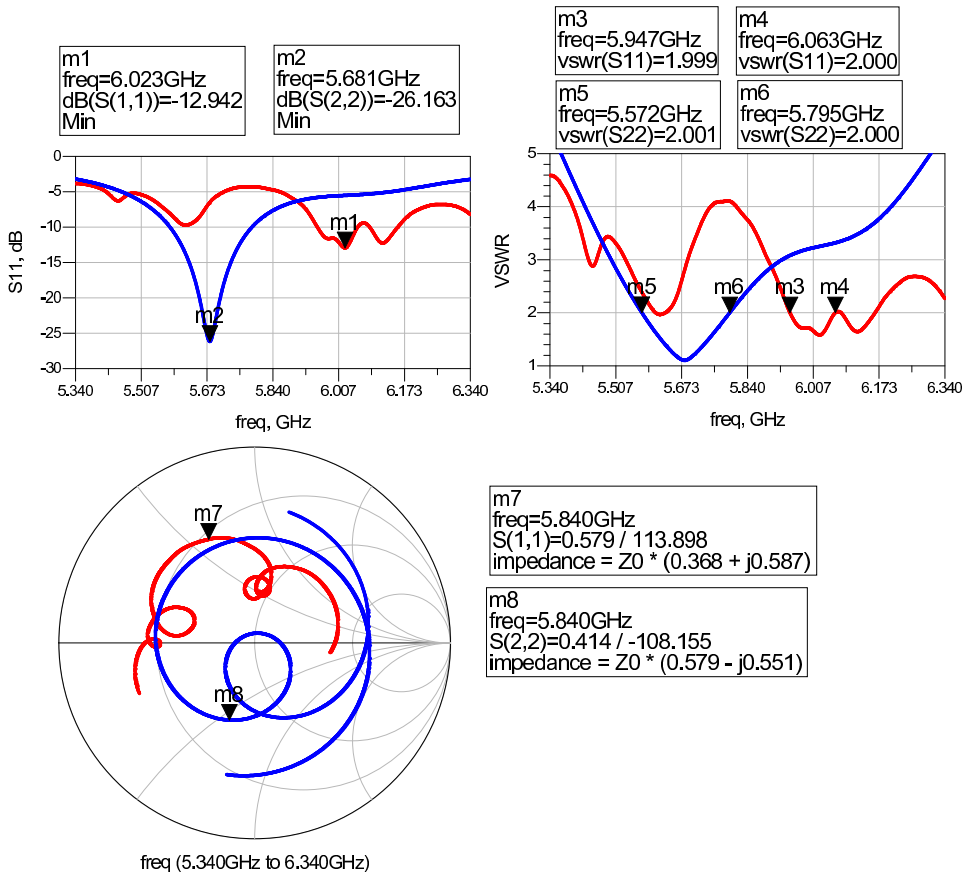

Figure 9.15: Comparison of measurement on the array with all phase shifters in the delay mode. Red = measured and blue = simulated.

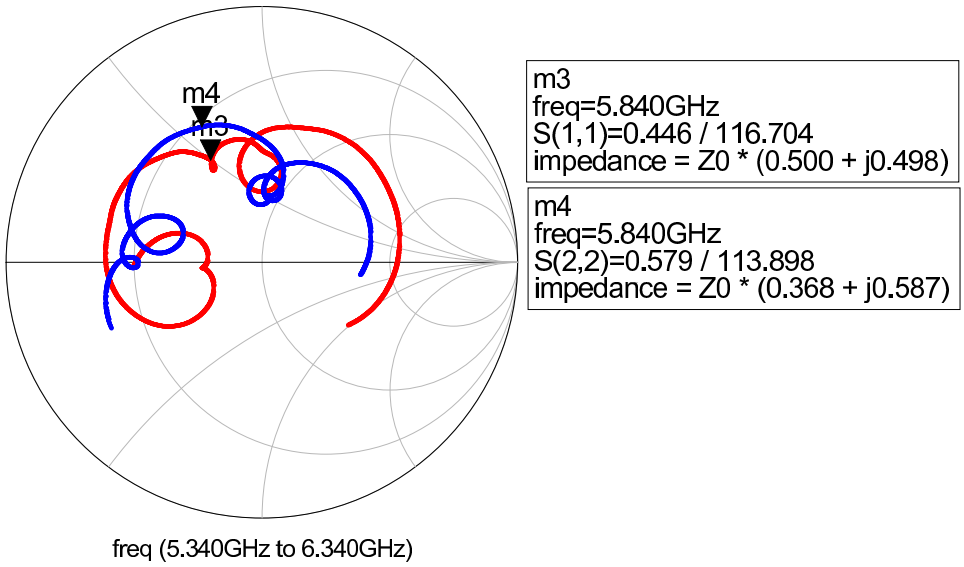

Figure 9.16: Measured results. Red = all phase shifters in the reference mode and blue = all phase shifters in the delay mode.

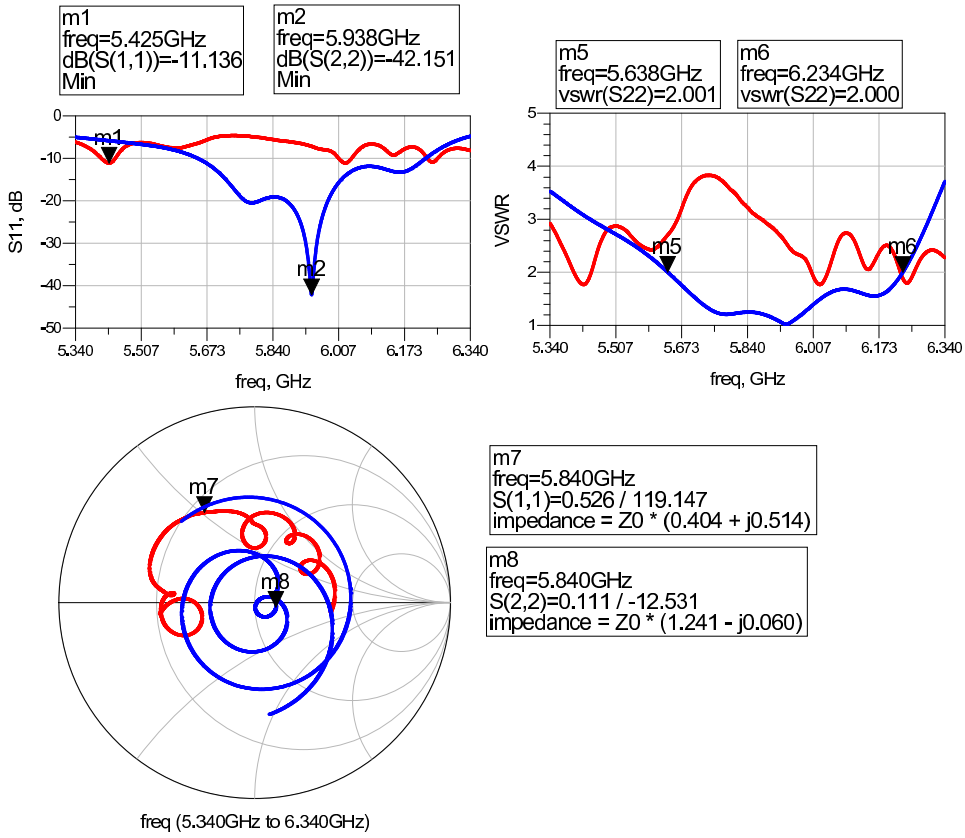

Figure 9.17: Comparison of measurement on the array where one main branch has both phase shifters in the delay mode while the other main breach has them in the reference mode. Red = measured and blue = simulated.

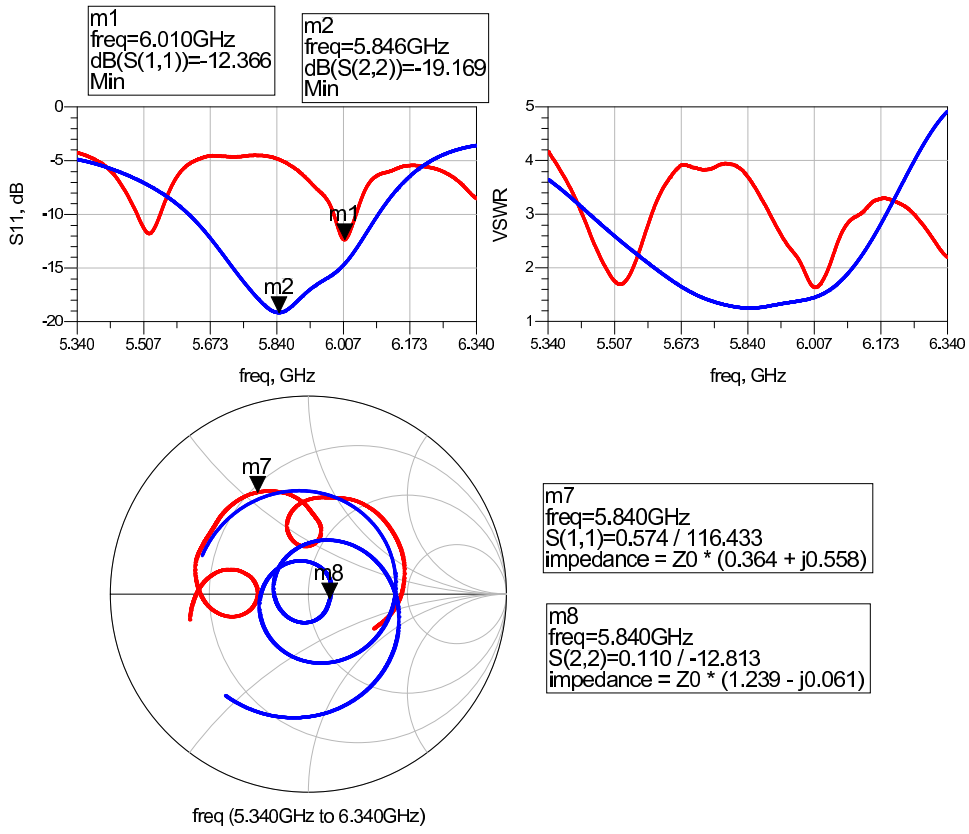

Figure 9.18: Array where each main branch has both phase shifter modes represented. Red = measured and blue = simulated.

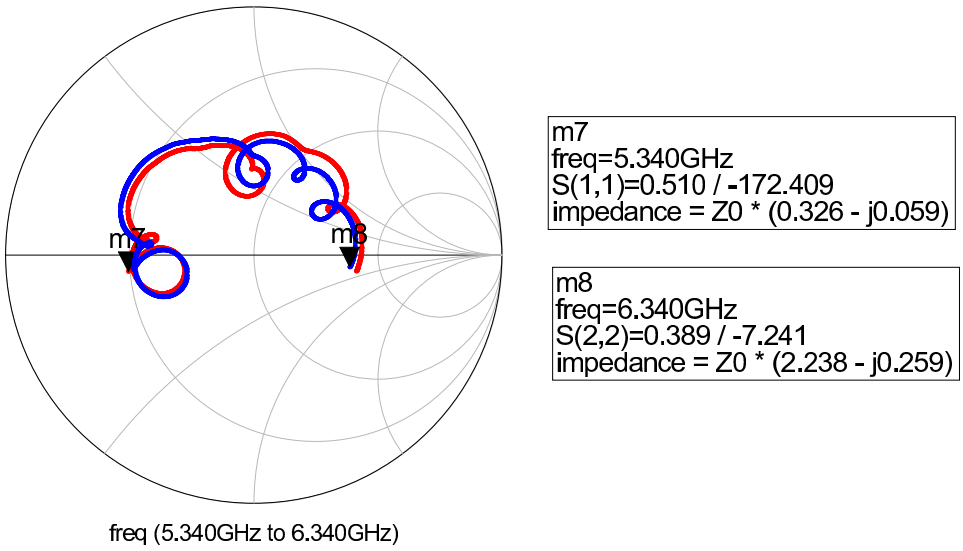

Figure 9.19: Red = array with one main branch with both phase shifters in the reference mode while the other main branch is in the opposite mode. Blue = same as red, but with opposite phase shifter modes.

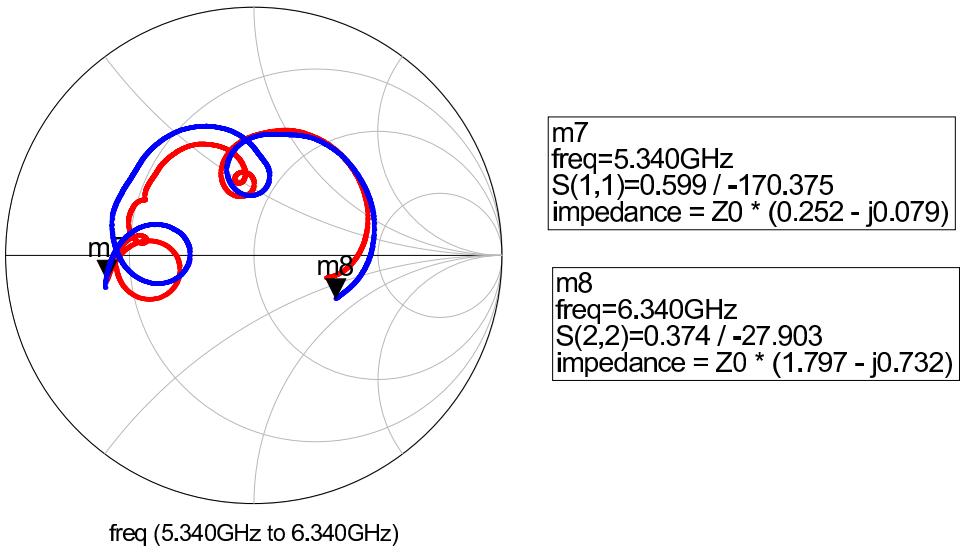

Figure 9.20: Red = array where each main branch has both phase shifter mode represented. Blue = same as red, but with the phase shifter in opposite modes.

9.2 Radiation Diagrams

The radiation diagrams has been measured using a turntable to rotate the antenna which is placed inside an EM anechoic chamber. A horn antenna with distinct polarization (dependent on its orientation) acts as the transmitting antenna and the DUT as the receiving antenna. When measuring on the array configuration only the vertical polarization has been measured. Since the MSA elements are rotated 45 degrees and their polarization is parallel to their length, only half of the vertical polarization (in the ideal case) will be received by the antenna (will also pick up cross polarization). Therefore, 3 dB has been added to the measured radiation diagrams from the array.

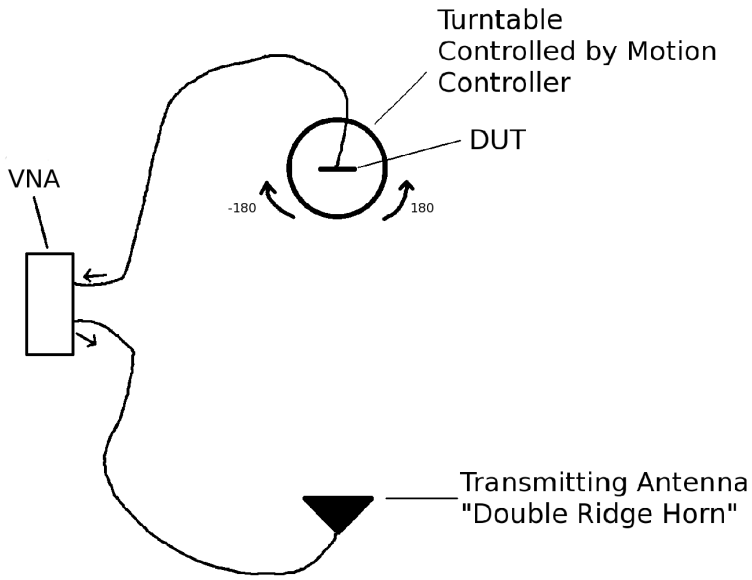

Figure 9.21: Measurement setup for radiation measurements. The DUT is situated inside an EM anechoic chamber while the transmitting antenna is situated at a hole it the wall.

9.2.1 Single MSA Element (12.7 mm)

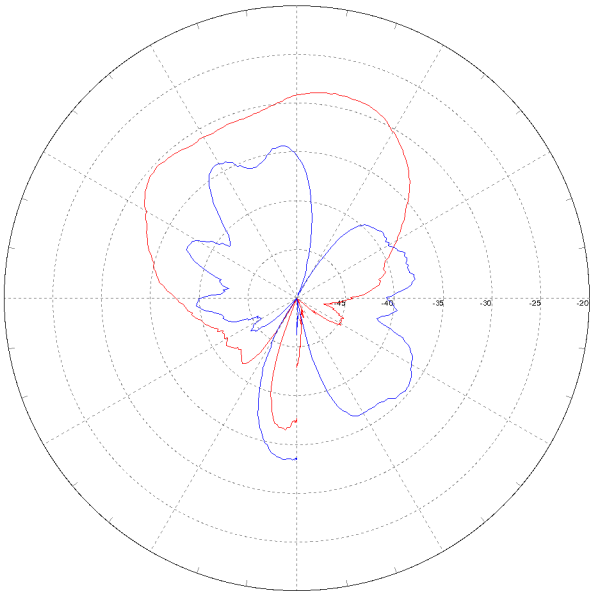

Figure 9.22: E-plane measurements of a single MSA element. E-plane is equivalent to a centered ϕ-cut along the length of the patch. Red = co-polar (max = -28.7 dB) and blue = cross-polar (max = -33.4 dB).

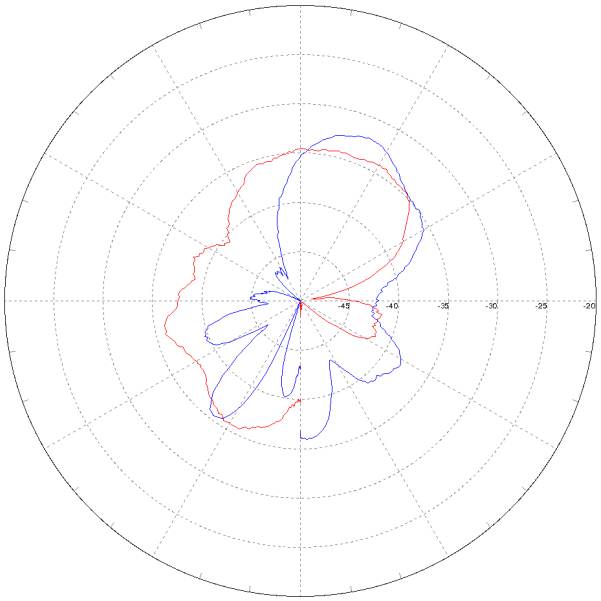

Figure 9.23: H-plane measurements of a single MSA element. H-plane is equivalent to a centered ϕ-cut along the width of the patch. Red = co-polar (max = -29.4 dB) and blue = cross-polar (max = -32.1 dB).

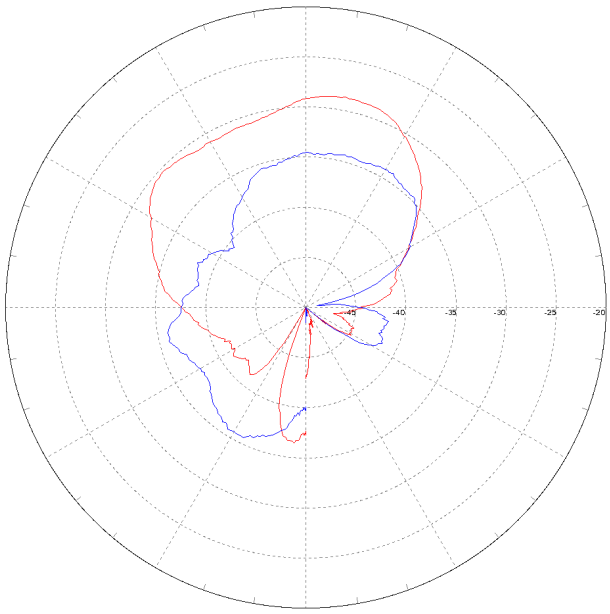

Figure 9.24: Comparison of the E- and H-plane measurements. Red = E-plane and blue = H-plane.

Measurements with the SMA-to-microstrip transition covered with absorbers

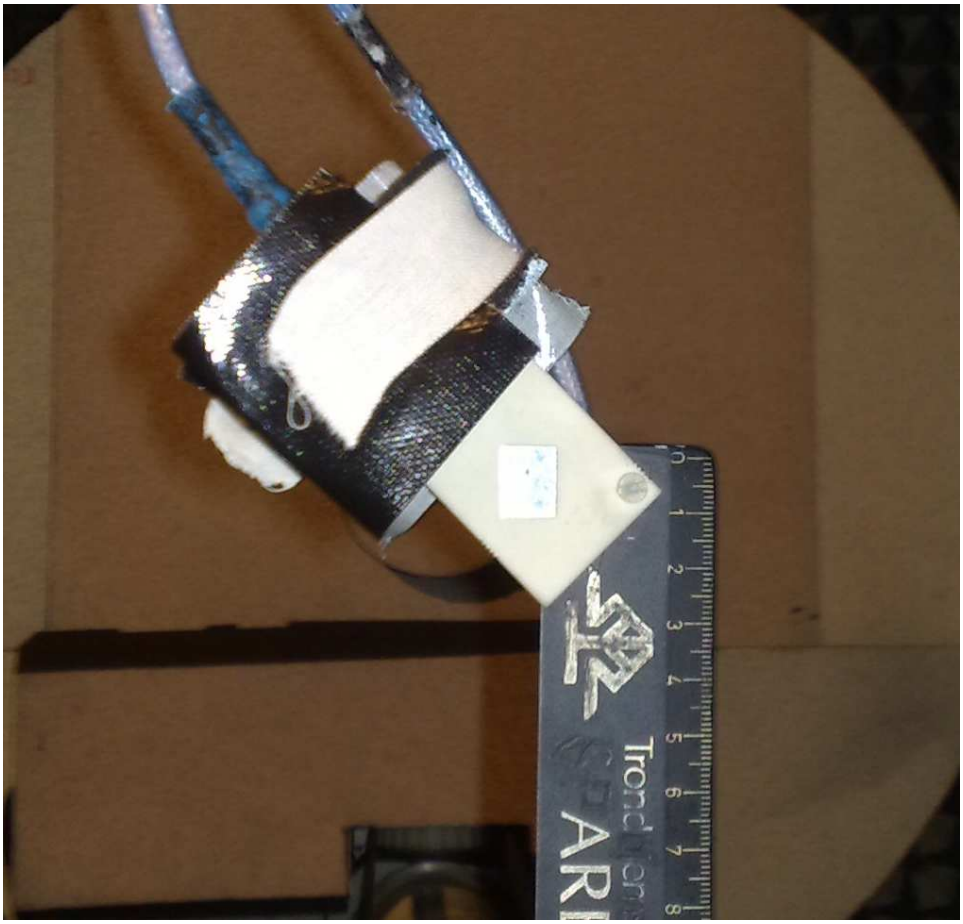

Figure 9.25: Picture of the measurements setup for H-plane measurements. The SMA-to-microstrip launch is covered with absorbers.

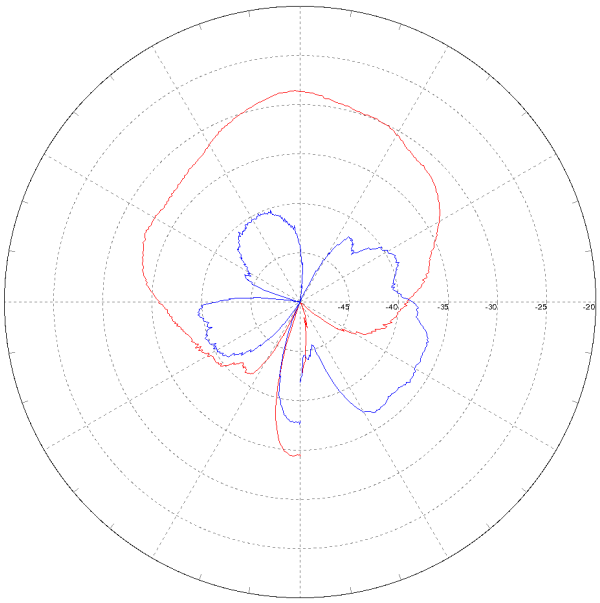

Figure 9.26: E-plane measurements of a single MSA element. E-plane is equivalent to a centered ϕ-cut along the length of the patch. Red = co-polar (max = -28.6 dB) and blue = cross-polar (max = -36.2 dB).

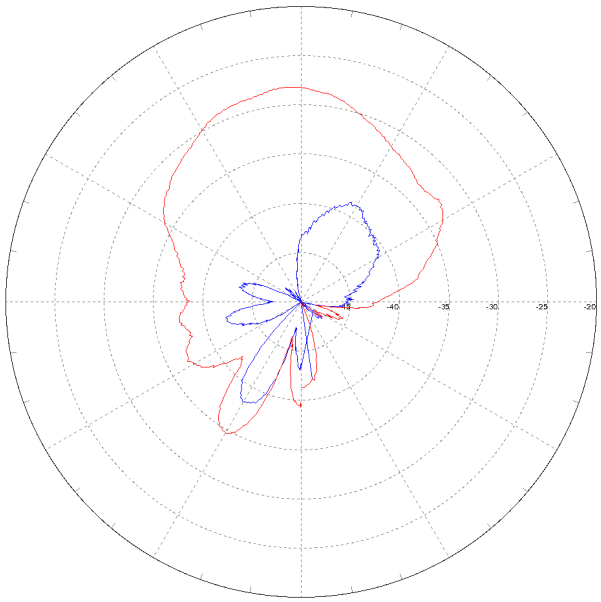

Figure 9.27: H-plane measurements of a single MSA element. H-plane is equivalent to a centered ϕ-cut along the width of the patch. Red = co-polar (max = -28.1 dB) and blue = cross-polar (max = -38.2 dB).

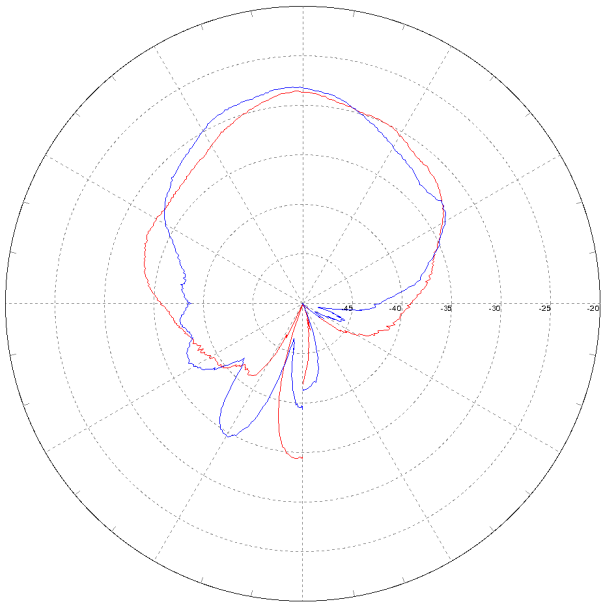

Figure 9.28: Comparison of the E- and H-plane measurements. Red = E-plane and blue = H-plane.

9.2.2 Static Array

It was also tried to measure on the arrays with an absorber covering the SMA-to-microstrip transition. However, in this case it lead to a degraded performance. The absorber probably came to close to the MSA elements. In the following measurement results the absorber have not been used.

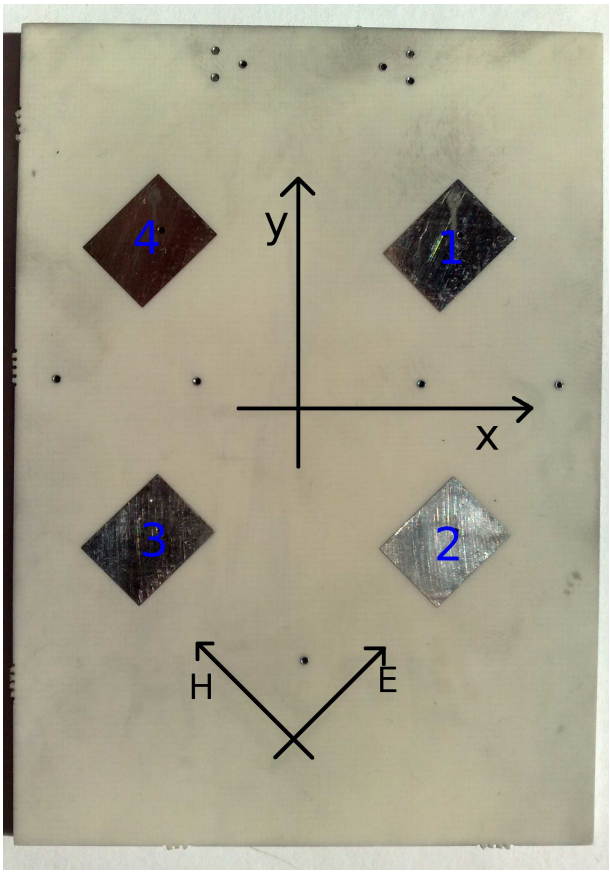

Figure 9.29: Shows the array with element numbers and axes. E and H indicates the E- and H-plane.

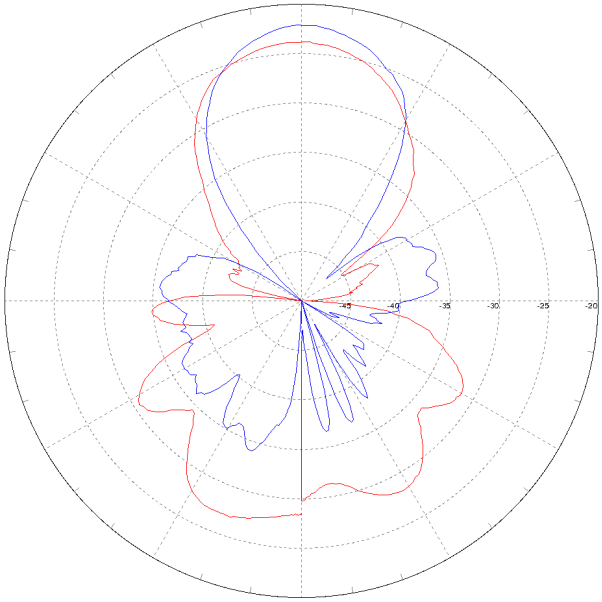

Figure 9.30: Red = ϕ-cut along the x-axis (max = -23.8 dB) in Fig. 9.29 and blue = along the y-axis (max = -23.1 dB).

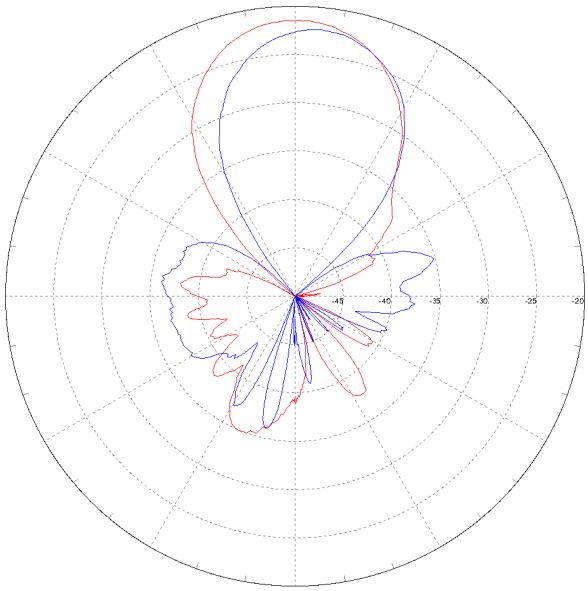

Figure 9.31: Red = ϕ-cut along the x-axis (max = -21.5 dB)in Fig. 9.29 and blue = along the y-axis (max = -22.3). The measurement has been performed with a 10x10 cm absorbers covering the feed network side.

9.2.3 Switched Beam Array

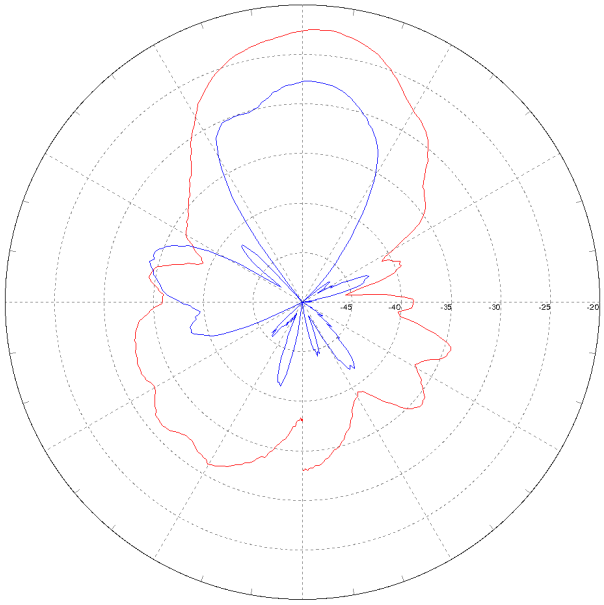

Figure 9.32: Measurement of the boresight beam with all the phase shifters in the reference mode. Red = ϕ-cut along the x-axis (max = -22.4 dB in Fig. 9.29 and blue = along the y-axis (max = -27.7 dB).

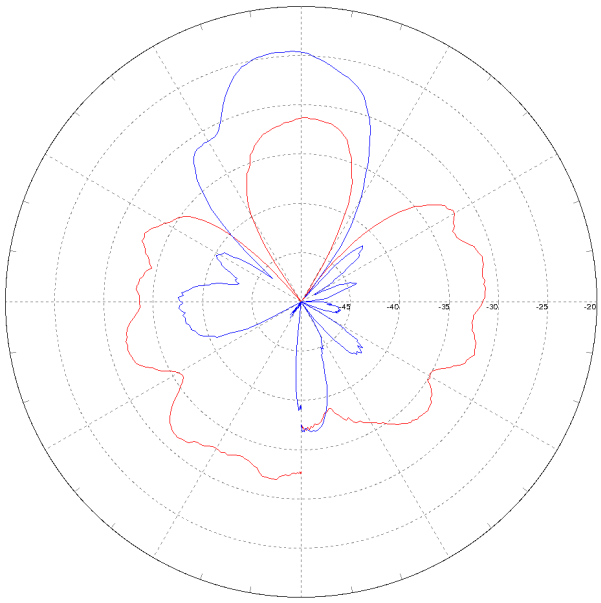

Figure 9.33: Measurement of the boresight beam with all the phase shifters in the delay mode. Red = ϕ-cut along the x-axis (max = -31 dB) in Fig. 9.29 and blue = along the y-axis (max = -24.5 dB).

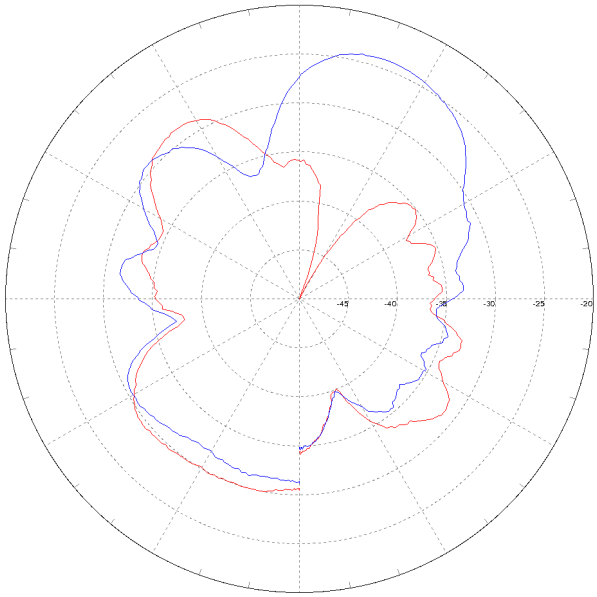

Figure 9.34: Red = ϕ-cut along the x-axis with beam pointing out between element 1 and 2 (max = -28.6 dB) in Fig. 9.29 and blue = beam pointing out between element 3 and 4 (max = -24.1 dB).

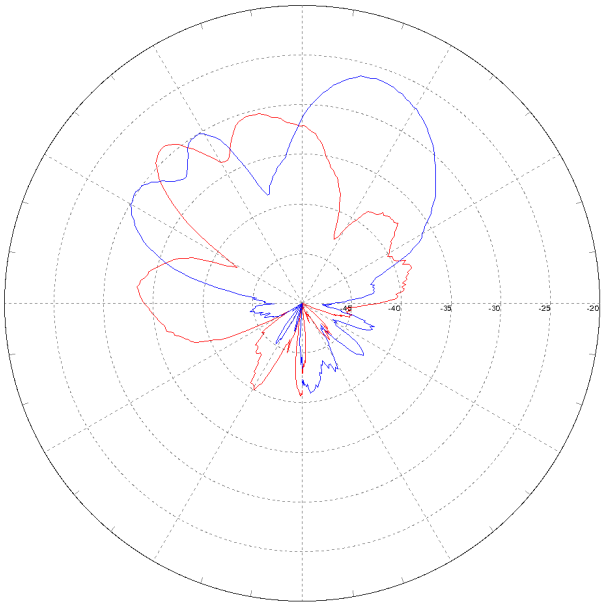

Figure 9.35: Red = ϕ-cut along the y-axis with beam pointing out between element 1 and 4 (max = -28.9 dB) in Fig. 9.29 and blue = beam pointing out between element 2 and 3 (max = -26.2 dB).

Chapter 10

Discussion

The new ε_r of 3.55 will cause what was intended to be:

- 50 Ω lines to decrease from 49.6 Ω to 48.5 Ω.
- 70.7 Ω lines to decrease from 70.2 Ω to 68.8 Ω.
- 100 Ω lines to decrease from 97.3 Ω to 95.4 Ω.

The original impedance values are not exactly the values they were intended to be. The final values are a consequence of tuning the line widths to the best result possible.

The substrate wavelengths will also change. The wavelength is dependent on the line width since ε_{reff} have a dependance on the width, see (2.3). The substrate wavelength is the free space wavelength divided by $\sqrt{\varepsilon_{reff}}$

- 50 Ω lines: from 31.6 mm to 30.9 mm.
- 70.7 Ω lines: from 32.5 mm to 31.8 mm.
- 100 Ω lines: from 33.5 mm to 32.8 mm.

10.1 TRL Calibration Kit

As can be seen from Fig. 9.4 both the Thru and Line standard varies a great deal over the frequency range. Especially the Thru standard varies a lot with regards to S_{11}. This can be related to higher order modes exited at the launch point (SMA-to-microstrip transition) and since the Thru standard is only 1.13 wavelengths (at 5.84 GHz) long it is likely that these evanescent modes does not die out before they reach port 2. In [25] it is suggested that the Thru component should be at least 2 wavelengths long to avoid this problem. Higher order modes will cause unwanted variations during the TRL

calibration procedure [25]. From the two Figures in section 9.1.1 it can be clearly seen that the TRL calibration is faulty. Positive S-parameters from a passive device is impossible. Due to these irregularities the TRL calibrated measurements has been disregarded. Additionally, all the launchers would have to be identical to get a precise calibration. As can be seen from Fig. 8.4 a SOLT calibration will have a more loss (S_{21}) and mismatch ripples in the S_{11} measurements.

10.2 SOLT Calibration

As can be observed from the S-parameters, there is a problem with matching the DUT to the VNA. It is most likely that it is the SMA-to-microstrip launch solution that is not good enough and causes significant reflections. Due to this problem the insertion loss instead of S_{21} will be used to indicate and compare losses.

10.2.1 Tee-junction

As can be observed from the graphs in Fig. 9.5 the matching is very poor and only a fraction of the energy from port 1 enters port 2. Compared to the simulated results this is way off. The insertion loss for this device is 9.06 dB which can be translated into 4.5 dB loss in each tee-junction. This is a huge loss compared to simulated values. Since the junction has right angle it can be that it cause significant reflections that cancels out incident signals (ADS simulations are not full wave). So in retrospective it could probably have been better to have used a solution that looked more like a Y than a T or even perhaps a Wilkinson power divider. A small notch where the line splits could also help, but it would be very small and could potentially violate the design rules. A full wave solution using the integrated EMDS for ADS solver shows a loss of 2 dB for this circuit.

10.2.2 Quarter Wave Transformer

Again the matching is poor, but slightly better than for the previously discussed circuit. The insertion loss for this device which is 4 dB or 2 dB per transformer must said to be high. This component is pretty straightforward and the models used by ADS should not have any problem to simulate this circuit pretty accurate. As mentioned earlier there have been some issues regarding the connection to ground. It could be that this a certain impact on this measurement.

10.2.3 DC Network

Once again the matching is pretty bad and so is the loss measurement too. Since this circuit also contains two quarter wave transformers the insertion loss from the quarter wave transformers should be subtracted from the total insertion loss. This means that the insertion loss for the DC network will go from 3.1 dB to have a gain of 0.85 dB, which is impossible. It should be expected more loss from the DC network, it even features two hand soldered SMD capacitors which should introduce some losses in their imperfect soldering joints. This can be interpreted as a evidence for an artificially high insertion loss through the quarter wave transformer test circuit.

10.2.4 Phase Shifter

As before the matching is poor in both states of the phase shifter. This test circuit is the same as the DC network, but with a line switcher circuit in between the two DC feeds. So by deducting the insertion loss from the DC network, the switched line configuration ends up with an insertion loss of 5.7 dB and 6.2 dB for respectively the delay mode and the reference mode. These numbers are far from simulated values. This phase shifter design was designed and realized in [2] were good correspondence between simulations and measurements was found. This gives reason to believe that the simulations made here should also be pretty accurate. Looking at the S_{11} one can observe that in the measured result the phase shifter in the reference mode is better matched than in the delay mode, but for the simulated values the situation is reversed. Another difference is with regard to the insertion loss. According to Tab. 7.1 the delay mode should have 0.2 dB more loss. The measured results suggests the opposite. However, these difference could be related to how good/bad the soldering of the PIN-diodes are. They are extremely small and very difficult to solder. Most likely there is a large variance in the quality of the soldering job done on the PIN-diodes. The phase shifter was measured once more, but this time one of the PIN-diodes did not work. The PIN-diode was replaced and measurements performed. The measurement now showed a drop in S_{21} of 5 dB.

The phase shift also differs a lot from measurements. Simulations performed with the new higher dielectric constant of 3.55 results in a slightly higher phase shift than intended. The phase shift increases from 105° to 110° since the wavelength now is shorter. Looking at the measured phase shift, on can see that it is actually 144°. The measured and simulated phase of the reference line seem to be in good correspondence, but in the delay mode there is a difference equivalent to the error in phase shift. It can also be observed an error in the phase between the Line and Thru component in

Fig. 9.4. The Line component is 7.96 mm longer than the Thru component (verified by a slide gauge), but the difference in phase suggest the difference to be 10.5 mm or 120°. Simulations suggest the phase to be 90°, so here the measurements shows 30° too much. Since the phase shifter design and PIN-diode model has been found to be pretty accurate in [2], diodes and line lengths should be excluded as sources for the error. For instance a reflected signal could have been added to signal causing an error in phase (like two vectors added together), but then again such an effect should be observable in both states.

	Simulated			*Measured*		
Circuit	S_{11}	S_{21}	*IL*	S_{11}	S_{21}	*IL*
Tee	-29.7	-0.1	0.1	-6.4	-10.2	9.1
Quarter	-27.2	-0.1	0.1	-8.6	-4.6	4.0
DC	-17.5	-0.3	0.2	-4.5	-5.0	3.1
Phase delay	-16.8	-1.2	1.1	-4.1	-10.8	8.7
Phase short	-14.2	-1.1	0.9	-5.2	-10.9	9.3

Table 10.1: Comparison of simulated and measured results

10.2.5 Single Elements

Changing the dielectric constant did not have such a large influence on the feeding network, but for the MSA elements the change has a large impact. Since the wavelength decreases the resonant length will be electrically larger which results in a decreased resonance frequency of about 130 MHz. Since the SMA-to-microstrip launcher provides such a large mismatch, bandwidth assessments will be difficult.

Antenna	*Simulated* [GHz]	*Measured* [GHz]
12.6 mm	5.74	5.86
12.7 mm	5.70	5.62
12.8 mm	5.61	5.83
Static Array	5.70	5.72

Table 10.2: Comparison of simulated and measured results for the single elements and static array

As can be seen from Tab. 10.2 the 12.6 mm and 12.8 mm long patches does not agree well with the simulations. Especially the largest antenna deviates a lot from the simulated results. When looking at the Smith Charts for the single elements in section 9.1.2 one can see three large resonance circles and two smaller. The biggest of those circles is most likely the resonance

circle seen in the simulated results. If the 12.7 mm long patch did not have the resonance circle (the one marked with 5.84 GHz in Fig. 9.11) inside the larger resonance circle, the large circle would probably be situated in between the 12.6 mm circle and the 12.8 mm circle. Since all of these elements have the same probe-to-edge distance the relative distance from the probe to the edge would decrease with an increasing patch length. As closer the feed point gets to the edge, the higher the input impedance gets. An increase in input impedance will cause the impedance locus to shift towards right in the Smith Chart.

The small resonance circle mentioned above seems to be the reason why the 12.7 mm antenna is much closer to the simulated values than the two other antennas. The good correspondence between the simulated and measured result in this case is probably just a strike of luck.

10.2.6 Static Array

From Fig. 9.13 good correspondence between the simulated and measured values can be observed. The physical array seem to have a slightly higher resonance frequency and a resonance at 6.25 GHz. This resonance can also be found in the measurements from the single elements.

10.2.7 Switched Beam Array

All Phase Shifters in the Reference Mode

Looking at the Smith Chart in Fig. 9.14 one can see that the simulated results has one resonance circle while the measured has two. It seems that the small circle close to m7 is the resonance circle from the patches. Since the SMA-to-microstrip launch causes significant reflections, weaker reflections from inside the DUT can be overshadowed by this.

All Phase Shifters in the Delay Mode

Much of what was said for the reference mode array is valid here. When comparing the Smith Charts in Fig.9.16 on can notice that the delay mode has more resonance circles than the reference mode.

One Main Branch with Delay Mode and the Other in Reference Mode

Once again the large mismatch can be observed in Fig. 7.13. In the Smith Chart it can be observed that there are several resonance circles in both the measured and simulated results. The new resonances probably occurs due to mismatch and reflections due to phase shifters being in different states. According to the simulated results this will increase the BW drastically. In Fig. 9.19 a comparison between two ideally equal states has been plotted. Since the curves does not overlap each other all the way the feed network is not perfectly symmetric. The variance in PIN-diode soldering may very well be the reason for this.

Each Main Branch with both Phase Shifter States Represented

With regards to Fig. 9.18 and 9.20 the same as mentioned in the previous section applies.

10.3 Radiation Diagrams

10.3.1 Single MSA Element (12.7 mm)

From the radiation plots in Fig. 9.22 and 9.23 one can see that the cross polarization levels are very high. Since the SMA-to-microstrip launch has been suspected to cause major reflections and mismatch it was covered by absorbers to see if it radiated. In Fig 9.26 and 9.27 the measurements has been repeated with absorbers covering the SMA-to-microstrip transition. This causes the max cross polarization levels to drop by 3 dB in E-plane and 6 dB in H-plane. One can also observe a significant improvement in the co polarization H-plane radiation diagram. This improvement can be taken as evidence on that the SMA-to-microstrip is a source of mismatch and reflections. The cross-polarization is still relatively high. This could indicate that the connection to ground is still not good and currents flows on the ground plane and contributes to the cross-polarization.

10.3.2 Static Array

The measurement in Fig.9.30 shows good correspondence between the two cuts. The backward radiation is somewhat high, but most of that can be related to the feed network. If one says that the largest readout from the single element measurements is equivalent to 6 dBi (conservative estimate)

the static array would have a directivity 5 dB higher, 11 dBi (PCAAD suggests 6.1 dBi and 13.3 dBi while EMDS suggest 6.5 dBi and 12.8 dBi). By covering the feed side of the antenna with a 10x10 cm (same dimensions as the nadir panel of a CubeSat) large absorber a slightly better result could be achieved (see Fig. 9.30. Now the array directivity can be increased by 1.6 dB relative to the measurements without the absorber.

There also good correspondence between simulated and measured HPBW with both having a beamwidth of just above 40°

Compared to the single elements the static array consists of two tee-junctions in addition to the quarter wave transformer they both have. From the measurement of the tee-junction an insertion loss of 9.1 dB should be added to the array. If this had been the case the maximum S_{12} values measured from the static array should have been close to 3 dB less than what has been measured for a single element. Since the static array has somewhere around 0-2 dB less directivity compared to simulated values it can be said that this is due to increased loss in the array feeding network.

10.3.3 Switched Beam Array

Boresight Beam

The boresight beam has been measured in the x- and y-direction with all phase shifters in the reference mode in Fig. 9.32 and with the delay mode in Fig. 9.33. Since the only difference in geometry compared to the static array is a slightly larger ground plane the radiation diagrams should be pretty much the same. The two boresight diagrams result in almost inverse results between the two phase shifter states. As possible explanation is that different phase shifters and their different states has large variations in loss, the soldering of the PIN-diodes should take the blame. Even if the different elements are being exited with different amplitudes the measured values at $\theta = 0°$ should ideally be the same, but here one can observe a difference of 5-7 dB. Different phase could also cause a discrepancy, but it would also cause either on or both of the beams to have their maximum directivity in another direction than $\theta = 0°$.

Steered Beams

In Fig. 9.34 and 9.35 the steered beams has been plotted. According to PCAAD the maximum directivity should drop by 1.5 dB. The only beam that seems to be close to simulation is the blue plot in Fig. 9.34 where the beam is steered out between elements 3 and 4. Its maximum directivity

is 1.7 dB lower than the boresight beam cut along the y-axis with all the phase shifters in the reference mode. The maximum directivity occurs at 19.3°, this also the point where it intersects with the boresight beam. For a beam to have its maximum at 19.3°, PCAAD suggest a phase shift of 128.2°, which is about halfway between simulated and measured phase shift. Mutual coupling between elements can also be a factor that has an effect on the steered beams radiation diagrams.

10.4 Summarized

Looking at both S-parameter measurements and radiation diagram (Fig. 9.13, 9.30 and 9.31) the static array seems to agree well with simulations in terms of resonance frequency , directivity and HPBW. It also seems that the high insertion loss found when measuring on the tee-junction circuit is a consequence of the design of the test circuit and when used under normal operation it operates closer to expectations.

It seems that the circuits made here have two "troublemakers" among themselves. The SMA-to-microstrip launch/transition and the phase shifter.

The problem with the launcher is that it does not provide a good enough transition from the SMA inner conductor to the microstrip. It creates mismatch and reflections. As shown when measuring on the single MSA element it also radiates and is a major contributor to cross polarization. It can definitely be stated that the feeding method must be changed in order to improve performance. The feeding method must be changed anyways in order to make a flight model.

Since the phase shifter design worked good in [2], it gives reason to believe that it is the soldering of the PIN- diodes that is the source of the problems. They are so small and fragile that they should have been soldered by a professional and not by a novice like the author of this thesis. Not only could it be poor electrical contact that are the problem, but the PIN-diodes could also have been exposed to excessive heat during the soldering process. In addition to being small they are also rather expensive and in the present configuration too much power is dissipated in the 220 Ω resistors in the DC network. One PIN-diode itself should not dissipate more than 20 mW, but the present configuration uses 214 mW for each phase shifter which is way too much for CubeSat operation.

Chapter 11

Conclusion

In theory the proposed solution in this thesis will provide the NTNU student satellite with a much improved data link solution, The array solution will have no problem with being fitted to the nadir panel of a CubeSat in terms of weight and size. A drawback is that it could be difficult to fit a camera at the center of the array due to the phase shifter design. The phase shifter design also consumes too much power. The change in substrate for the MSA elements seems to be beneficiary in terms of physical strength and is probably a better solution than the original one.

The phase shifter and the fact that the wrong dielectric constant has been used are the two key factors to why the array does not operate as intended.

The S-parameter measurements presented here has a major handicap with the reflections from the SMA-to-microstrip transistion. It masks out smaller variations inside the DUT.

The static array corresponds well to simulations (when adjusted to the correct ε_r) in several ways, which suggest that the software used in the design procedure have a sufficient accuracy.

By making a better SMA-to-microstrip transition, improve the soldering work and do a redesign with the correct dielectric constant, the array configuration should work as outlined in the design process.

Chapter 12

Further Work

Fix Errors Made in This Thesis

Redesign the array so that the resonance frequency will be at 5.84 GHz. Replace the SMA-to-microstrip transition. Solder the PIN-diodes properly and reduce the power consumption for the phase shifter. The solder points for the PIN-diodes should be moved so that the soldering operation becomes easier too.

Radio Transmitter

The frequency band that the satellite downlink is located in is covered by some 802.11a [26] WiFi equipment. The occupied bandwidth for the standard is 16.6 MHz. The lowest data rate in the 802.11a standard is 6 Mbps using BPSK and 1/2 FEC so that the gross data rate is actually 12 Mbps. The FEC adds data to the stream, but the coding gain results in a larger link margin even though the bitrate increases. The AR5006XS single chip 802.11a/b/g solution from Atheros [27] provides operation up to 5.85 GHz according to its data sheet. It will probably be easier, cheaper and less time consuming to adapt this radio together with a power amplifier to the satellite compared to designing a solution from scratch.

To improve the total data-throughput from the satellite the data rate should vary with the channel. The worst case scenario that has been used when comparing array solution is very simple, but also a very poor usage of the link. The 802.11a standard only allows for data rates of 6, 9, 12, 24, 36, 48 and 54 Mbps using different coding rates and modulation schemes. If one could could modify the protocol in the WiFi radio and implement something like what is suggested in [28] the link could would be much more efficient. If

such a solution were to be realized it would set a world record as the longest WiFi link.

Array Control

Develop a system for controlling the phase shifters. It would probably be a good idea to link it to TT&C and the ADCS systems.

Bibliography

[1] A. J. Bolstad, "C-Band Patch Antenna Array for a Small Student Satellite," Project report, NTNU, December 2008.

[2] Dag Kjetil Sjaaeng, "Konstruksjon av faseskiftere for plane gruppeantenner," Master's thesis, NTH, December 1993.

[3] C. A. Balanis, Antenna Theory, Analysis and Design. John Wiley & Sons, New York, 3rd ed., 2005.

[4] G. Kumar and K. P. Ray, Broadband Microstrip Antennas. Artech House, Boston, 2003.

[5] J. A. AAs, "Exercise 10." Exercise in TTT4215 Antenna Engineering, 2008.

[6] R. J. Mailloux, Phased Array Antenna Handbook. Artech House, Boston, 2nd ed., 2005.

[7] G. Stette, Kort innføring i Romteknologi. NTNU, 2006.

[8] Wiley J. Larson and James R. Wertz, Space Mission Analysis and Design. Microcosm, Inc and Kluwer Academic Publishers, 2nd ed., 1992.

[9] A. K. Maini and V. Agrawal, Satellite Technology. Priciples and Applications. John Wiley & Sons, New York, 2007.

[10] "Agilent Specifying Calibration Standards for the Agilent," tech. rep.

[11] "Background for CubeSat." `http://cubesat.atl.calpoly.edu/pages/home/background.php`, 11th May 2009.

[12] E. Blom, Erik Narverud, and Roger Birkeland, "Design of a Small Student Satellite," Project report, NTNU, December 2006.

[13] E. Narverud, "Design of a UHF Radio System for Small LEO Satellites," Master's thesis, NTNU, July 2007.

[14] "National Table of Frequency Allocations, 300 MHz - 3 GHz." http://www.npt.no/pt_internet/ressursforvaltning/frekvenser/frekvensplan/uhf_frames.html, 19th May 2009.

[15] "National Table of Frequency Allocations, 3 GHz - 30 GHz." http://www.npt.no/pt_internet/ressursforvaltning/frekvenser/frekvensplan/shf_frames.html, 19th May 2009.

[16] C. A. Balanis, Advanced Engineering Electromagnetics. John Wiley & Sons, New York, 1989.

[17] E. O. Hammerstad, "Equations for Microstrip Circuit Design," in Proc. Fifth European Microwave Conf., pp. 268–272, September 1975.

[18] R. Garg, P. Bhartia, I. Bahl, and A. Ittipiboon, Microstrip Antenna Design Handbook. Artech House, 1st ed., 2001.

[19] D. M. Pozar, Microwave and RF Design of Wireless Systems. John Wiley & Sons, 1st ed., 2001.

[20] "PCAAD." http://www.antennadesignassociates.com, 11th May 2009.

[21] "EMDS." http://eesof.tm.agilent.com/products/emds_main.html, 11th May 2009.

[22] J. Jin, The Finite Element Method in Electromagnetics. Wiley-IEEE Press, 2nd ed., 2002.

[23] "Technical information." http://www.elprint.no/index.php/pages/35, 30th April 2009.

[24] "ADS." http://www.home.agilent.com/agilent/product.jspx?nid=-34346.0.00&cc=US&lc=eng, 11th May 2009.

[25] "Agilent Network Analysis Applying the 8510 TRL Calibration for Non-Coaxial Measurments. 8510-8a," Product Note, Agilent Technologies, August 2006.

[26] IEEE, IEEE Std 802.11a-1999, part 11.

[27] "AR5006XS Solution Highlights." http://www.atheros.com/pt/AR5006XS.htm, 18th May 2009.

[28] Z. Ye and G.J. Saulnier M. J. Medley., "Rate Adaptive OFDM (RA-OFDM) Spread Spectrum System for LEO Satellite Communications," vol. 1, pp. 621–625, 1999.

Appendix A

CubeSat Standard

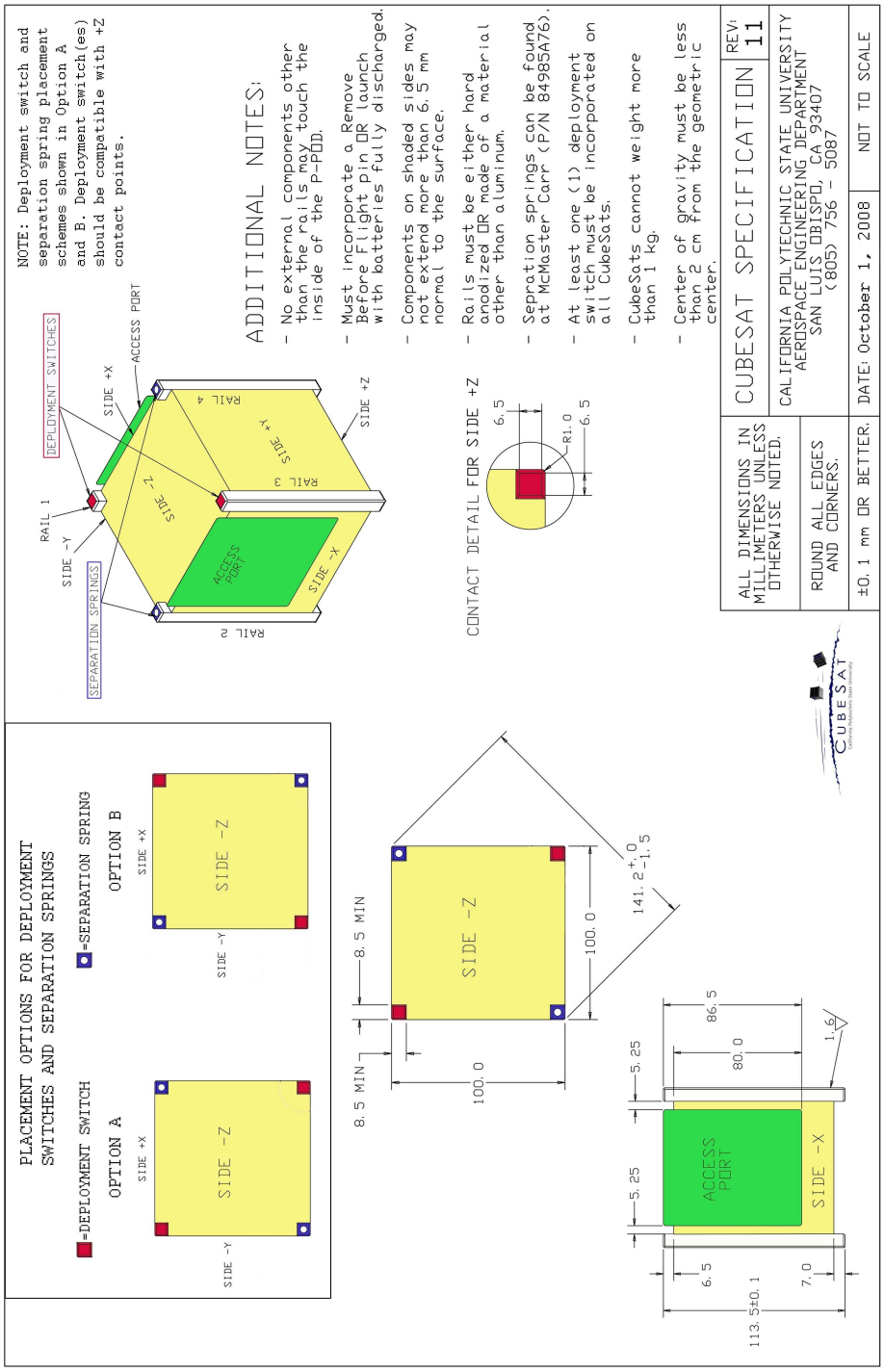
NOTE: Deployment switch and separation spring placement schemes shown in Option A and B. Deployment switch(es) should be compatible with +Z contact points.
ADDITIONAL NOTES:
- No external components other than the rails may touch the inside of the P-POD.
- Must incorporate a Remove Before Flight pin OR launch with batteries fully discharged.
- Components on shaded sides may not extend more than 6.5 mm normal to the surface.
- Rails must be either hard anodized OR made of a material other than aluminum.
- Separation springs can be found at McMaster Carr (P/N 8498A76).
- At least one (1) deployment switch must be incorporated on all CubeSats.
- CubeSats cannot weight more than 1 kg.
- Center of gravity must be less than 2 cm from the geometric center.
CONTACT DETAIL FOR SIDE +Z
DEPLOYMENT SWITCHES
ACCESS PORT
SEPARATION SPRINGS
RAIL 1
RAIL 2
RAIL 3
RAIL 4
SIDE -Y
SIDE +X
SIDE -Z
SIDE +Y
SIDE -X
SIDE +Z
ACCESS PORT
PLACEMENT OPTIONS FOR DEPLOYMENT SWITCHES AND SEPARATION SPRINGS
=DEPLOYMENT SWITCH
=SEPARATION SPRING
OPTION A
OPTION B
8.5 MIN
100.0
141.2+0.0 -1.5
5.25
86.5
80.0
1.6
6.5
7.0
113.5±0.1
ALL DIMENSIONS IN MILLIMETERS UNLESS OTHERWISE NOTED.
ROUND ALL EDGES AND CORNERS.
±0.1 mm OR BETTER.
CUBESAT SPECIFICATION
REV: 11
CALIFORNIA POLYTECHNIC STATE UNIVERSITY
AEROSPACE ENGINEERING DEPARTMENT
SAN LUIS OBISPO, CA 93407
(805) 756 - 5087
DATE: October 1, 2008
NOT TO SCALE
CUBESAT

Appendix B

Substrate Documentation

B.1 RT/duroid 6002 Substrate

Typical Values — **RT/duroid® 6002 High Frequency Laminates**

PROPERTY	TYPICAL VALUE[2]	DIRECTION	UNITS[1]	CONDITIONS	TEST METHOD
Dielectric Constant, ε_r	2.94 ± 0.04 (Y Spec) 2.92+-0.04	Z	--	10 GHz/23°C	IPC-TM-650, 2.5.5.5
Dissipation Factor, Tan δ	0.0012	Z	--	10 GHz/23°C	IPC-TM-650, 2.5.5.5
Thermal Coefficient of ε_r	+12	Z	ppm/°C	10 GHz/1-100°C	IPC-TM-650, 2.5.5.5
Volume Resistivity	10^6	Z	Mohm cm	A	ASTM D257
Surface Resistivity	10^7	Z	Mohm	A	ASTM D257
Tensile Modulus Ultimate Stress Ultimate Strain	828 (120) 6.9 (1.0) 7.3	X,Y X,Y X,Y	MPa (kpsi) MPa (kpsi) %	23°C	ASTM D638
Compressive Modulus	2482 (360)	Z	MPa (kpsi)		ASTM D638
Moisture Absorption	0.1 0.13 max	—	%	D23/24 D48/50	IPC-TM-650 2.6.2.1 ASTM D570
Thermal Conductivity	0.60	—	W/m/K	80°C	ASTM C518
Coefficient of Thermal Expansion	16 24	X,Y Z	ppm/°C	(10K/min)	ASTM D3386
Td	500		°C TGA		ASTM D3850
Density	2.1		gm/cm³		ASTM D792
Specific Heat	0.93 (0.22)	—	J/g/K (BTU/lb/°F)	---	Calculated
Copper Peel	8.9 (1.6)		lbs/in (N/mm)		IPC-TM-650, 2.4.8
Flammability	94V-0				UL
Lead-Free Process Compatible	Yes				

[1] S1 units given first, with other frequently used units in parentheses.

[2] References: Internal TRs 3824, 5016, 5017, 5035. Tests were at 23°C unless otherwise noted.

Typical Values should not be used for specification limits.

Typical Values should not be used for specification limits

STANDARD THICKNESS:	STANDARD PANEL SIZE:	STANDARD COPPER CLADDING:
0.005" (0.127mm) 0.010" (0.254mm) 0.020" (0.508mm) 0.030" (0.762mm) 0.060" (1.524mm) 0.120" (3.048mm)	18" X 12" (457 X 305mm) 18" X 24" (457 X 610mm)	¼ oz. (8 μm) electrodeposited copper foil. ½ oz. (17μm), 1 oz. (35μm), 2 oz. (70μm) electrodeposited and rolled copper foil. Unclad material 0.020" or greater is available. Thick metal claddings are available. Contact customer service for more information.

CONTACT INFORMATION:

USA:	Rogers Advanced Circuit Materials, ISO 9002 Certified	Tel: 480-961-1382	Fax: 480-961-4533
Belgium:	Rogers N.V. - Gent	Tel: +32-9-2353611	Fax: +32-9-2353658
Japan:	Rogers Japan Inc.	Tel: 81-3-5200-2700	Fax: 81-3-5200-0571
Taiwan:	Rogers Taiwan Inc.	Tel: 886-2-86609056	Fax: 886-2-86609057
Korea:	Rogers Korea Inc.	Tel: 82-31-716-6112	Fax: 82-31-716-6208
Singapore:	Rogers Technologies Singapore Inc.	Tel: 65-747-3521	Fax: 65-747-7425
China:	Rogers (Shanghai) International Trading Co., Ltd	Tel: 86-21-63916088	Fax: 86-21-63915060

B.2 RO4003C Substrate

Property	Typical Value		Direction	Units	Condition	Test Method
	RO4003C™	RO4350B™				
Dielectric Constant, ε_r (Process specification)	3.38 ± 0.05	[1] 3.48 ± 0.05	Z	--	10 GHz/23°C	IPC-TM-650 2.5.5.5 [2]Clamped Stripline
[3] Dielectric Constant, ε_r (Recommended for use in circuit design)	3.55	3.66	Z	--	FSR/23°C	IPC-TM-650 2.5.5.6 Full Sheet Resonance
Dissipation Factor tan, δ	0.0027 0.0021	0.0037 0.0031	Z	--	10 GHz/23°C 2.5 GHz/23°C	IPC-TM-650 2.5.5.5
Thermal Coefficient of ε_r	+40	+50	Z	ppm/°C	-100°C to 250°C	IPC-TM-650 2.5.5.5
Volume Resistivity	1.7 X 10^{10}	1.2 X 10^{10}		MΩ•cm	COND A	IPC-TM-650 2.5.17.1
Surface Resistivity	4.2 X 10^{9}	5.7 X 10^{9}		MΩ	COND A	IPC-TM-650 2.5.17.1
Electrical Strength	31.2 (780)	31.2 (780)	Z	KV/mm (V/mil)	0.51mm (0.020")	IPC-TM-650 2.5.6.2
Tensile Modulus	26,889 (3900)	11,473 (1664)	Y	MPa (kpsi)	RT	ASTM D638
Tensile Strength	141 (20.4)	175 (25.4)	Y	MPa (kpsi)	RT	ASTM D638
Flexural Strength	276 (40)	255 (37)		MPa (kpsi)		IPC-TM-650 2.4.4
Dimensional Stability	<0.3	<0.5	X,Y	mm/m (mils/inch)	after etch +E2/150°C	IPC-TM-650 2.4.39A
Coefficient of Thermal Expansion	11 14 46	14 16 35	X Y Z	ppm/°C	-55 to 288°C	IPC-TM-650 2.1.41
Tg	>280	>280		°C DSC	A	IPC-TM-650 2.4.24
Td	425	390		°C TGA		ASTM D3850
Thermal Conductivity	0.64	0.62		W/m/°K	100°C	ASTM F433
Moisture Absorption	0.06	0.06		%	48 hrs immersion 0.060" sample Temperature 50°C	ASTM D570
Density	1.79	1.86		gm/cm^3	23°C	ASTM D792
Copper Peel Strength	1.05 (6.0)	0.88 (5.0)		N/mm (pli)	after solder float 1 oz. EDC Foil	IPC-TM-650 2.4.8
Flammability	N/A	94V-0				UL
Lead-Free Process Compatible	Yes	Yes				

(1) Dielectric constant typical value does not apply to 0.004" (0.101mm) laminates. Dielectric constant specification value for 0.004 RO4350B material is 3.36.
(2) Clamped stripline method can potentially lower the actual dielectric constant due to presence of airgap. Dielectric constant in practice may be higher than the values listed.
(3) Typical values are a representation of an average value for the population of the property. For specification values contact Rogers Corporation.

Prolonged exposure in an oxidative environment may cause changes to the dielectric properties of hydrocarbon based materials. The rate of change increases at higher temperatures and is highly dependent on the circuit design. Although Rogers' high frequency materials have been used successfully in innumerable applications and reports of oxidation resulting in performance problems are extremely rare, Rogers recommends that the customer evaluate each material and design combination to determine fitness for use over the entire life of the end product.

Standard Thickness	Standard Panel Size	Standard Copper Cladding
RO4003C: 0.008" (0.203mm), 0.012 (0.305mm), 0.016" (0.406mm), 0.020" (0.508mm) 0.032" (0.813mm), 0.060" (1.524mm) **RO4350B**: *0.004" (0.101mm), 0.0066" (0.168mm) 0.010" (0.254mm), 0.0133 (0.338mm), 0.0166 (0.422mm), 0.020" (0.508mm) 0.030" (0.762mm), 0.060" (1.524mm)	12" X 18" (305 X457 mm) 24" X 18" (610 X 457 mm) 24" X 36" (610 X 915 mm) 48" X 36" (1.224 m X 915 mm) *0. 004" material in not available in panel sizes larger than 24"x18" (610 X 457mm).	½ oz. (17µm), 1 oz. (35µm) and 2 oz. (70µm) electrodeposited copper foil.

B.3 RO4450 Prepreg

Typical Values **RO4450B, RO4450F Prepreg**

PROPERTY	RO4450B		RO4450F	DIRECTION	UNITS	CONDITION	TEST METHOD
Thickness	4 (0.102)	3.6 (0.091)	4 (0.102)	Z	mils (µm)	-	-
Dielectric Constant, ε_r	3.54 ± 0.05	3.30 ± 0.05	3.52 ± 0.05	Z	-	10GHz - 23°C	IPC-TM-650, 2.5.5.5
Dissipation Factor, tan δ	0.004	0.004	0.004	Z	-	10GHz-23°C	IPC-TM-650, 2.5.5.5
Dielectric Strength	1000	1000	1000	Z	V/mil	23°C/50% RH	IPC-TM-650, 2.5.6
Volume Resistivity	>2.5 X 10^{10}	>2.5 X 10^{10}	TBD	-	MΩ•cm	23°C/50% RH	IPC-TM-650, 2.5.17.1
Surface Resistivity	1.9X10^{8}	1.9 X 10^{8}	TBD	X,Y	MΩ	23°C/50% RH	IPC-TM-650, 2.5.17.1
Thermal Conductivity	0.60	0.60	0.65	Z	W/m/K	100°C	ASTM F433
Moisture Absorption	0.05	0.10	0.09	-	%	48 hrs immersion 0.060" sample temperature 50°C	ASTM D570
Tg	>280	>280	>280	-	°C TMA	-60°C - 300°C @ 10°C/min	IPC-TM-650 2.4.24
Td	390	390	390	-	°C TGA		ASTM D3850
Density	1.86	1.80	1.83	-	gm/cm^3	23°C	ASTM D792
Dimensional Stability	TBD	TBD	-0.065	X,Y	mils/inch	After Etch +E2/150	IPC-TM-650, 2.2.4
Copper Adhesion	4.9* (0.86)	4.0* (0.70)	4.0* (0.70)	Z	pli (N/mm)	After Solder Float	IPC-TM-650, 2.4.8
Coefficient of Thermal Expansion	19 17 50	19 17 60	19 17 50	X Y Z	ppm/°C	-55 to 280°C	IPC-TM-650, 2.4.41
Color	White	White	White	-	-	-	-
Flammability	94V-0	94V-0	94 V-0				
Lead-Free Process Compatible	Yes	Yes	Yes				

Typical values are a representation of an average value for the population of the property. For specification values contact Rogers Corporation.

*Tested on ½ oz. EDC foil for RO4450B. Rogers UL file number is E102763B.

STANDARD THICKNESS:	STANDARD SIZE:
RO4450F: 0.004", (0.101mm) RO4450B: 0.0036 (0.091mm), 0.004", (0.101mm)	24X18" Sheets (610mm X 457mm) Contact Customer Service for other available sizes.

The information contained in this data sheet and processing guide is intended to assist you in designing with Rogers' circuit materials and prepreg. It is not intended to and does not create any warranties, express or implied, including any warranty of merchantability or fitness for a particular purpose or that the results shown on this data sheet and processing guide will be achieved by a user for a particular purpose. The user is responsible for determining the suitability of Rogers' circuit materials and prepreg for each application.

Prolonged exposure in an oxidative environment may cause changes to the dielectric properties of hydrocarbon based materials. The rate of change increases at higher temperatures and is highly dependent on the circuit design. Although Rogers' high frequency materials have been used successfully in innumerable applications and reports of oxidation resulting in performance problems are extremely rare, Rogers recommends that the customer evaluate each material and design combination to determine fitness for use over the entire life of the end product.

These commodities, technology and software are exported from the United States in accordance with the Export Administration regulations. Diversion contrary to U.S. law prohibited.

Revised 04/2009 0861-0409-CC **Publication #92-005**

B.4 Outgassing Resistance

MICRO-GRAM

As a quarterly feature of the Micro-Gram, Arturo Aguayo, Jr. is doing a series of question and answer articles of special interest to you. He will feature questions most frequently asked by our customers and will respond to those questions. E-mail: art.aguayo@rogers-corp.com.

Question: **I'm in the process of designing circuitry for space applications. Which Rogers high frequency materials should I be evaluating?**

by Art Aguayo, Jr.

Answer: Rogers high frequency materials have been used in space-qualified hardware for many years for antennas, power dividers, transceivers, and power modules. The materials used range from RT/duroid® to TMM® grades, and currently, several programs have been working with the RO4000® family. There is no certification process for materials to be labeled *space qualified*; this qualification is done on finished hardware. A requirement placed on materials by NASA, is for them to have low outgassing resistance (expressed as % of original specimen mass) as measured by Total Mass Loss (TML), Collected Volatile Condensable Materials (CVCM) and Water Vapor Recovered (WVR). Materials used should have a TML less than 1% and both CVCM and WVR should be less than 0.1%. Table I presents these properties, along with the nominal dielectric constant and loss tangent at 10 GHz, for the various materials tested by NASA. It can be seen that many materials from Rogers meet NASA's requirement for outgassing resistance. This data, along with an extensive database of various materials can be found at the NASA website http://misspiggy.gsfc.nasa.gov/og/.

Table I. Outgassing Resistance of Various Rogers High Frequency Materials.

	RT/duroid 5870	RT/duroid 5880	RT/duroid 6010	RT/duroid 6002	TMM 3	TMM 10	RO4003
Composition	PTFE glass-microfiber	PTFE glass-microfiber	PTFE glass-microfiber ceramic filler	PTFE glass-microfiber ceramic filler	Thermoset polymer ceramic filler	Thermoset polymer ceramic filler	Thermoset polymer ceramic filler woven glass
Diel. Const.	2.33	2.2	10.2	2.94	3.27	9.2	3.38
Loss Tangent	0.0012	0.0009	0.0023	0.0012	0.0020	0.0023	0.0027
% TML	0.05	0.03	0.03	0.02	0.03	0.06	0.06
% CVCM	0	0	0	0.01	0	0	0
% WVR	0.04	0.02	0.02	0.01	0.03	0.04	0.02

Outgassing resistance is not the only property desired. Because of the harsh temperature environment, materials with stable electrical and mechanical performance should be selected. Stable dielectric constant versus temperature (TCEr) would minimize frequency shifting of circuitry while low Z-axis expansion provides for higher plated through hole reliability. Table II summarizes these properties for the materials presented in Table I.

Table II. TCεr and CTE of Various Rogers High Frequency Materials

	RT/duroid 5870	RT/duroid 5880	RT/duroid 6010	RT/duroid 6002	TMM 3	TMM 10	RO4003
TCεr, ppm/°C -50 to 150C	-115	-125	-425	+12	+39	-39	+40
CTE (Z), ppm/°C -0 to 100C	173	237	24	24	20	20	46

It can be noted from Table II that the better materials for space programs would be RT/duroid 6002, TMM-3, TMM-10, and RO4003 materials. RT/duroid 6002 and RO4003 materials would be better suited for applications requiring multilayer constructions, while TMM materials, because of their rigidity, are used as replacement for ceramic circuitry. RT/duroid 5870, 5880 and 6010 can and have been used in various space programs, but require additional design considerations to compensate for the larger TCEr and CTE. Rogers Corporation Microwave Materials Division has an extensive selection of high frequency materials; many of them ideal for space programs. Selection of the best material for these applications depends on the desired construction and functionality.

Appendix C

Datasheet for the PIN-diode HPND-4005

HPND- 4005
Beam Lead PIN Diode

AVAGO TECHNOLOGIES

Data Sheet

Description

The HPND-4005 planar beam lead PIN diode is constructed to offer exceptional lead strength while achieving excellent electrical performance at high frequencies. High beam strength offers users superior assembly yield, while extremely low capacitance allows high isolation to be realized.

Nitride passivation and polyimide coating provide reliable device protection.

Applications

The HPND-4005 beam lead PIN diode is designed for use in stripline or microstrip circuits. Applications include switching, attenuating, phase shifting, limiting, and modulating at microwave frequencies. The extremely low capacitance of the HPND-4005 makes it ideal for circuits requiring high isolation in a series diode configuration.

Maximum Ratings

Operating Temperature	-65°C to +175°C
Storage Temperature	-65°C to +200°C
Power Dissipation at TCASE = 25°C (Derate linearly to zero at 175°C.)	250 mW
Minimum Lead Strength	4 grams pull on either lead
Diode Mounting Temp	220°C for 10 sec. max.

Features

- High Breakdown Voltage: 120 V Typical
- Low Capacitance: 0.017 pF Typical
- Low Resistance: 4.7 Ω Typical
- Rugged Construction: 4 Grams Minimum Lead Pull
- Nitride Passivated

Outline 21

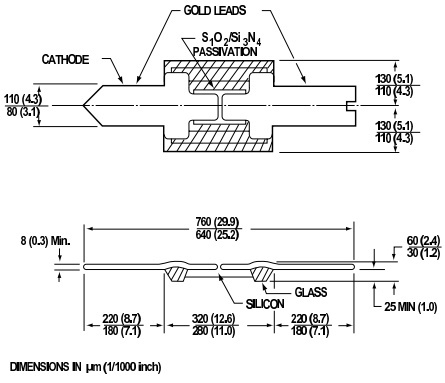

DIMENSIONS IN µm (1/1000 inch)

Electrical Specifications at $T_A = 25°C$

Part Number	Breakdown Voltage V_{BR} (V)		Series Resistance R_S (Ω)[2]		Capacitance C_T (pF)[1,2]		Forward Voltage V_F (V)	Reverse Current I_R (nA)	Minority Carrier Lifetime τ (ns)[2]	
HPND-	Min.	Typ.	Typ.	Max.	Typ.	Max.	Max.	Max.	Min.	Typ.
4005	100	120	4.7	6.5	0.017	0.02	1.0	100	50	100
Test Conditions	$I_R = 10\ \mu A$		$I_F = 20$ mA $I_F = 100$ MHz		$V_R = 10$ V f = 10 GHz		$I_F = 20$ mA	$V_R = 30$ V	$I_F = 10$ mA $I_R = 6$ mA	

Notes:
1. Total capacitance calculated from measured isolation value in a series configuration.
2. Test performed on packaged samples.

Typical Parameters

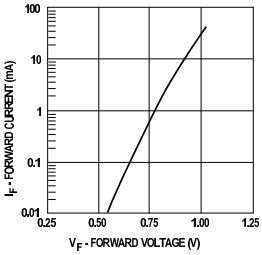

Figure 1. Typical Forward Conduction Characteristics.

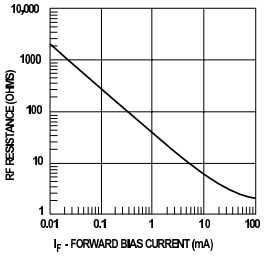

Figure 2. Typical RF Resistance vs. Forward Bias Current.

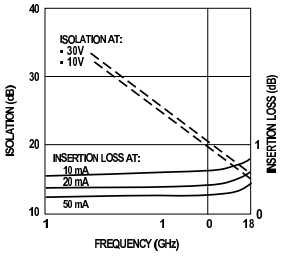

Figure 3. Typical Isolation and Insertion Loss in the Series Configuration ($Z_O = 50$ ½).

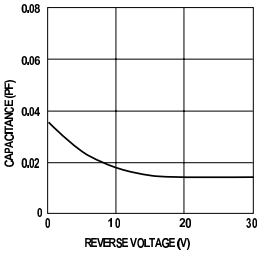

Figure 4. Typical Capacitance at 10 GHz vs. Reverse Bias.

Appendix D

MATLAB Script

```
Zf = (4.7000 + 5.4924i)./100; %Normalized diode impedance
                              in the direction of conduction (on mode)
Zr = (1.3417e+03 - 1.4925e+03i)./100; %Normalized diode impedance
                                      in the direction of conduction (off mode)
phase =107; %Difference in electrical length
            to achieve a phaseshift of 106.8 degrees

fi = 10:2.5:180;
fi1 = fi * pi ./180;
fi2 = fi1 +phase*pi./180;

S21a = 1 ./(1+1./(Zf-i*cot(fi1./2))+1 ./(Zr-i*cot(fi2./2)))
        -1 ./(1+1./(Zf+i*tan(fi1./2)) +1 ./(Zr+i*tan(fi2./2)));

S21b = 1 ./(1+1./(Zr-i*cot(fi1./2))+1 ./(Zf-i*cot(fi2./2)))
        -1 ./(1+1./(Zr+i*tan(fi1./2)) +1 ./(Zf+i*tan(fi2./2)));

diff = S21a ./S21b;

phaseshift = 180 ./ pi * angle(diff);
As21a = 20*log10(abs(S21a));
As21b = 20*log10(abs(S21b));


figure(1),
plot(fi,phaseshift),
title('106.8 degrees line-switched phase shifter with hpnd4005'),
xlabel('Length of L1 in degrees'),
ylabel('Phaseshift in degrees'),grid,
figure(2),
plot(fi,As21a,fi,As21b),
title('106.8 degrees line-switched phase shifter with hpnd4005'),
xlabel('Length of L1 in degrees'),
ylabel('Insertion loss in dB'),grid;
```

Appendix E

Various Parmeters Dependence on the Elevation Angle

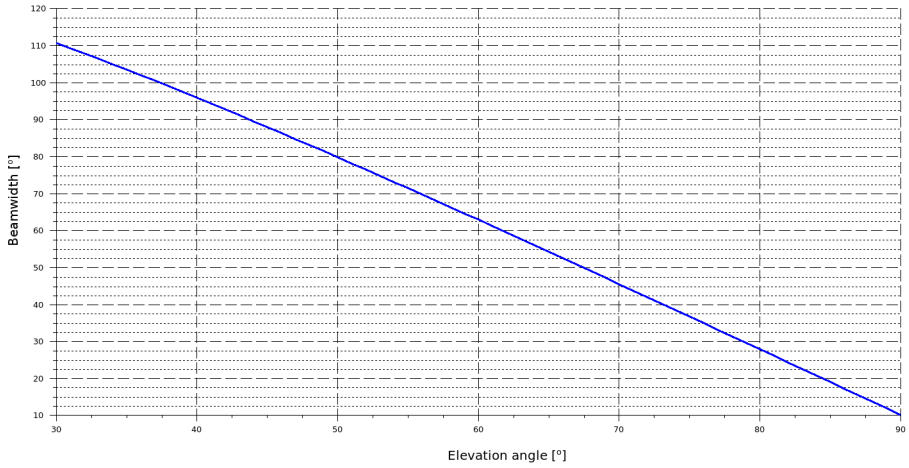

Figure E.1: Elevation angle versus needed beamwidth to give complete covereage.

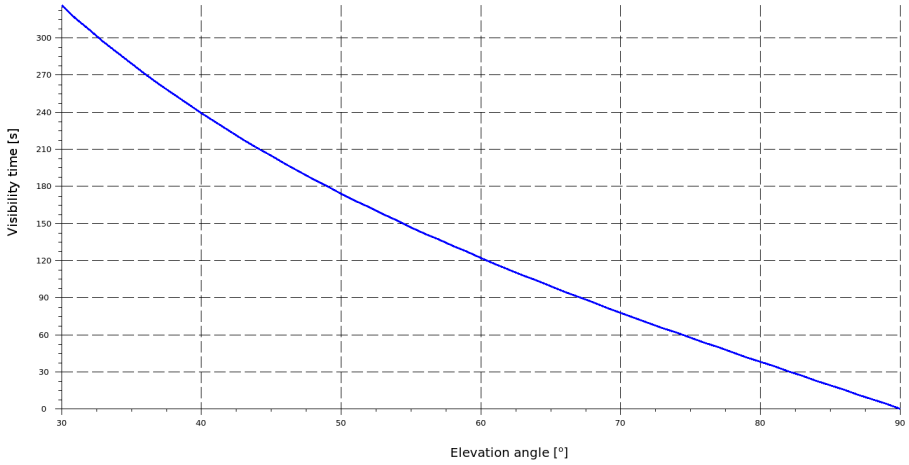

Figure E.2: Elevation angle versus visibility time.

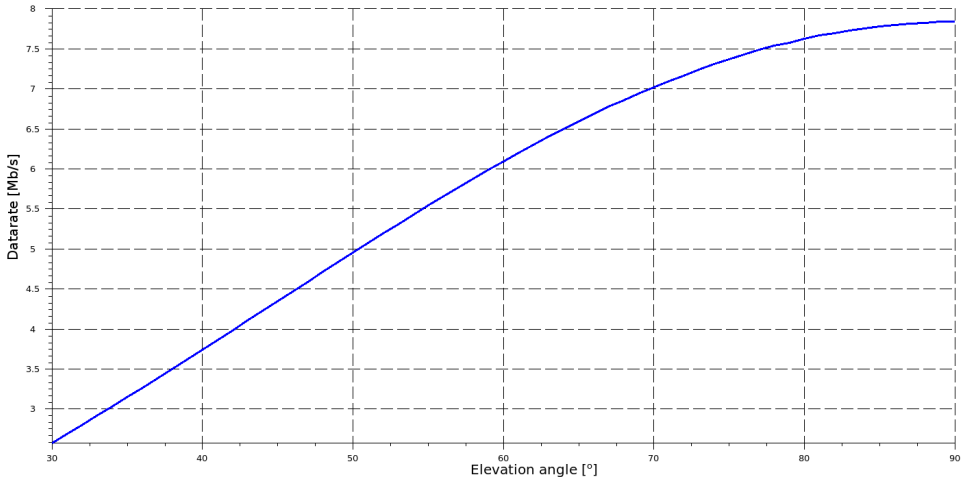

Figure E.3: Elevation angle versus maximum datarate from an antenna with D = 11.4 dBi.

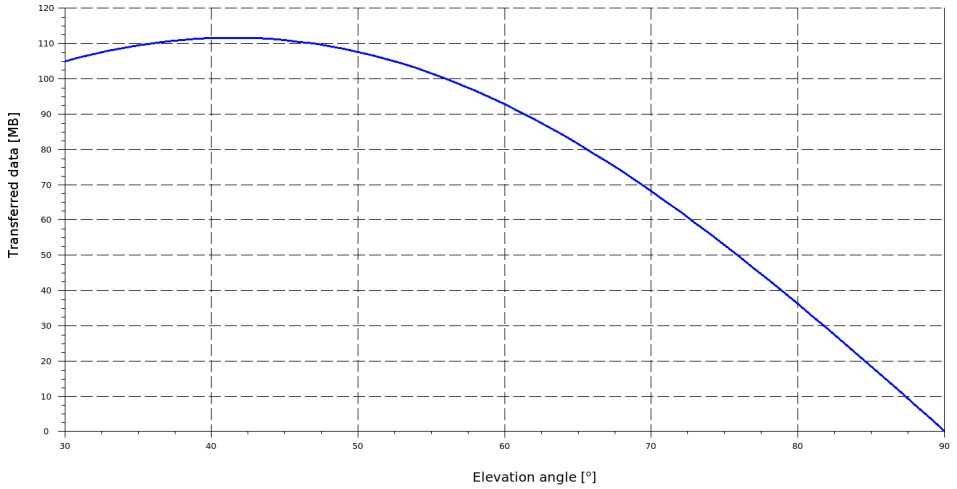

Figure E.4: Elevation angle versus transferred data amount when the data rate varies like in Fig. E.3.

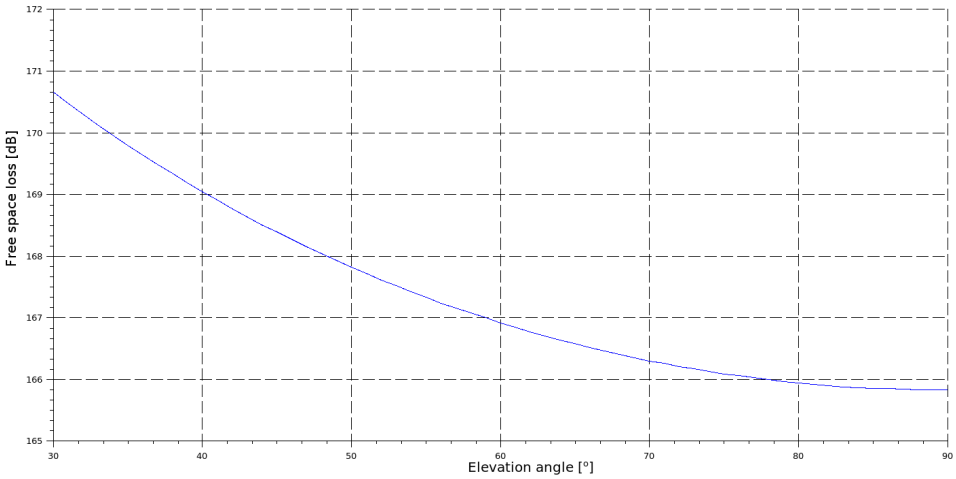

Figure E.5: Elevation angle versus free space loss.

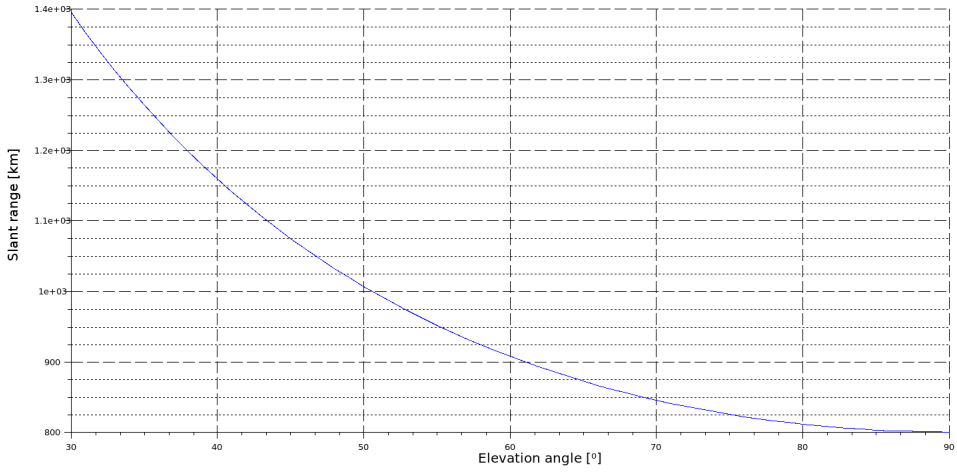

Figure E.6: Elevation angle versus slant range.

Appendix F

ADS Circuits and Results from Chapter 7

F.1 Tee-junction

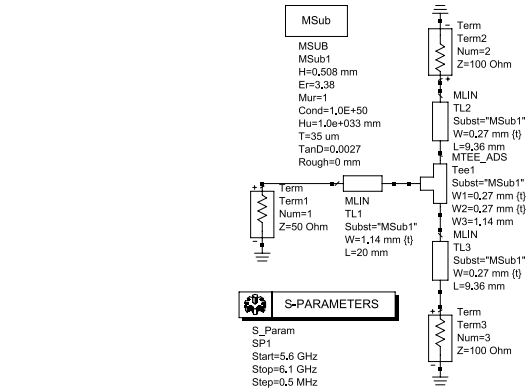

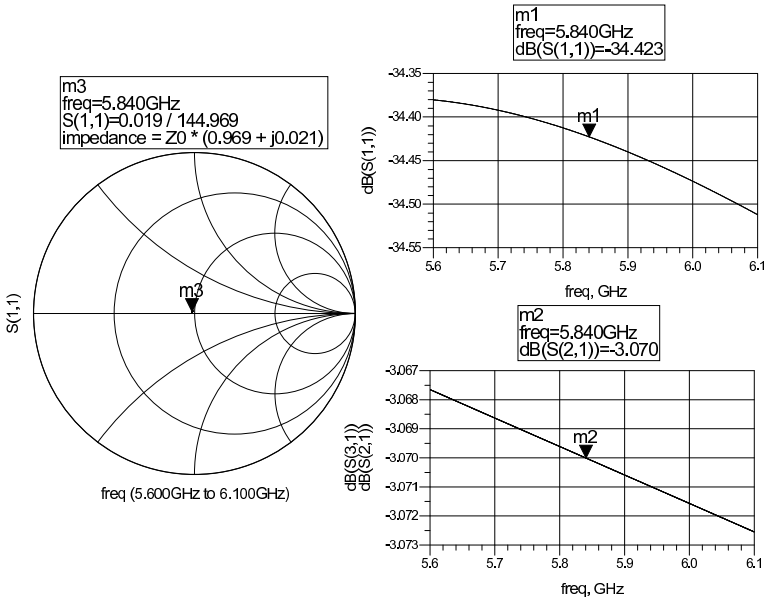

F.2 Tee-junction plus Quarter Wave Transformers

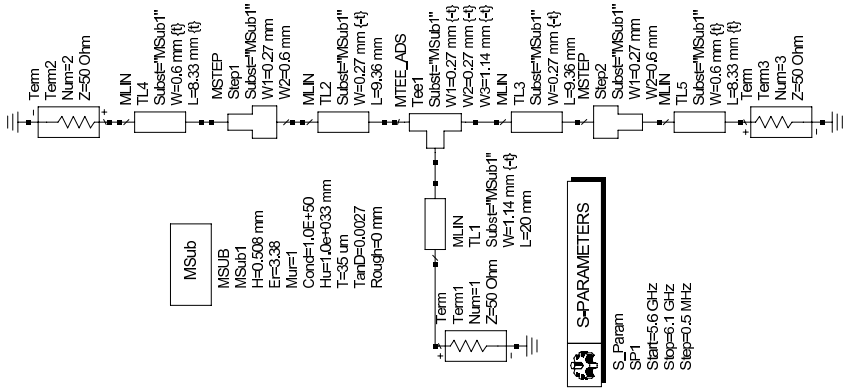

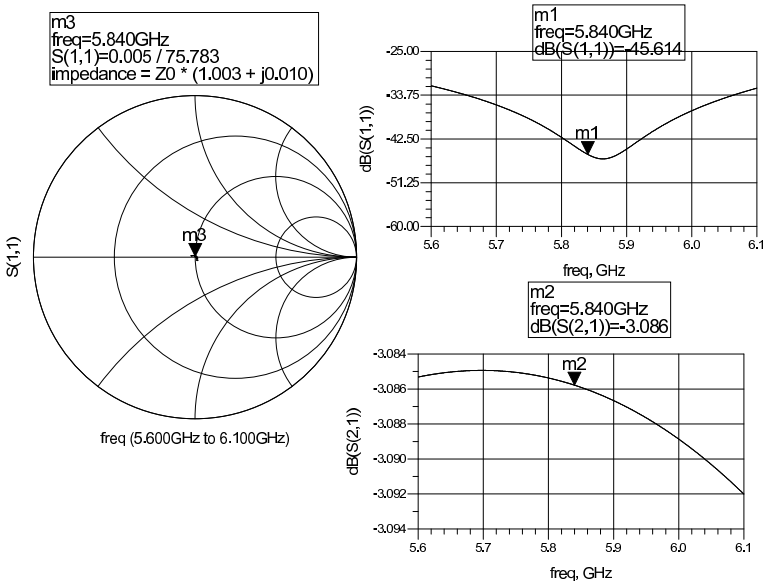

F.3 Feed Network up till the Second Bend

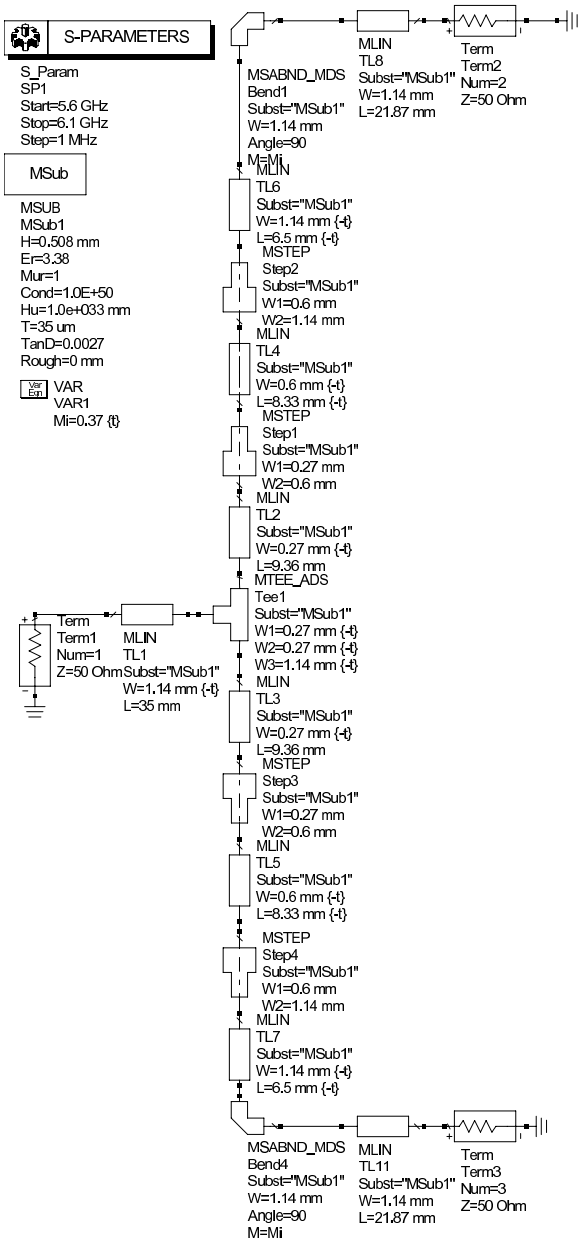

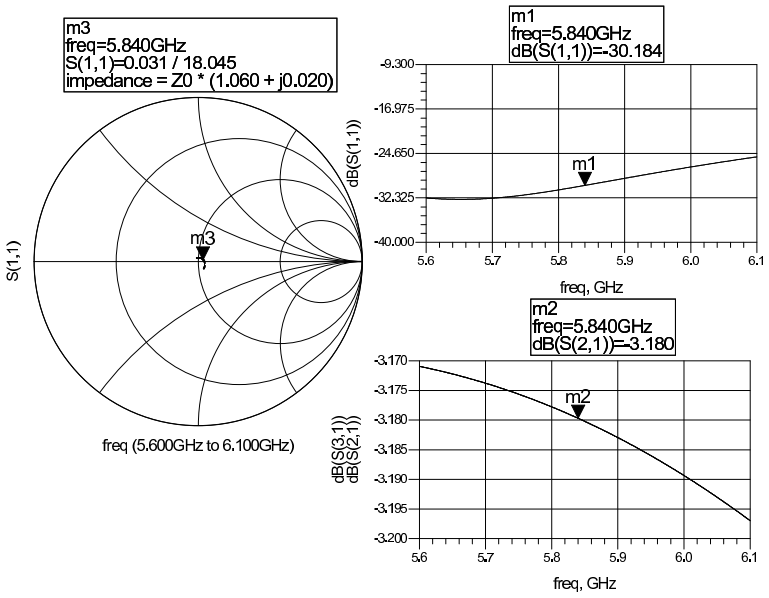

F.4 Static Feed Network

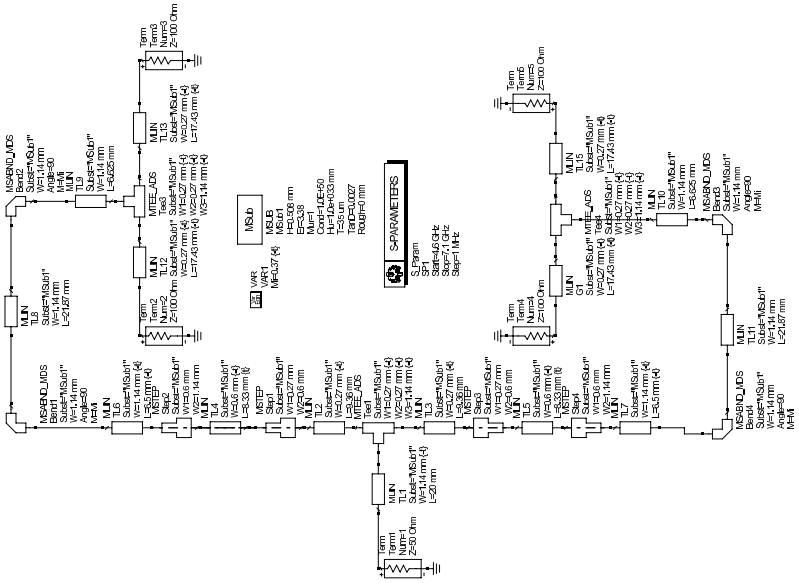

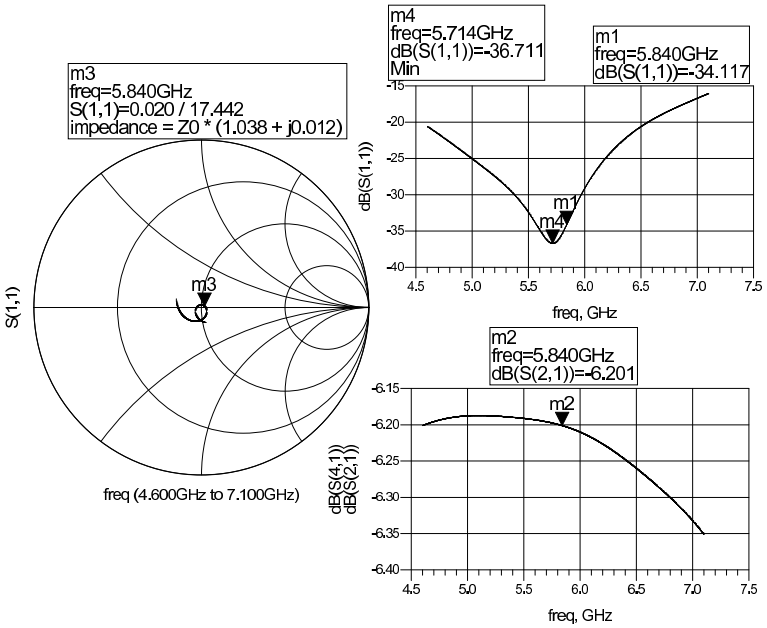
m4
freq=5.714GHz
dB(S(1,1))=-36.711
Min
m1
freq=5.840GHz
dB(S(1,1))=-34.117
m3
freq=5.840GHz
S(1,1)=0.020 / 17.442
impedance = Z0 * (1.038 + j0.012)
dB(S(1,1))
freq, GHz
S(1,1)
freq (4.600GHz to 7.100GHz)
m2
freq=5.840GHz
dB(S(2,1))=-6.201
dB(S(4,1))
dB(S(2,1))
freq, GHz

F.5 Line Switcher

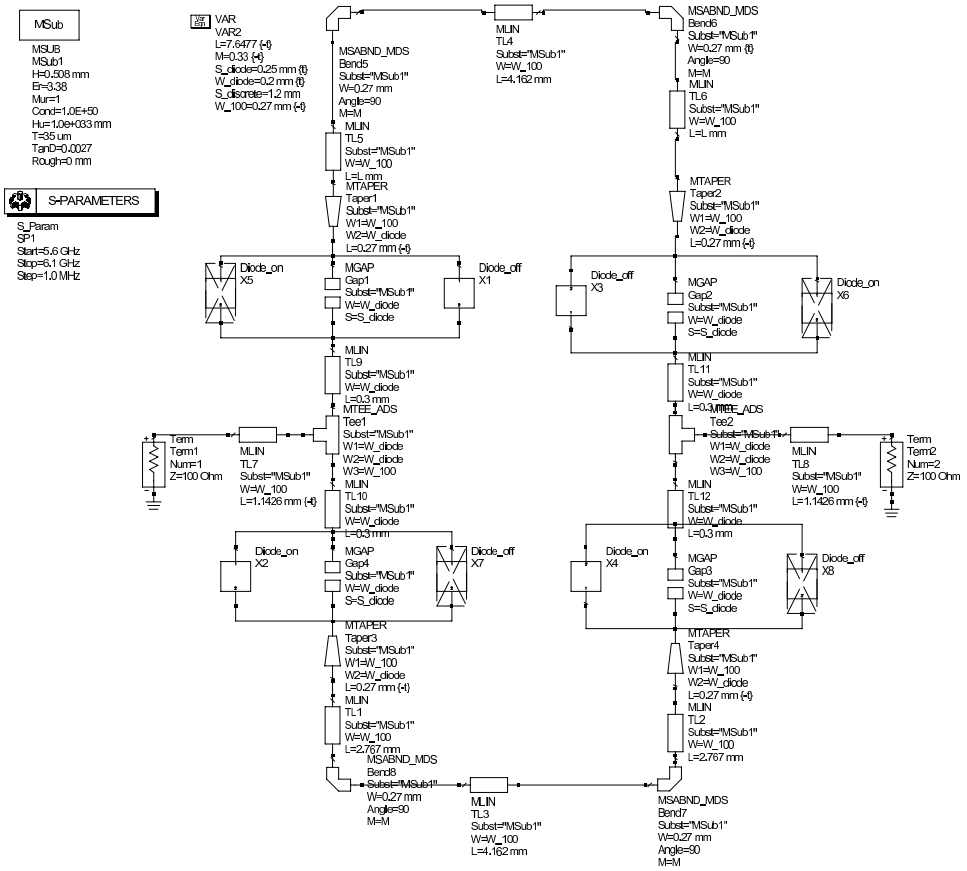

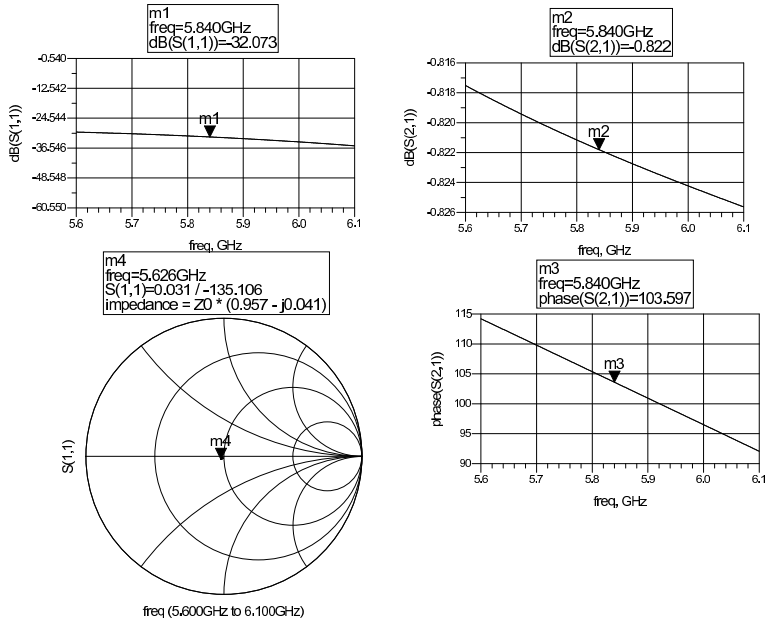

Figure F.1: Simulation results for the line swither in delay mode.

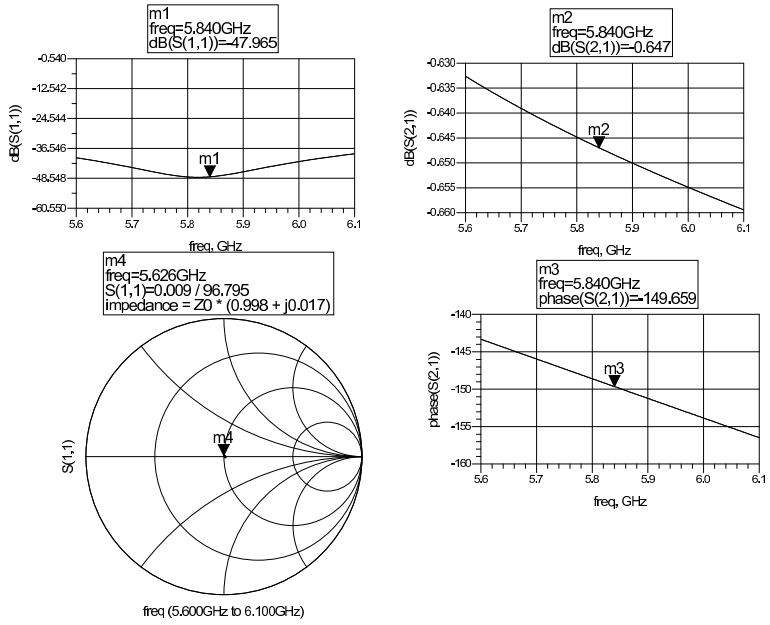

Figure F.2: Simulation results for the line swither in reference mode.

F.6 DC-Network

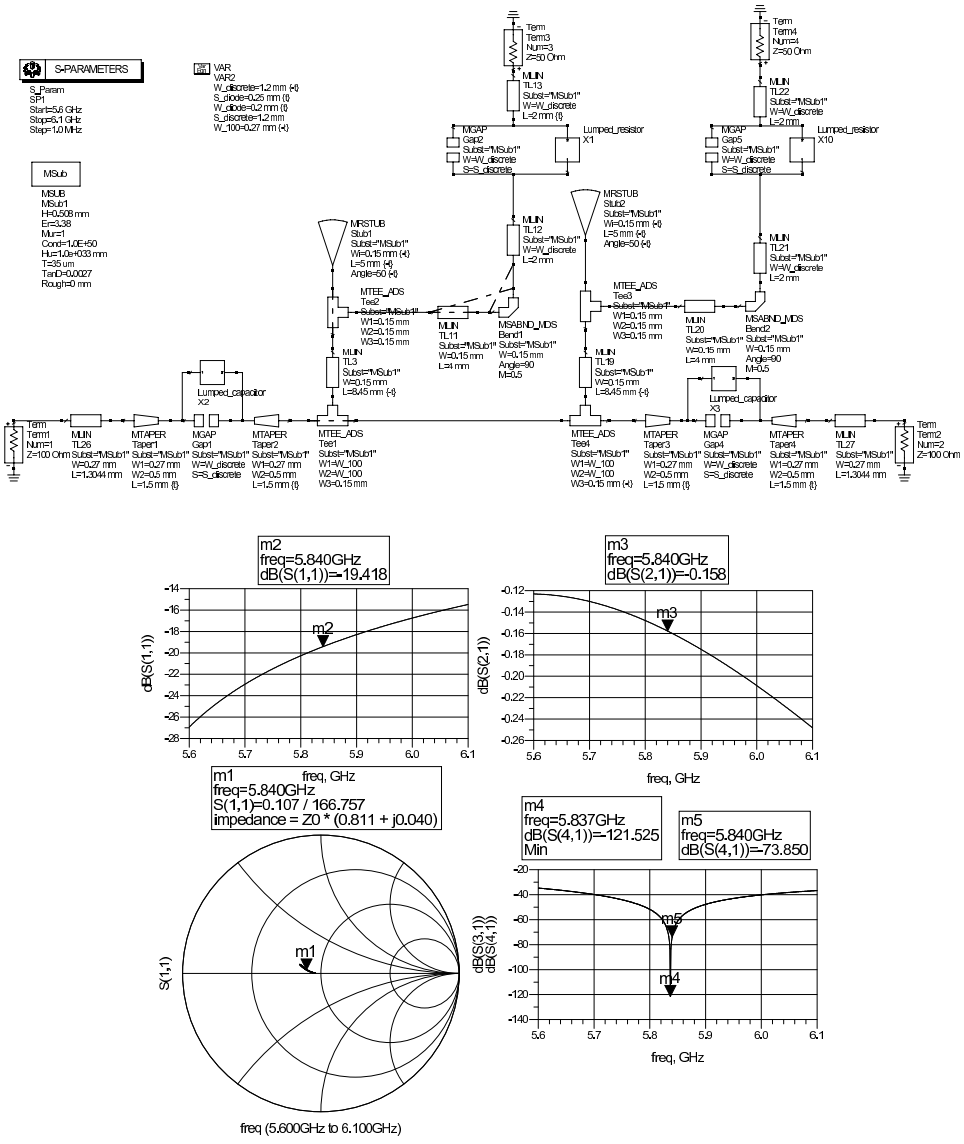

Figure F.3: S_{31} and S_{41} shows how much RF power that leaks out.

F.7 Phase Shifter

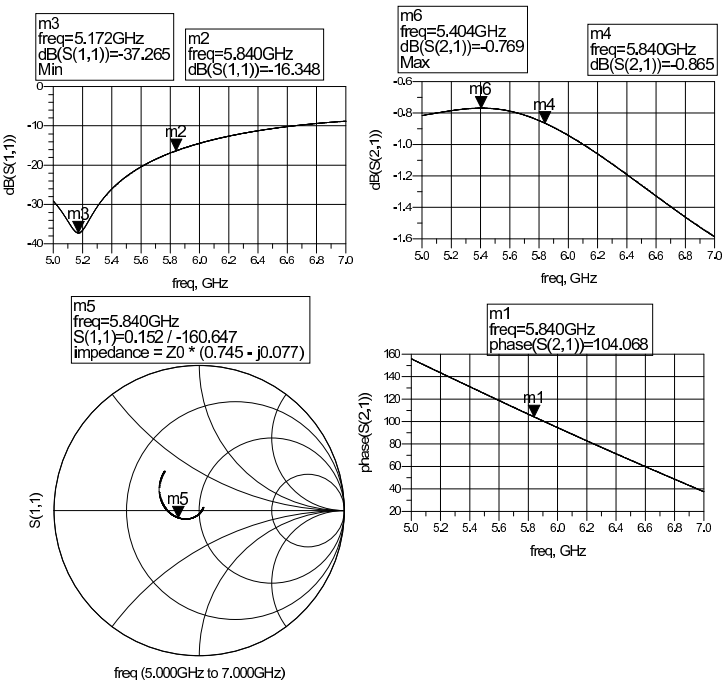

Figure F.4: Simulations results for the phase shifter along the reference line.

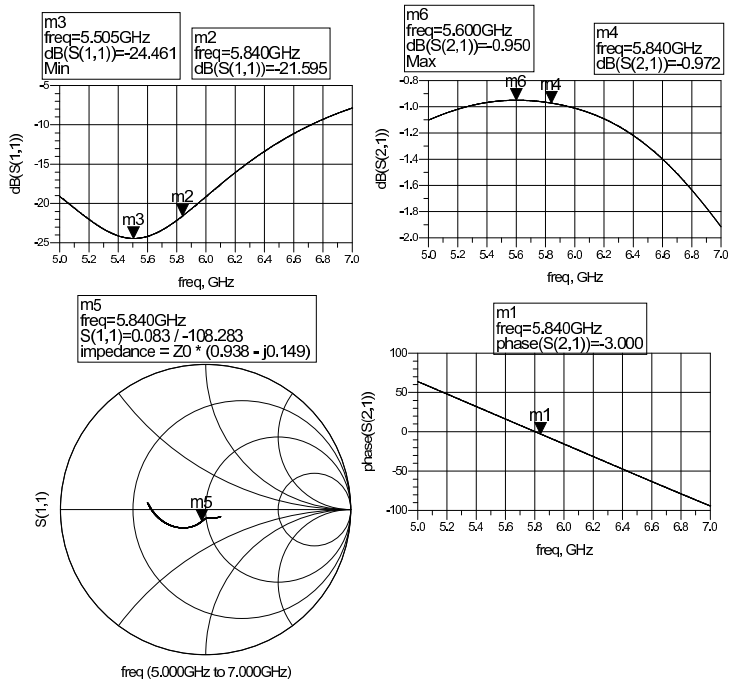

Figure F.5: Simulations results for the phase shifter along the delay line.

F.8 Complete Feed Network

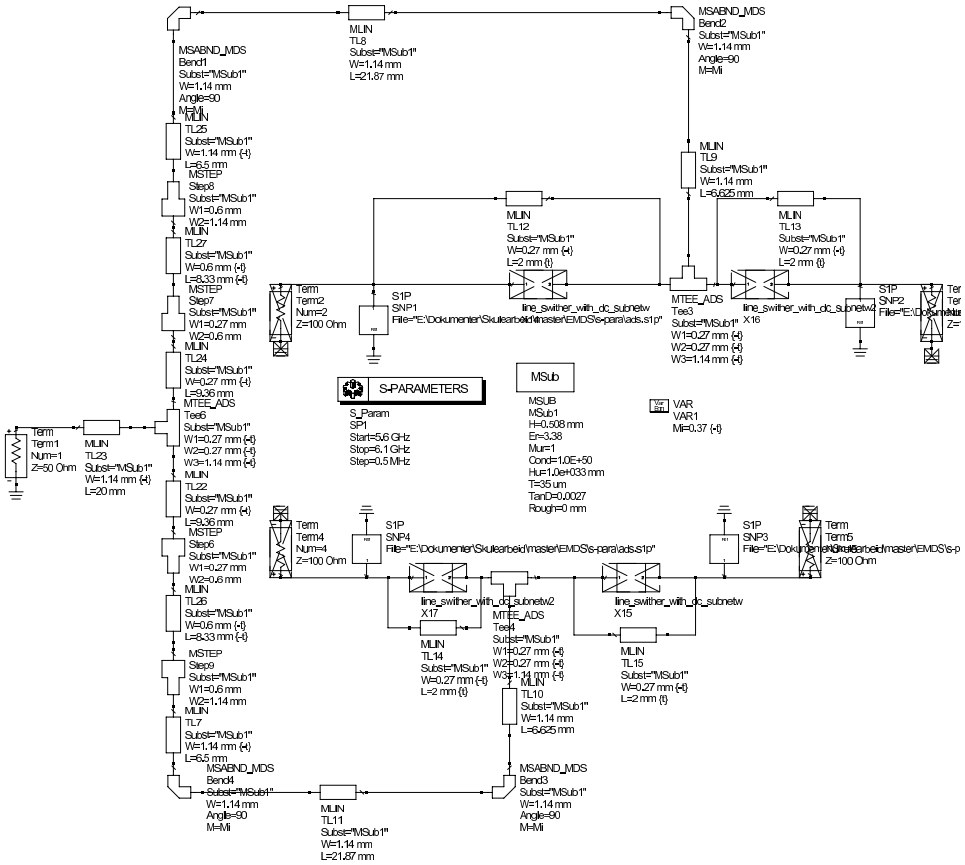

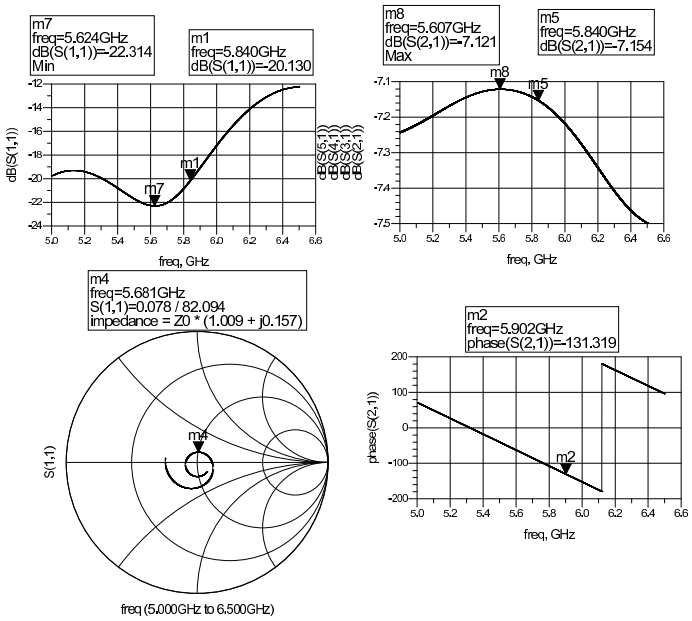

Figure F.6: Simulations results for the phase shifter integrated in the feed network. All phase shifters are in the delay mode.

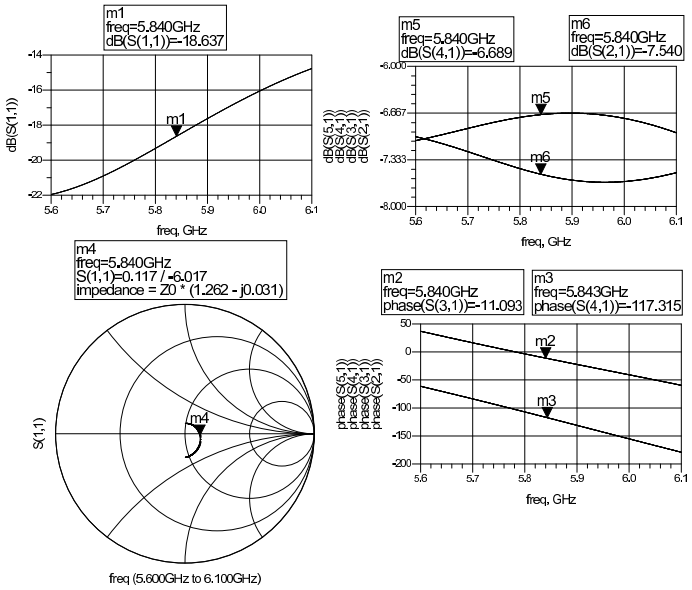

Figure F.7: Simulations results for the phase shifter integrated in the feed network. One main branch (S_{21} and S_{31}) with both phase shifters in the referance mode while the other main branch has both phase shifters in the delay mode.

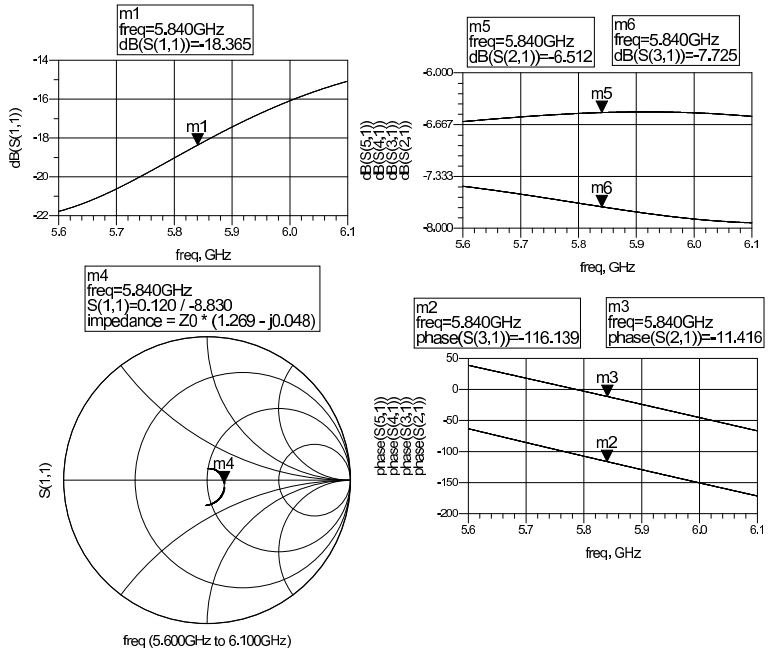

Figure F.8: Simulations results for the phase shifter integrated in the feed network. Both main branches have one phase shifter in each state (S_{31} and S_{41} is delay).

Appendix G

ADS Circuits, Results and Layouts from Chapter 8

G.1 Calibration Kit

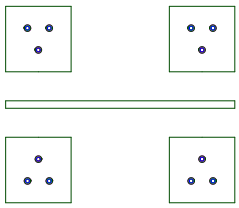

Figure G.1: Layout for the Thru component in the calibration kit.

Figure G.2: Layout for the open Reflection component in the calibration kit.

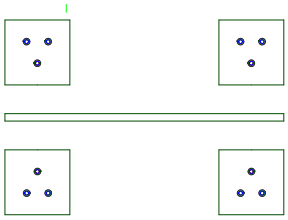

Figure G.3: Layout for the Line component in the calibration kit.

G.2 Tee-junction

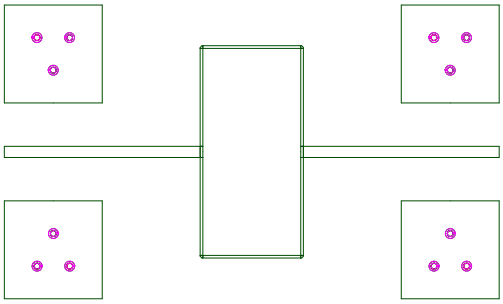

Figure G.4: Layout for the tee-junction test circuit.

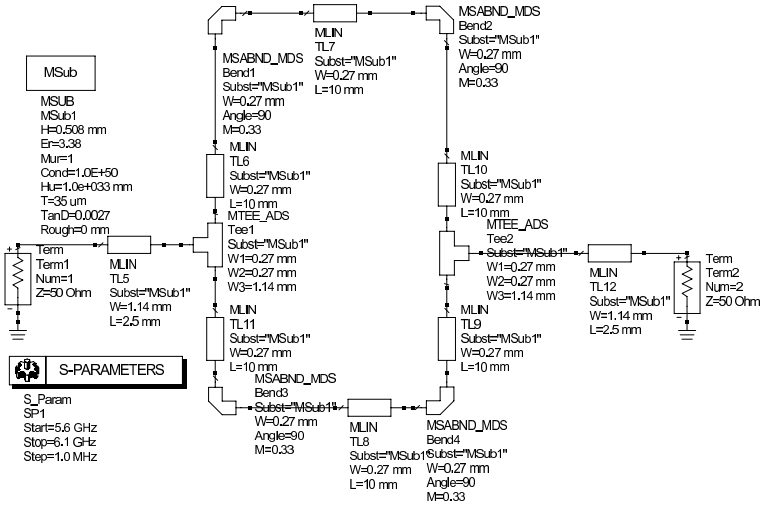

Figure G.5: Simulation circuit for the tee-junction.

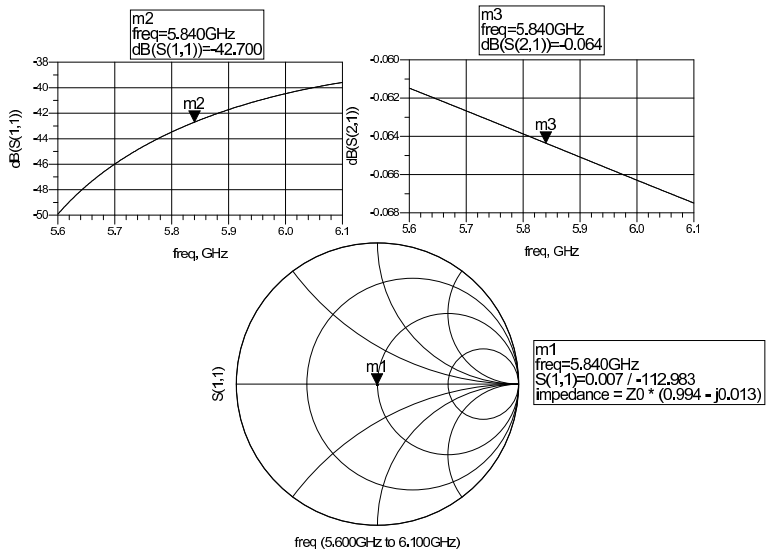

Figure G.6: Simulation results for tee-junction test circuit.

G.3 Quarter Wave Transformer

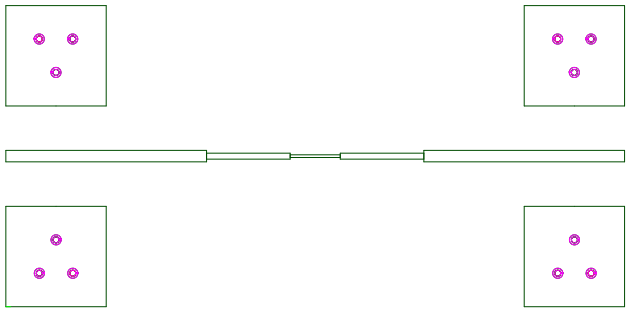

Figure G.7: Layout for the quarter wave transformer test circuit.

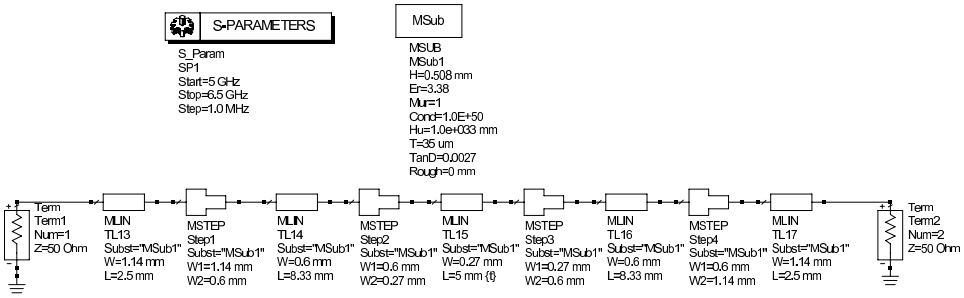

Figure G.8: Simulation circuit for the quarter wave transformer.

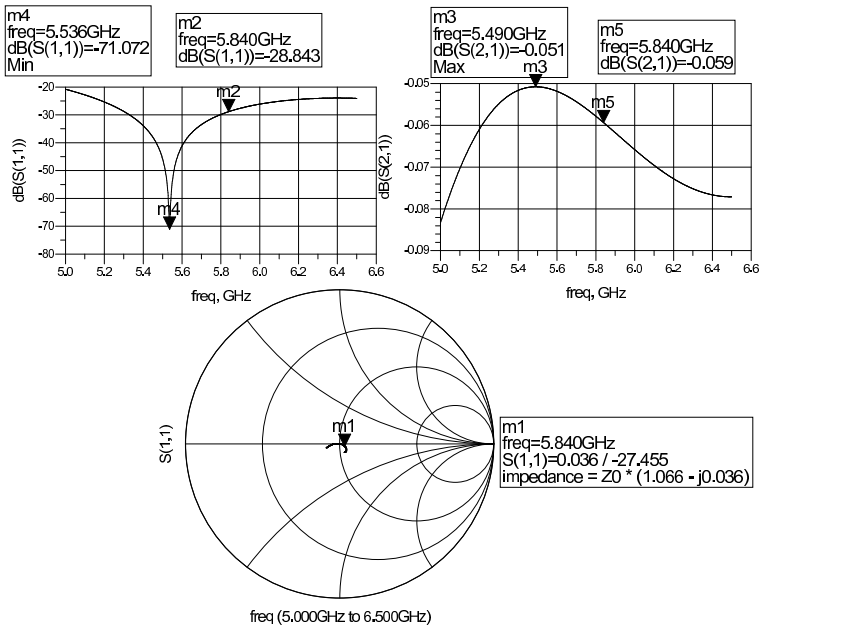

Figure G.9: Simulation results for the quarter wave transformer test circuit.

G.4 DC Network

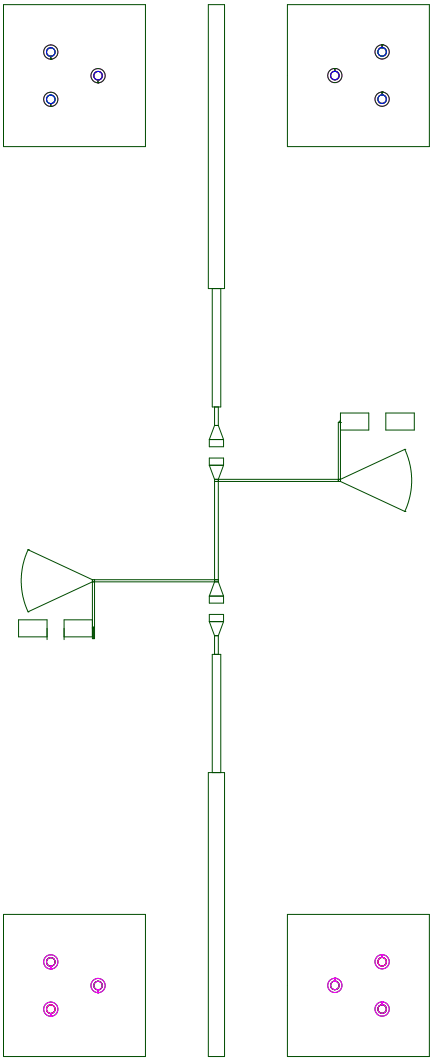

Figure G.10: Layout for the DC-network test circuit.

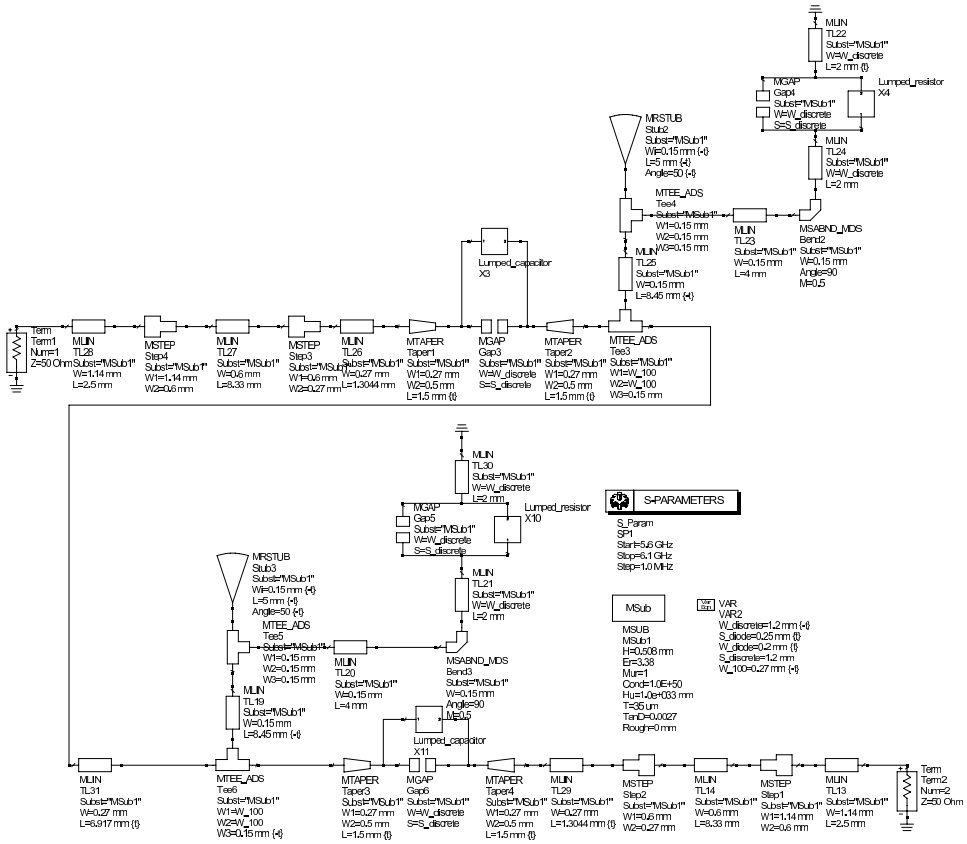

Figure G.11: Simulation circuit the DC-network test circuit.

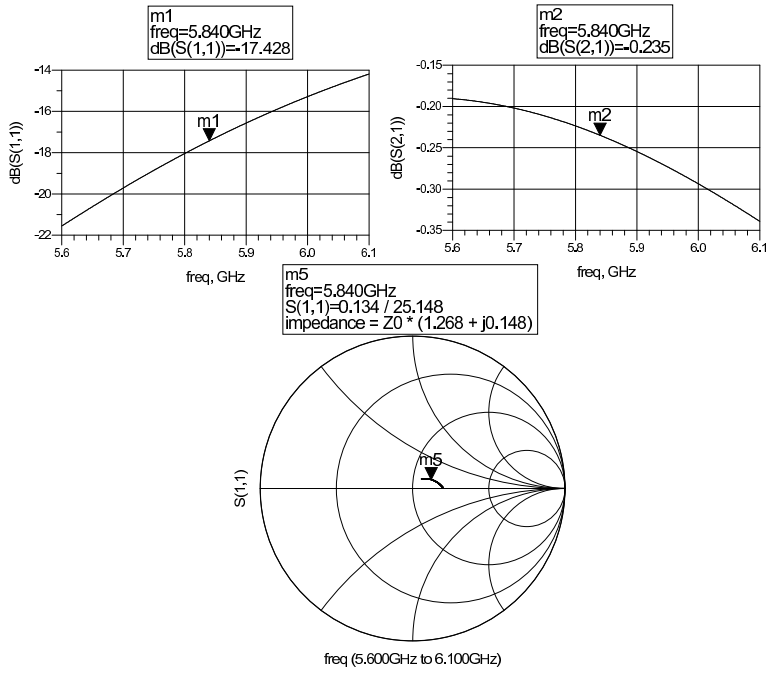

Figure G.12: Simulation results for the DC-network test circuit.

G.5 Phase Shifter

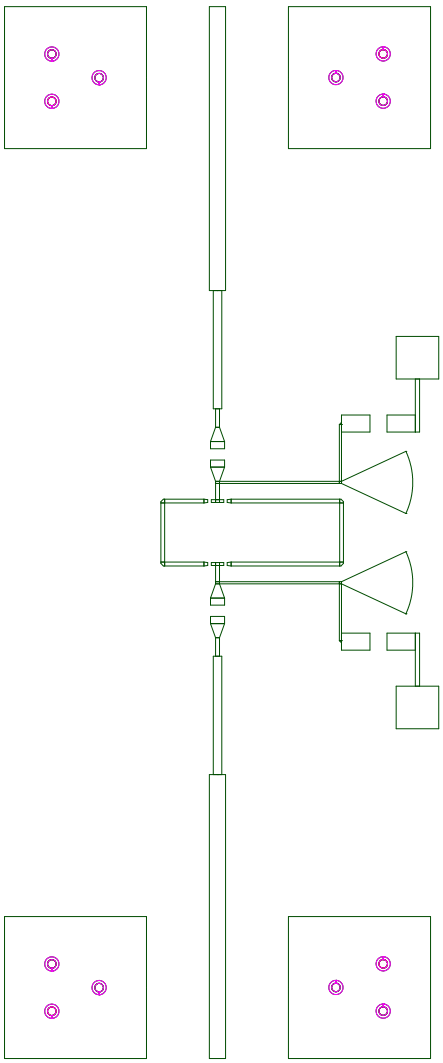

Figure G.13: Layout for the phase shifter network test circuit.

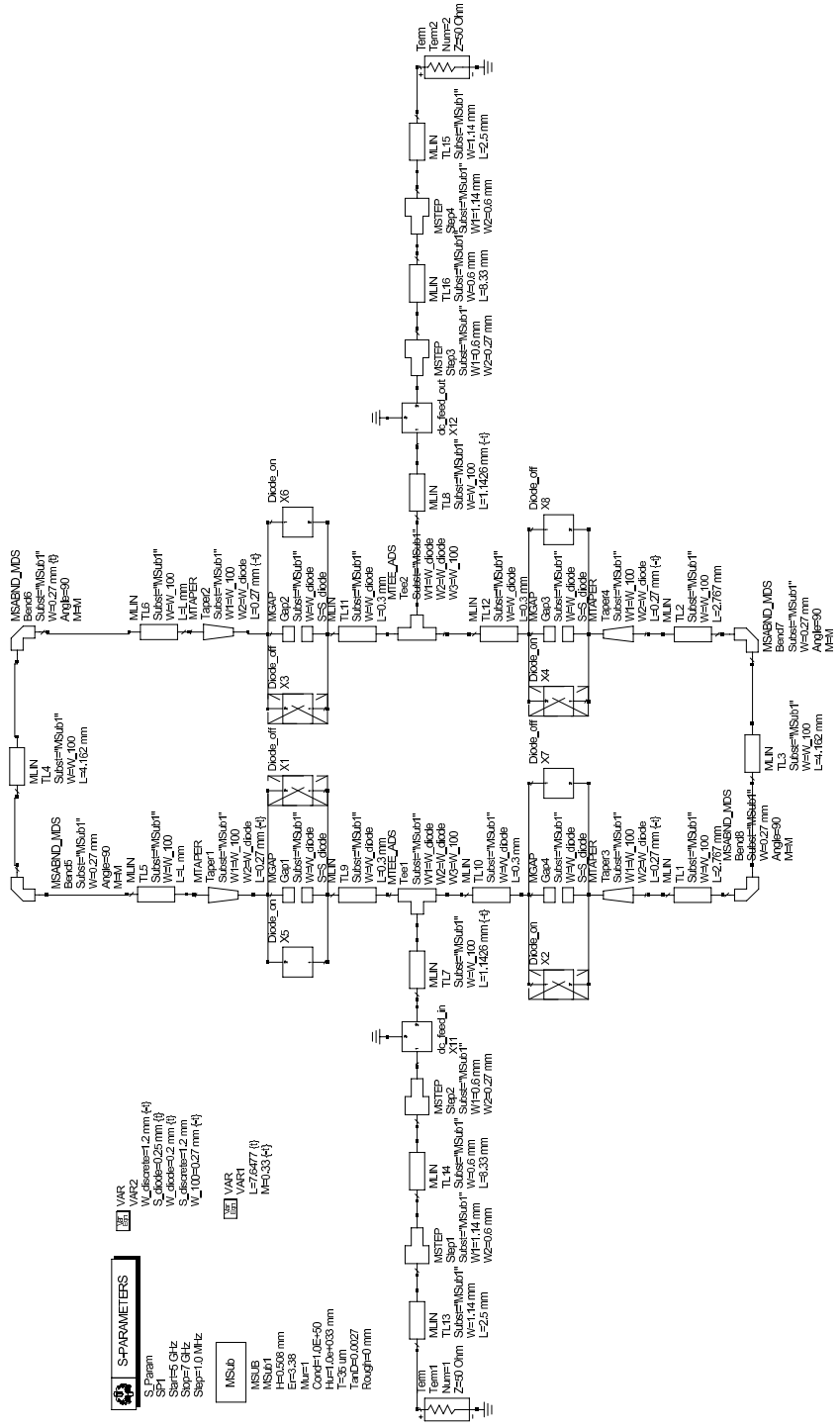

Figure G.14: Simulation circuit for the phase network test circuit.

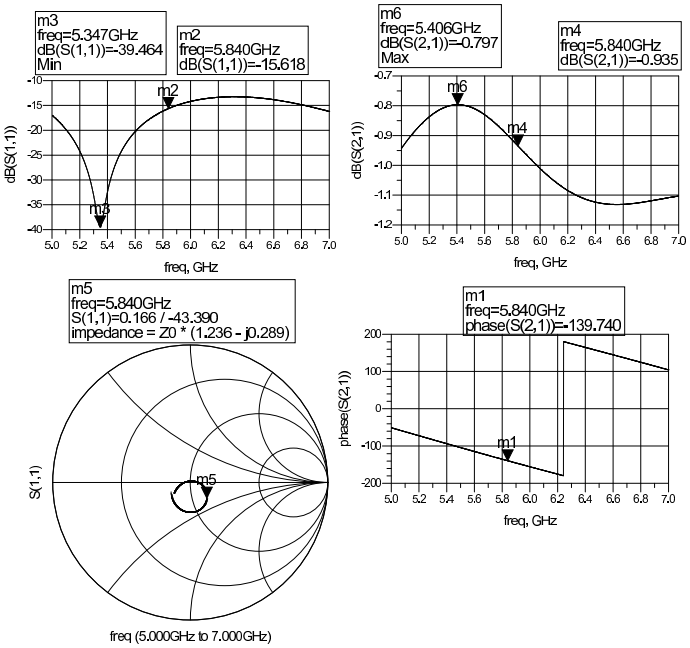

Figure G.15: Simulation result for the phase network test circuit. Reference mode.

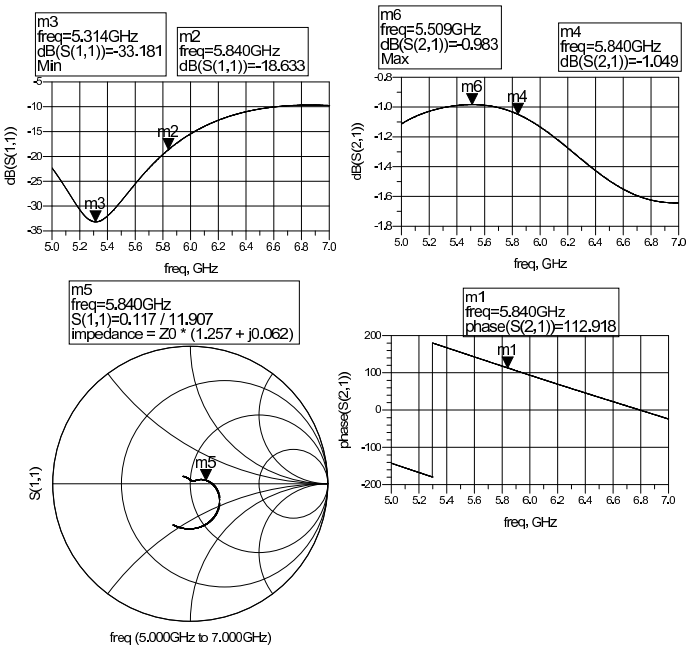

Figure G.16: Simulation result for the phase network test circuit. Delay mode.

G.6 Single Element

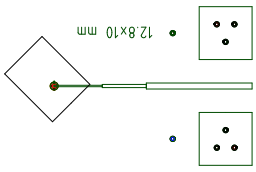

Figure G.17: Layout for a single MSA element.

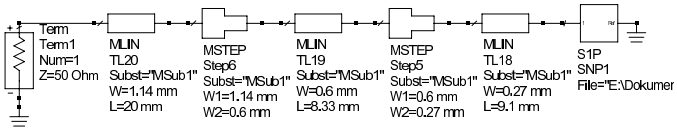

Figure G.18: Simulation circuit for a single MSA element.

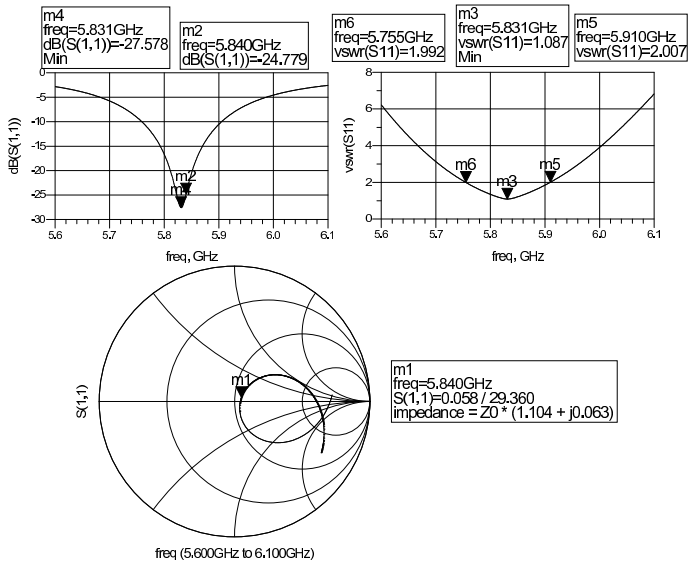

Figure G.19: Simulation results from a single MSA, 12.7×10 mm.

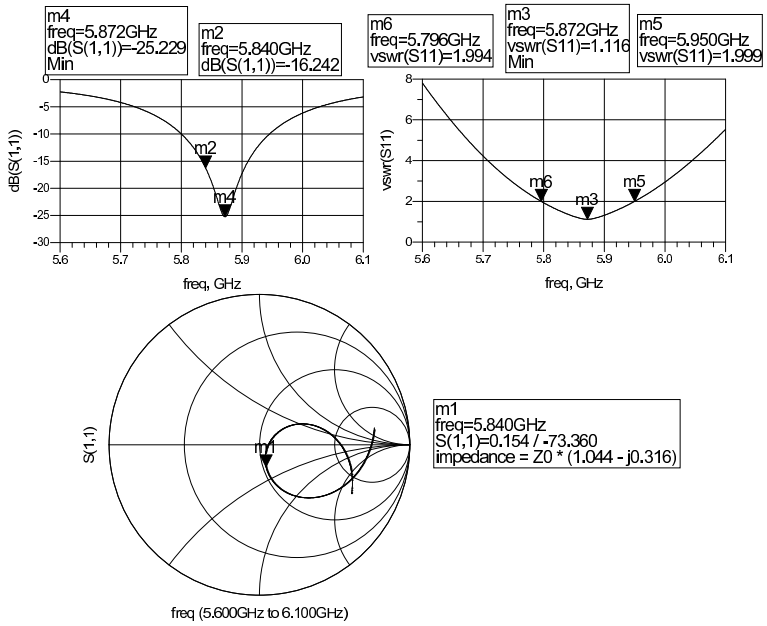

Figure G.20: simulation results from a single MSA, 12.6×10 mm.

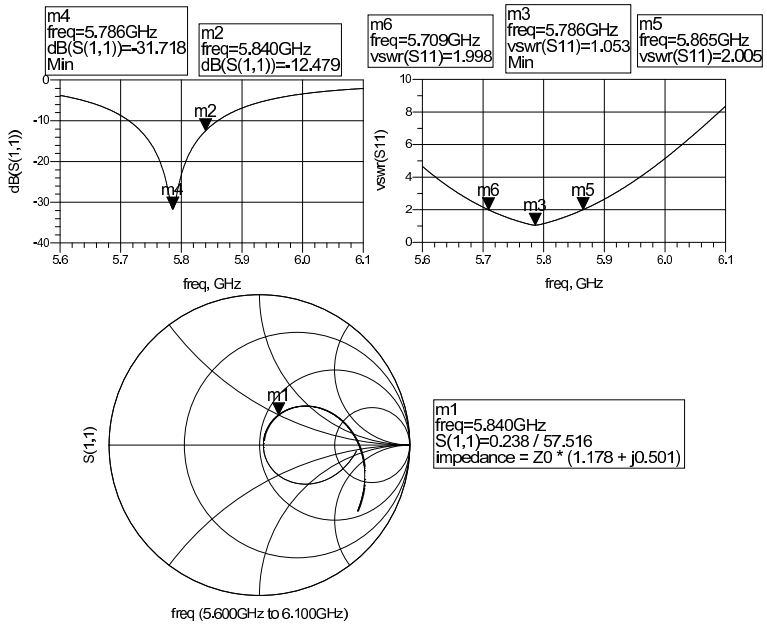

Figure G.21: Simulation results from a single MSA, 12.8×10 mm.

G.7 Static Array

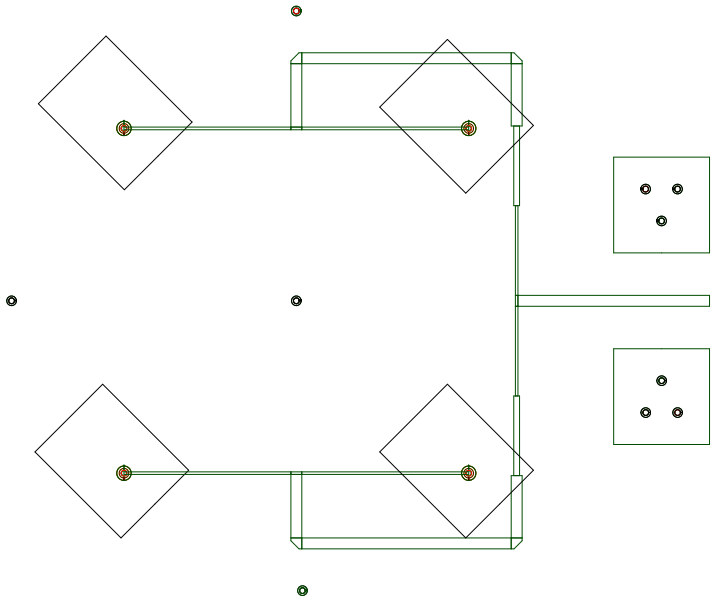

Figure G.22: Layout for array with no phase shifters.

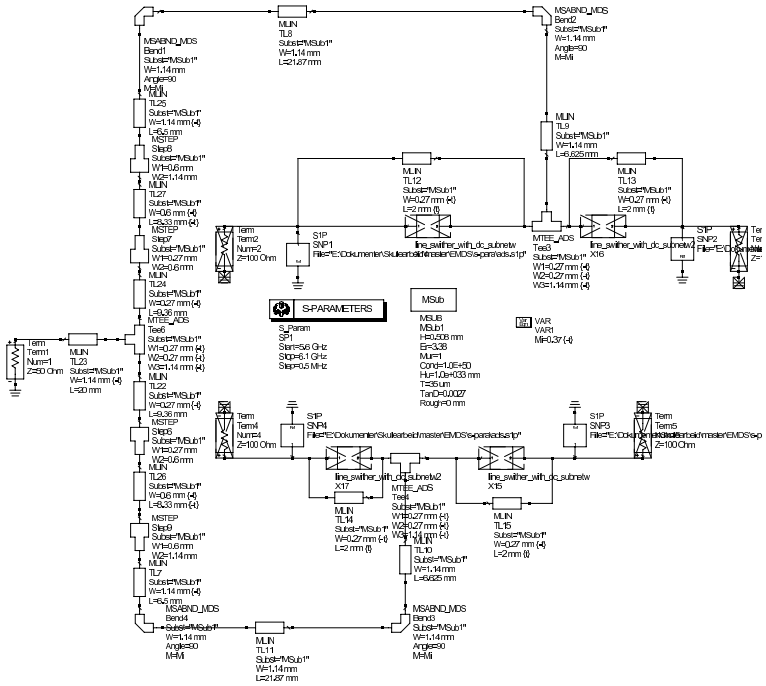

Figure G.23: Simulation circuit for array with no phase shifters.

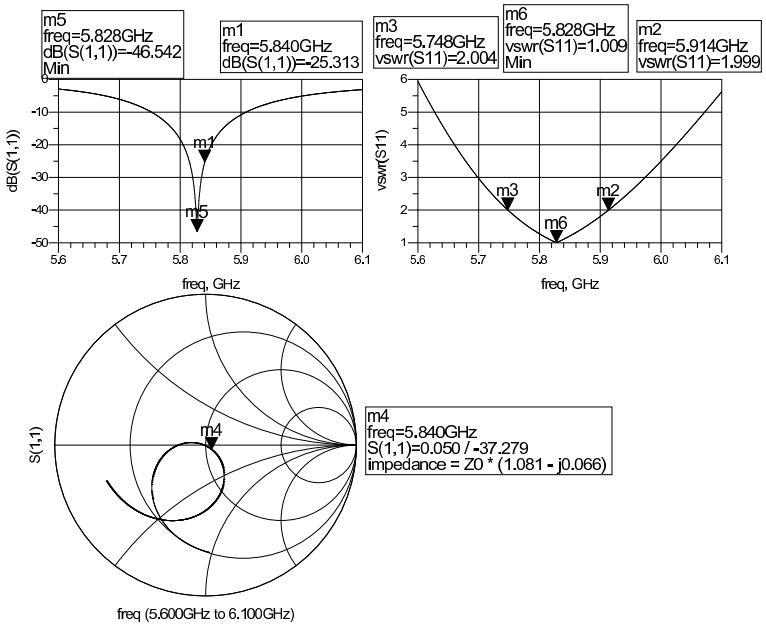

Figure G.24: Simulation circuit for array with no phase shifters.

G.8 Full Array

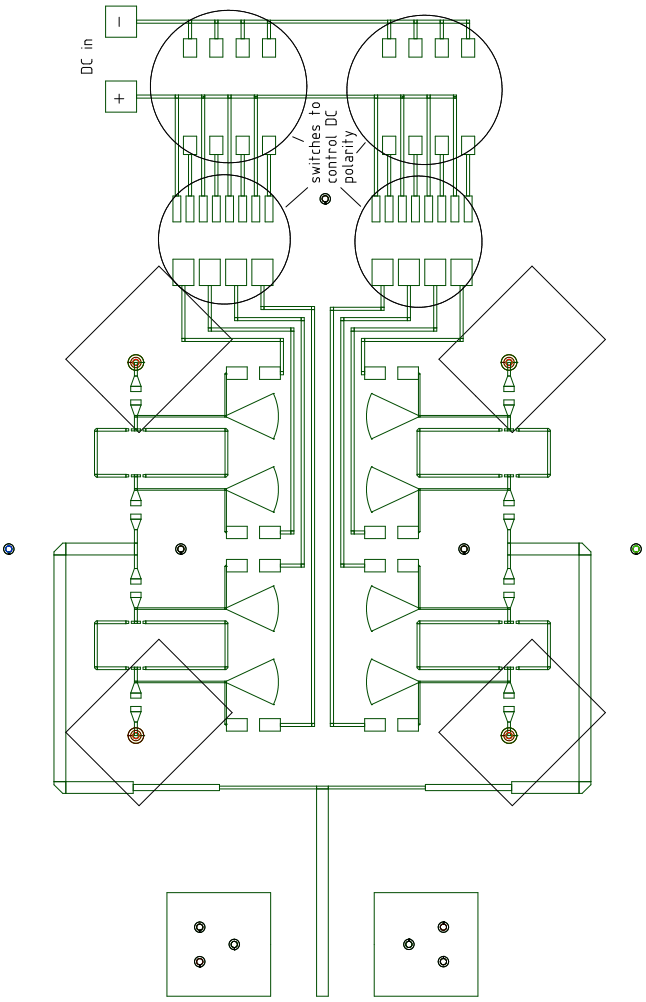

Figure G.25: Layout for the array with phase shifter and DC network with room for switches.

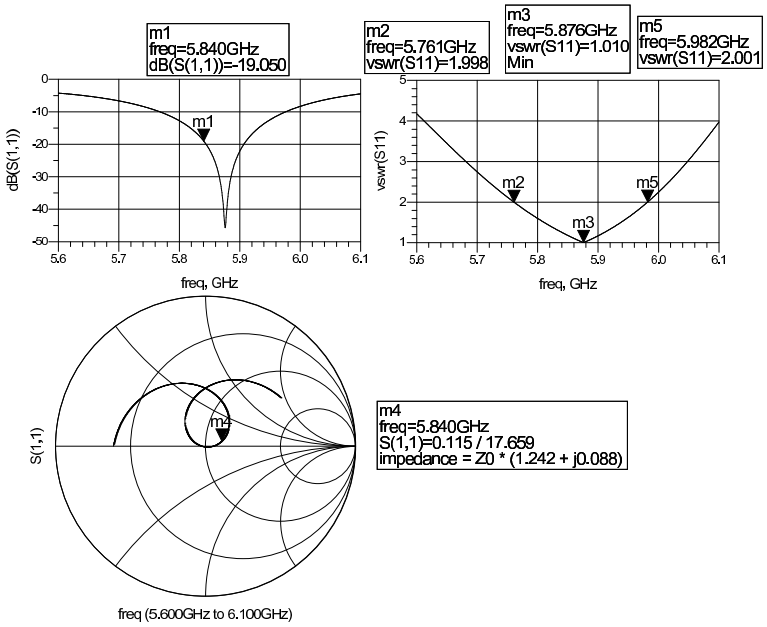

Figure G.26: Simulation results for the array with all phase shifters in reference mode, equivalent to using the boresight beam.

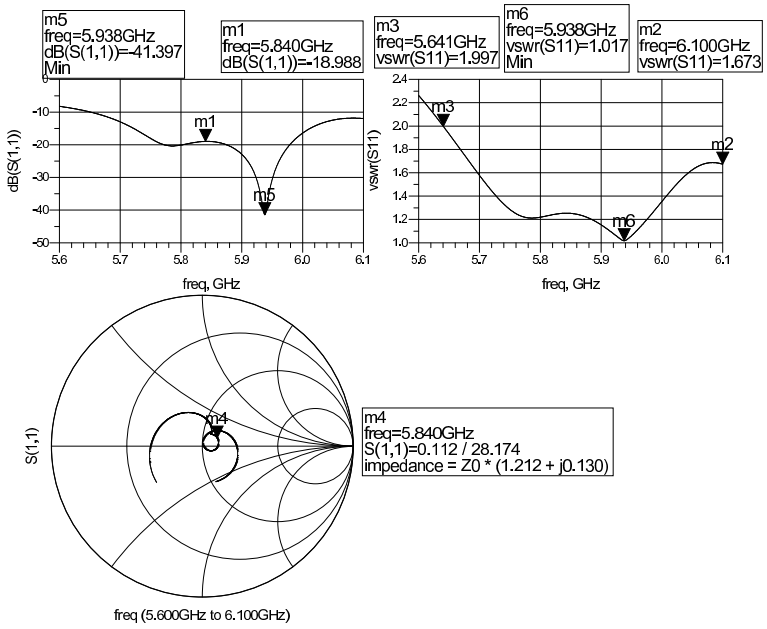

Figure G.27: Simulation results for the array with one main branch in the delay state and the other in the reference state, equivalent to steering the beam forwards or backwards.

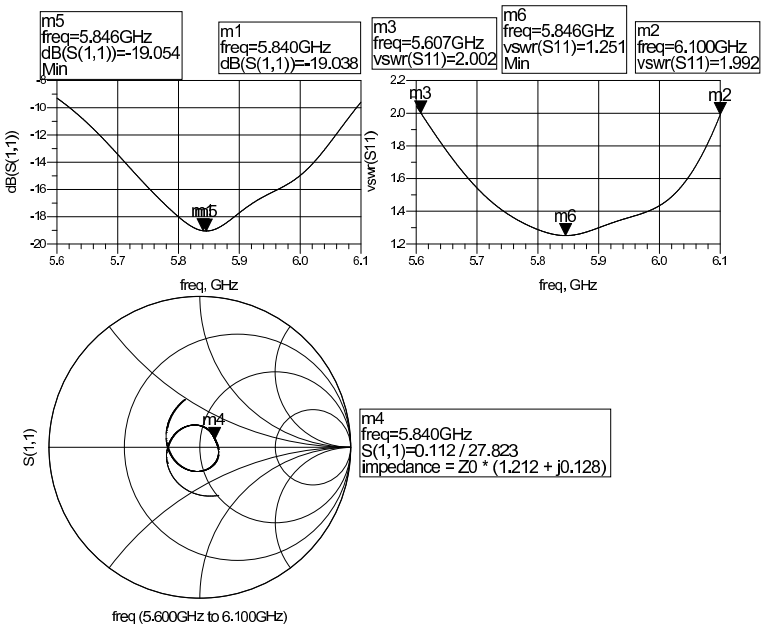

Figure G.28: Simulation results for the array where each main branch have both states represented, equivalent to steering the beam to left or right.

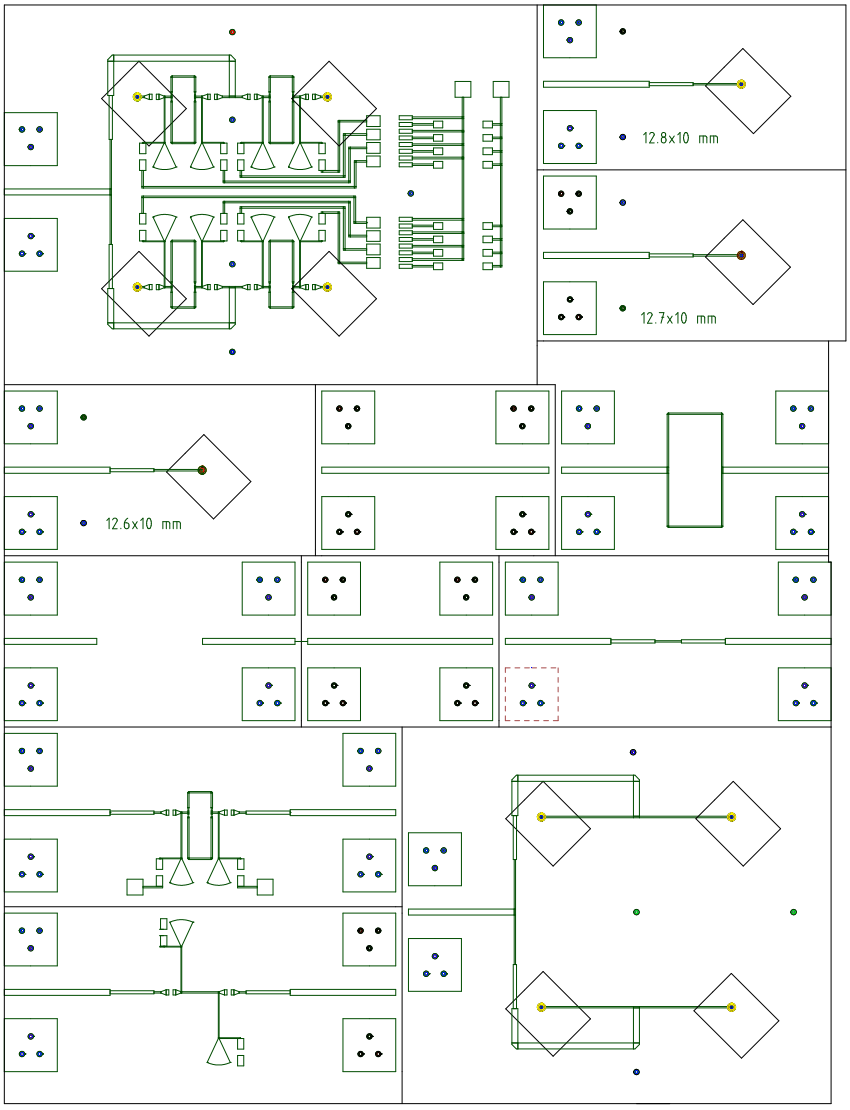

Figure G.29: All the circuits in one layout. This layout served as a basis for generating the Gerber files.